Electron and Phonon Dynamics in Topological Insulators at THz Frequencies

Im Fachbereich Physik
der Freien Universität Berlin
eingereichte Dissertation

Lukas Zacharias Braun

September 2016

This work was done between April 2012 and September 2016 in the Department of Physical Chemistry (Professor Martin Wolf) at the Fritz-Haber-Institute of the Max-Planck-Society.

Berlin, September 2016

Erstgutachter: Prof. Dr. Martin Wolf

Zweitgutachter: Prof. Dr. Martin Weinelt

Datum der Disputation: 14. Dezember 2016

Abstract

Three-dimensional topological insulators are fascinating materials with insulating bulk yet metallic surfaces that host highly mobile charge carriers with a spin orientation locked to the propagation direction. Such spin-velocity coupling facilitates the exciting possibility to launch spin-polarized charge currents by simply applying electric fields. Remarkably, illumination with light can also launch surface currents with tunable direction and magnitude, thereby potentially making topological insulators relevant for optoelectronic devices.

In this thesis, we use terahertz (1 THz = 1/ps) spectroscopy to investigate ultrafast charge-carrier dynamics in topological insulators. We develop a technique to reliably measure ultrafast photocurrents with unprecedented time resolution (20 fs) and apply this technique to detect currents on the surface and in the bulk of topological insulators.

To also gain insight into the current dynamics of charge carriers close to the Fermi energy, shortest available stimuli are desired with an excitation energy below the thermal energy to meet conditions as in electronic devices. Therefore, we use only recently available intense THz-electric fields (1 THz = 4 meV) to drive near-equilibrium electrons and phonon dynamics in topological insulators.

We monitor electron and phonon dynamics by a pump-probe scheme that detects the pump-induced changes in the dielectric function with subsequent time-delayed probe pulses. To separate the contributions of surface and bulk signals, we use thin-film samples and theoretical modeling of the optical probe process. With this technique, we observe a coherent phonon at a buried interface driven by a new mechanism that is resonant at the sum frequency (rather than the difference frequency) of all frequency pairs of the THz-pump spectrum. When the Fermi level position of our samples is tuned monotonously from n-type to p-type conductance, we observe a correlated change of the pump-induced THz-conductance. This dependence allows us to assign contributions of electron-phonon dynamics related to the bulk and to the surface. Remarkably, the strength of the electron-phonon coupling also depends on the Fermi level that culminates in an extremely long-lived excited state at the Dirac point in p-type topological insulators.

Our measurements strongly suggest that the often observed coupling of bulk and surface states is significantly reduced in our p-type samples even at room temperature, where transport measurements often find a bulk dominated conductance.

Kurzfassung

Topologische Isolatoren sind eine neuartige Klasse von Festkörpern, die sich durch hervorragende Oberflächenleitfähigkeit auszeichnet, obwohl das Innere des Festkörpers ein Isolator ist. Der Spin der Elektronen der metallischen Oberflächenzustände ist an ihre Bewegungsrichtung gekoppelt. Deshalb können spinpolarisierte Ströme durch das Anlegen eines äußeren elektrischen Feldes einfach erzeugt werden. Bestrahlt man einen topologischen Isolator mit Licht, so kann man Photoströme erzeugen, deren Größe und Richtung von der Polarisation des Lichts abhängen.

In der vorliegenden Arbeit wird Terahertz-Spektroskopie (1 THz = 1/ps) eingesetzt, um die ultraschnelle Dynamik in topologischen Isolatoren zu untersuchen. Dafür wurde ein Messverfahren entwickelt um ultraschnelle Photoströme mit zuvor nicht erreichter Zeitauflösung (20 fs) zu detektieren. Um darüber hinaus Einsichten in die Dynamik von Ladungsträgern nahe der Fermi-Energie zu gewinnen, sind die kürzest zur Verfügung stehenden Feldanregungen anzustreben, deren Anregungsenergie unterhalb der thermischen Energie der Elektronen liegt. Für diesen Zweck setzen wir intensive elektrische THz-Felder (1 THz = 4 meV) ein, um Elektronen und Gitterschwingungen (Phononen) nahe des Gleichgewichtzustandes anzuregen.

Wir verfolgen die Dynamik von Elektronen und Phononen mit Anrege-Abfrage Experimenten, die eine anregungsinduzierte Änderung der dielektrischen Funktion mit zeitverzögerten Abfragepulsen detektiert. Um Oberflächensignale vom Volumen zu unterscheiden, nutzen wir dünne Probenfilme und theoretische Modelle zur Beschreibung der optischen Abfrageprozesse. Somit werden wir empfindlich für verborgene Grenzflächen zwischen Probe und Substrat. An der Grenzfläche beobachten wir eine kohärente Gitterschwingung, die durch einen neuartigen Prozess angeregt wird, nämlich einer Resonanz, beschrieben durch die Summe (im Gegensatz zur Differenz) aller Frequenzpaare im Spektrum der Anregung. Wenn wir das Fermi-Niveau unserer Proben monoton von n- nach p-Dotierung ändern, beobachten wir eine korrelierte Änderung der THz-Leitfähigkeit, die wir einem Übergang von volumen- zu oberflächendominierten Signalen zuordnen. Sie geht mit einer starken Änderung der Elektronen-Phononen-Wechselwirkung einher, was sich insbesondere in einem außerordentlich langlebigen Anregungszustand am Dirac-Punkt äußert.

Unsere Ergebnisse weisen auf eine stark reduzierte Wechselwirkung zwischen Oberflächen- und Volumenzuständen in p-dotierten Proben hin, was sie von Transportmessungen unterscheidet, die häufig bei Raumtemperatur ein volumendominiertes Verhalten zeigen.

Contents

Contents IX

1 Topological insulator: An exciting state of matter 5
- 1.1 A new type of insulator . . . 5
  - 1.1.1 Quantum Hall insulator . . . 5
- 1.2 Three-dimensional topological insulators . . . 6
- 1.3 Generalized description of the topological state . . . 7
- 1.4 Properties and potential for THz electronics . . . 8

2 Ultrafast currents 11
- 2.1 Ohmic currents . . . 11
- 2.2 Photocurrents . . . 12
- 2.3 Photocurrent theory . . . 13
  - 2.3.1 Phenomenological description . . . 13
  - 2.3.2 Boltzmann-equation approach . . . 14
  - 2.3.3 Hydrodynamic model . . . 16
  - 2.3.4 Quantum-mechanical theory . . . 17

3 The Tool: Ultrafast THz electromagnetic pulses 19
- 3.1 Nonlinear light conversion . . . 19
  - 3.1.1 THz Generation . . . 20
  - 3.1.2 THz detection . . . 21

4 Experimental setup 23
- 4.1 The THz emission spectrometer . . . 23
- 4.2 The THz transmission spectrometer . . . 25
- 4.3 The THz pump-probe setup . . . 25
- 4.4 The laser and the THz sources . . . 26
  - 4.4.1 MHz-Laser Oscillator . . . 26
  - 4.4.2 kHz-Amplified Laser System . . . 27
  - 4.4.3 The THz sources . . . 28

5 Low noise data acquisition 31
- 5.1 DAQ “kHz setup” . . . 31
- 5.2 DAQ “MHz setup” . . . 31
  - 5.2.1 Rapid delay scanning . . . 32
  - 5.2.2 Step scan, lock-in detection . . . 33
  - 5.2.3 Time-domain multiplexing . . . 34

6 An ultrafast multimeter for measuring photocurrents and -voltages with 40 THz bandwidth 37
- 6.1 Motivation . . . 37

6.2 Basic principle . . . 38
6.3 Experimental details . . . 40
6.4 Determining the transfer function . . . 40
6.5 Transfer-function modeling . . . 43
6.6 Field extraction and robustness . . . 44
6.7 Discussion . . . 45
6.8 Conclusion . . . 46
Appendix of Chapter 6 . . . 47
6.A Reference-field calculation . . . 47
6.B Time-domain deconvolution . . . 48
6.C Modeling the transfer function . . . 49

7 Ultrafast photocurrents at the surface of the three-dimensional topological insulator Bi_2Se_3 51
7.1 Motivation . . . 51
7.2 Experimental details . . . 52
7.2.1 Ultrafast photocurrent amperemeter . . . 52
7.2.2 Ultrafast THz emission setup . . . 53
7.2.3 Sample properties . . . 54
7.3 Results . . . 55
7.3.1 Raw data . . . 55
7.3.2 Signal symmetries . . . 56
7.3.3 Ultrafast photocurrents . . . 57
7.3.4 Surface localization . . . 60
7.4 Discussion . . . 61
7.4.1 The source of the shift current . . . 61
7.4.2 The absence of circular photocurrents . . . 63
7.5 Conclusion/Outlook . . . 64
Appendix of Chapter 7 . . . 65
7.A Sample details . . . 65
7.B From electrooptic signals to THz fields . . . 65
7.C From THz fields to THz currents . . . 66
7.D Waveform mean amplitude . . . 67
7.E Azimuthal symmetry analysis . . . 67
7.F Extended symmetry analysis . . . 68
7.G Signal azimuthal symmetries . . . 70
7.H Spin relaxation in Bi_2Se_3 . . . 71
7.I Current magnitude of the pump-helicity-dependent photocurrent . . . 72

8 Ultrafast spin-to-charge-current conversion in $BiSbTe_3$/CoFeB 73
8.1 Motivation . . . 73
8.2 Experimental details . . . 74
8.2.1 Detection of ultrafast spin transfer . . . 74
8.2.2 Ferromagnet/topological-insulator bilayer . . . 74
8.3 Results . . . 75

8.4 Discussion . . . 75
8.5 Conclusion/Outlook . . . 76

9 Sum frequency excitation of coherent phonons in Bi_2Te_3 and Sb_2Te_3 77
9.1 Motivation . . . 77
9.2 Experimental details . . . 78
9.3 Raw data Bi_2Te_3 . . . 78
9.4 Signal separation . . . 80
9.5 Electronic component . . . 81
9.6 Resonant sum-frequency Raman excitation . . . 81
9.6.1 Sum-frequency or difference-frequency excitation? . . . 82
9.6.2 Is the phonon force impulsive? . . . 84
9.6.3 Fit results . . . 86
9.7 Spatial localization . . . 87
9.8 Comparison to Sb_2Te_3 . . . 89
9.8.1 Exclusion of other phonon driving mechanism . . . 89
9.8.2 Displacive excitation of coherent phonons in Sb_2Te_3 . . . 90
9.9 Discussion . . . 91
9.9.1 Electron dynamics . . . 91
9.9.2 Source of electron displacement . . . 92
9.9.3 Sum frequency DECP . . . 93
9.10 Conclusion/Outlook . . . 93
Appendix of Chapter 9 . . . 94
9.A TI dielectric function at THz frequencies . . . 95
9.B Modeling of pump and probe propagation . . . 95

10 Electron-phonon dynamics on the surface of $(Bi_xSb_{1-x})_2Te_3$ 99
10.1 Motivation . . . 99
10.2 Experimental details . . . 101
10.2.1 Sample characterization . . . 101
10.2.2 The THz-pump/THz-probe setup . . . 101
10.3 Results . . . 102
10.3.1 Pump-induced broadband THz transmission change at $t = 0$ . . . 102
10.3.2 Signal dynamics . . . 103
10.4 Discussion . . . 105
10.4.1 Pump-induced bleaching . . . 105
10.4.2 Pump-induced absorption . . . 106
10.4.3 Excited-state dynamics . . . 106
10.5 Conclusion/Outlook . . . 107

11 Summary 109

Bibliography 111

Publications 127

Acknowledgments **131**

Introduction

"Topological insulators: Star material"[Bru10a] and "Quantum magic can make strange but useful semiconductors that are insulators on the inside and conductors on the surface" [Moo11] are just two of recent headlines in leading scientific journals. They express the enthusiasm about a new material class called *topological insulators* [Moo10].

The name is somewhat confusing since the excitement is neither about its shape, nor is being insulating the material class's most interesting feature. A topological insulator is a solid that does not conduct an electric current through the bulk of the material, but does so along the surface. One may wonder why this effect is more exciting than the obvious alternative of coating an ordinary semiconductor with a thin layer of metal. It turns out that surface conductance of a topological insulator significantly differs from that of other two-dimensional electron gases, because it is a subtle result of spin-orbit interaction.

First, spin-orbit coupling is so strong that the spin axis of each surface electron is determined by the direction of the electron motion [Moo10]. In other words, the spin is uniquely locked perpendicular to the electron momentum. Therefore, applied electric fields induce spin-polarized surface currents [Li14] with such a sizable magnitude that they can be used to electrically manipulate adjacent magnetic materials [Mel14]. For example, a small current flowing through the topological insulator could efficiently read information stored in an adjacent magnetic layer, while a larger current could flip the magnetic orientation, thereby enabling writing.

Second, the surface electrons exhibit a linear Dirac-type dispersion [Hsi09a], resulting in an effective mass of zero and thus high mobility. Such zero-mass electrons have been known to also occur in graphene whose technological potential was shown by demonstrating very fast electronic devices such as field effect transistors with a cut-off frequency approaching the terahertz (THz) range [Lia10]. In contrast to graphene, counterpropagating electrons of topological insulators have opposite spin. Consequently, 180° back scattering is prohibited for most types of impurities [Moo10], thereby further increasing electron mobility. Remarkably, the linear Dirac-type surface state dispersion is robust against weak perturbations. Due to this so-called topological protection, topological insulators retain their unique bulk-insulating but surface-conducting character even in the presence of adsorbants under ambient air [Hoe14]. This paradoxical behavior arises from the bulk origin of the metallic surface.

These unique properties are ideal prerequisites to induce large spin polarizations by means of surface currents. Therefore, topological insulators are promising to act as first-place spin current sources in low-power spintronic applications. Up to now, however, most current measurements and spintronics works on topological insulators have been done at frequencies below 10 GHz [Mel14], significantly lagging behind the THz bandwidth of cutting-edge field-effect transistors [dA11]. To explore the ultimate speed limit of spin and charge currents in topological insulators, experiments have to reveal elementary processes of current generation and relaxation. Since many elementary scattering processes in solids occur on time scales of $\sim$ 10-1000 fs (1-100 THz) [Sun02], studying their dynamics requires

experiments with ultrashort time resolution.

This thesis

In this thesis, we induce and monitor electron transfer in topological insulators on ultrafast timescales by making use of the fastest available stimuli: femtosecond optical laser pulses and THz electromagnetic fields. While optical excitation mimics the situation in opto-electronic devices such as photodiods and solar cells, THz pulses lead to conditions rather similar to those found in electronic applications such as transistors. More over the optical photon energy ($\sim$ 1.5 eV) is much larger than both the thermal energy ($\sim$ 25 meV at room temperature) and the band gap ($\sim$ 0.3 eV) of typical topological insulators, whereas the opposite is true for THz photon energies ($\sim$ 4 meV). Therefore, we expect that optical and THz excitation trigger distinctly different dynamics in topological insulators.

In our experiments, we monitor the subsequent evolution of the photocurrent and the isotropic and anisotropic optical and THz conductivity by different and complementary optical probe schemes. By developing such advanced optical/THz pump-probe setups, we aim at answering important open questions of TI physics which are relevant from both a fundamental and applied viewpoint. Following optical excitation, how fast does the photocurrent build up and decay? Can we distinguish between surface and bulk currents? Recently, the observation of spin-polarized currents driven by circularly polarized light was reported [McI12b]. The microscopic model used to explain this current suggests very large THz current densities, an expectation that needs to be confirmed. The static measurements also revealed a current component driven by linearly polarized light, which could not be assigned to a microscopic generation mechanism [McI12b]. To understand the nature of this current, we measure its ultrafast dynamics.

When near-equilibrium carriers are generated by ultrashort THz electric fields, we explore the relevant interactions that bring the excited state back to equilibrium. So far, time-resolved investigations have mainly addressed the relaxation of highly non-equilibrium carriers [Wan12] and revealed a filling of the surface states by bulk carriers, following dynamics dominated by electron-phonon interactions in the bulk states [Sob14], while a different kind of bottleneck was observed for surface electrons at the Dirac point[SB16]. How do the dynamics evolve when the excited electron excess energy is reduced to a minimum? To reveal the role of electron-phonon interaction, which is expected to determine such dynamics, we investigate different regimes of the near-equilibrium electron-phonon interaction at the surface and in the bulk of n-doped Bi_2Te_3 and p-doped Sb_2Te_3.

Finally, on a more applied note, we address the potential of spin-to-charge current conversion in topological insulators. Since topological insulators such as Bi_2Se_3 are known to exhibit very large spin-orbit coupling strength, they have been shown to efficiently convert charge currents into perpendicularly flowing spin currents [Mel14]. Can we induce and measure the opposite effect on ultrafast time scales? Can we inject an ultrafast spin photocurrent from a ferromagnetic metal into an adjacent TI and observe conversion into a charge current? Similar processes in metals were shown to lead to efficient emission of THz radiation with a magnitude and bandwidth that outperforms standard THz emitters. Does ultrafast spin-to-charge current conversion in TIs pave the way to even better THz

emitters?

To answer these questions, required tools were developed to exploit THz emission spectroscopy for ultrafast current detection and gain interface sensitivity in THz-pump/optical-probe experiments.

This thesis is structured as follows. Chapters 1 and 2 provide a brief introduction to the topological insulating state of matter and ultrafast currents driven by optical and THz fields. This is followed by a description of how THz pulses are exploited as a spectroscopic tool in general (Chapters 3 and 4), the technological developments required to achieve low noise signal acquisition (Chapter 5) and the method to measure ultrafast currents with unprecedented time resolution (Chapter 6). To obtain a microscopic understanding of the charge carrier dynamics driven with optical (Chapters 7 and 8) and THz fields (Chapters 9 and 10), models and analysis techniques were developed. They are detailed in several appendices directly following the result chapter they belong to rather than at the end of this work. These appendices are useful for readers who wish to follow the development of the results in a profound manner.

1 Topological insulator: An exciting state of matter

This thesis focuses on the ultrafast dynamics of currents in topological insulators (TIs). As outlined in the introduction, surface electrons in TIs have unique properties including high mobility and spin-velocity locking. Since the occurrence of such surface states is far from obvious, this chapter briefly summarizes some theoretical background of this extraordinary material class.

1.1 A new type of insulator

The band theory of electric conduction was one of the early successes of quantum mechanics in the 1920s [Blo29], giving a simple explanation why crystalline solids are electric conductors or insulators. In the independent-electron model, electronic states of solids are characterized by Bloch states, that is, plane waves with wavevector $\mathbf{k}$ modulated by a lattice-periodic function. Since $\mathbf{k}$ is continuous, electronic states form continuous bands.

The response of the solid to an applied electric field is determined mainly by the electrons close to the Fermi energy. In equilibrium, states with $\pm\mathbf{k}$ are equally populated such that no current flows. In metals, due to only partially filled bands, an external electric field can redistribute the population such that the occupation at, say, $+\mathbf{k}$ is larger than $-\mathbf{k}$, and a current is launched [Kit69]. In contrast, an insulator has completely filled bands that are separated from empty bands by an energy gap, as depicted in Fig. 1.1a.

It is this gap that prohibits the redistribution of population by an external field and, thus, prohibits conductance in an ordinary band insulator. However, the discovery of the quantum Hall effect in the 1980s by Klitzing *et al.* [Kli80] has shown that there are also other, completely different kinds of insulators.

1.1.1 Quantum Hall insulator

In 1980, Klitzing *et al.* [Kli80] showed that a two-dimensional metal placed in a strong magnetic field is an insulator in its bulk but conducts along the edges. The bulk is insulating since the magnetic field forces the electrons on confined circular orbits [Has10]. The quantization of these orbits leads to highly degenerate Landau levels m with energy $E_m = \hbar\omega_c(m + 1/2)$, separated by an energy $\hbar\omega_c$, where ω_c is the cyclotron frequency. When N levels are completely filled, while the $(N + 1)$-th level is completely empty, the energy levels are gapped just as in an insulator.

However, the same magnetic field that induces the gap in the bulk, forces electrons onto robust skipping orbits at the edges (Fig. 1.1b). Thus, a two-dimensional metal in a strong magnetic field has an energy gap in the bulk, but conducts along the surface edge states [Has10].

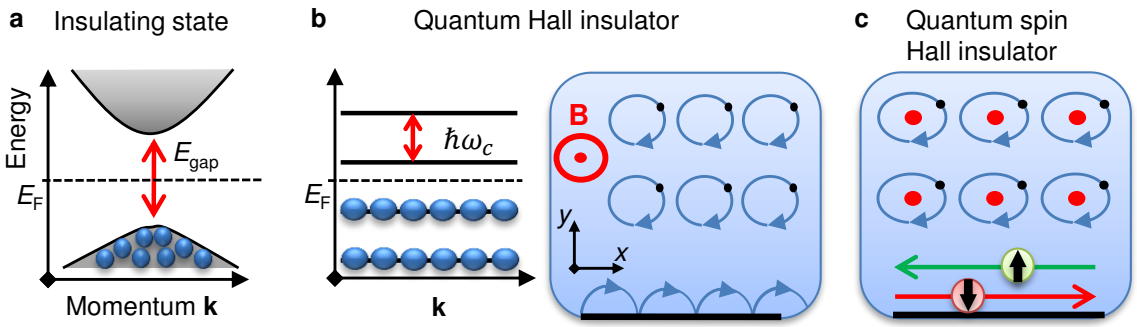

Figure 1.1: Insulating states of matter. **a**, Band structure of a normal band insulator. An energy gap E_{gap} separates completely filled bands from empty bands. **b**, The quantum Hall state. A strong magnetic field forces bulk electrons in a two-dimensional metal on closed cyclotron orbits but induces metallic skipping orbits at the edges. Cyclotron orbits are associated with Landau energy levels separated by $\hbar\omega_c$. Thus, electronic states are separated by an energy gap as in an normal insulator when levels below the Fermi energy E_F are completely filled. **c**, The effective magnetic field of spin-orbit coupling induces two kinds of edge states in the quantum spin Hall insulator (two-dimensional topological insulator), one for "spin up" and one for "spin down".

1.2 Three-dimensional topological insulators

Soon after the discovery of the quantum Hall state, theory [Ber06] showed that an external magnetic field is not necessary for an insulator to have a robust conducting edge state. Without external magnetic field, two kinds of edge states can appear that transport electrons of spin up and spin down in opposite directions [Has10] as illustrated in Fig. 1.1c. In so-called topological insulators, the role of the magnetic field is assumed by spin-orbit coupling, an intrinsic property of all solids. Later, it was discovered that topological order also occurs in three-dimensional materials [Fu07].

An important prerequisite for the occurrence of the topological phase is band inversion [Zha09, Fu07], that is, the energetic order of the conduction band and valence band is inverted. Such inversion is illustrated in Fig. 1.2a that shows the exemplary band order of a normal insulator with the symmetric band (parity $+1$) lower in energy than the antisymmetric band (-1) separated by a band gap. If, for example, strong spin-orbit coupling lowers the energy of the antisymmetric state below that of the symmetric state, an inversion of valence and conduction band occurs. This twist in the band order leads to the topological state, and although still being an insulator, the resulting state is topologically different from an ordinary insulator [Zha09].

Physically, an arbitrary number of band crossings can induce surface states, but topological protected is only an odd number of states [Zha09]. This is due to time reversal symmetry that forces the surface states to come in Kramers pairs of spin-up and spin-down states [Fu07]. The symmetry of these states is depicted in Fig. 1.2b. In the trivial topology, an even number $2n$ ($n \in \mathbb{N}$) of surface states can be gapped out in pairs. Thus, start and end point are in the same bulk band (Fig. 1.2b). However, for an odd number, the $(2n+1)$-th spin-up and spin-down band have to cross the band gap to retain the symmetry (Fig. 1.2b). It is in this sense that a single pair of edge states is protected by time reversal

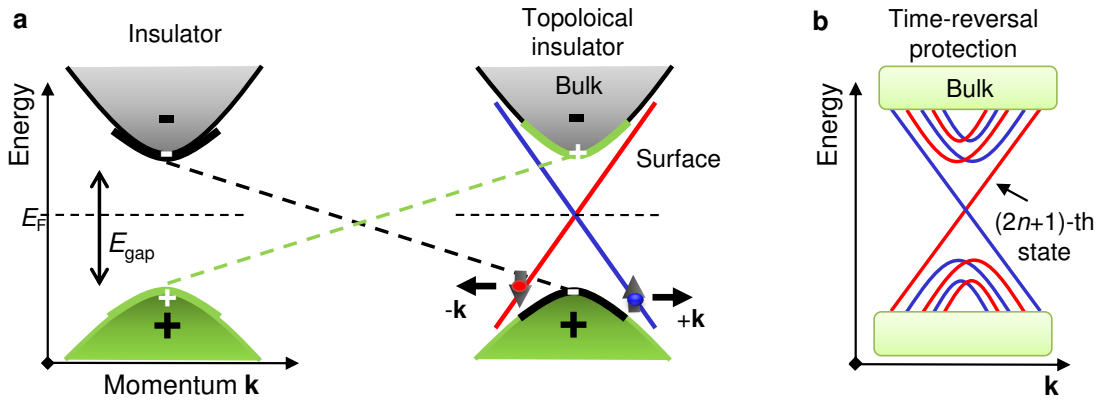

Figure 1.2: Band inversion drives a topological phase transition. **a**, Exemplary band order in a normal insulator with the symmetric band (parity +1) lower in energy than the antisymmetric band (−1) separated by a band gap. Band inversion of the highest valence band (+1) with the lowest conduction band (−1) causes metallic surface states. **b**, Time-reversal symmetry requires that from an odd number of surface states, all but one single pair of surface states can open a gap. Thus, start and end point are in the same bulk band. The remaining single $(2n+1)$-th Kramer's pair is topologically protected by time-reversal symmetry.

symmetry [Zha09].

1.3 Generalized description of the topological state

A band inversion in the bulk states is required for the transition to the topological insulating state. However, an even number of band inversions causes the trivial state. In fact, theory could show that counting an even or odd number of band inversions occurring in all filled bulk bands can identify the TI state in inversion-symmetric media [Zha09]. To motivate the origin of the topological insulating state in a more general consideration, several theoretical concepts are required, which are beyond the scope of this work. In the following we, therefore, give a brief suggestion how bulk properties can enforce a metallic surface state.

For this purpose, we consider electrons in a one dimensional chain. In the periodic region of the chain, the electronic eigenstates are Bloch states, which can be labeled by a crystal momentum k and written in the form

$$\Psi_k(x) = \mathrm{e}^{\mathrm{i}k\cdot x} u_k(x), \tag{1.1}$$

where the function u_k has the periodicity of the lattice, and x is the real space coordinate. Topological aspects arise from the smooth dependence of the wavefunction u_k on k, which causes a nontrivial phase obtained during a cyclic adiabatic evolution of the parameter k [Has11]. Such a loop can be defined even in one dimension due to the periodicity of the Brillouin zone $k \in [-\pi/a, \pi/a]$:

$$\gamma = \int \langle u_k |\, i\partial_k \,| u_k \rangle \, \mathrm{d}k. \tag{1.2}$$

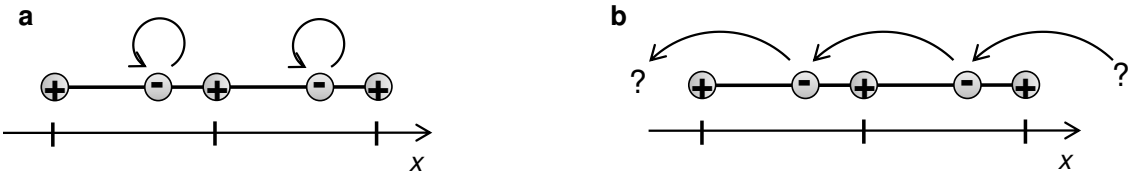

Figure 1.3: Possible evolution of charge center positions (−), relative to a one-dimensional lattice of ions (+), as the system evolves adiabatically around a closed loop in the parameter k. The charge centers must return to themselves, but can do so either **a** without or **b** with a shift by a lattice constant. While in the bulk (infinitesimal long chain) in both scenarios their is no difference between before and after the cyclic evolution, scenario **b** induces a charge unbalance at the chain ends.

The integral is a scalar. An intuitive clue of its meaning is given by replacing ∂_k by x as would be appropriate for the action on a plane wave. This suggests the γ is closely related to the spatial location of the electrons [Has11]. However, for a plane wave, γ is zero. To obtain a non-zero γ one may think of a wave packet, whose center of mass is interpreted as the charge position.

The way how such a wave packet and, thus, its center of mass evolves under cyclic adiabatic evolution can be very different in various solids [Has11]. This fact can be used to motivate the difference in topology of insulators [Fu06].

In an adiabatic loop of the parameter k, initial and final points are the same. Therefore, the charge centers must return to their initial locations at the end of the cyclic evolution. Importantly, they can do so in two ways, as illustrated in Fig. 1.3a and b. If each charge center returns to itself, then no charge is transferred. However, as illustrated in Fig. 1.3b, this need not be the case; it is only necessary that each charge center returns to one of its periodic images. Consequently the charge center may change by a multiple of the lattice constant. This integer ambiguity in one-dimensions is closely related to the quantum Hall effect in two-dimensions [Has11].

In topological insulators, time-reversed pairs of charges counter propagate and, consequently, no charge but spin might be transferred in an adiabatic loop in $\mathbf{k}$. In analogy to the charge position ambiguity that may lead to a charge pump along the chain, Fu and Kane Ref. [Fu06] discussed a spin pump to the surface as the signature of a non-trivial topological insulator.

1.4 Properties and potential for THz electronics

A unique feature of TI surface states is their robustness against weak perturbations, which protects their extraordinary properties even in the presence of adsorbants under ambient air [Hoe14]. The crossing of the band gap on the surface not only ensures that these states are gap-free but also implies a linear Dirac-type dispersion [Hsi09a] with high band velocity. The resulting high mobility is important, for instance, in field-effect transistors to enable low voltage operation with large currents.

Another important aspect of the TI surface states is spin-velocity locking, a property

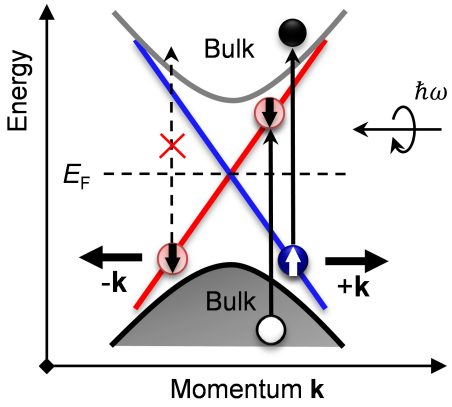

Figure 1.4: Photocurrent control on the surface of a topological insulator. In equilibrium, spin-polarized electrons propagate in opposite direction. Circularly polarized light preferentially couples to only one spin species. Since opposed spins correspond to reversed momenta, illumination with circularly polarized light causes an unbalanced population at $+\mathbf{k}$ and $-\mathbf{k}$, and thus, launches a current.

of high interest to extend the functionalities of conventional electronics by the spin of the electron [Sta14]. For this purpose, TIs are highly promising to induce large spin polarizations by simply driving surface currents [Mel14].

Part of this considerable potential was demonstrated by recent works which reported the exciting possibility of launching TI surface currents by simply illuminating the sample with light. The direction of the photocurrent could be controlled through the polarization of the incident light beam [McI12b]. Such photocurrent control can be easily understood as follows: in the widely used three-dimensional TI Bi_2Se_3, the surface states, in an idealized model, can be described by a single Dirac cone [Liu10] with a spin structure locked to the momentum. Thus, electrons with the same energy but opposite momentum have opposite spin. Circularly polarized light preferentially couples to electrons with spins that are either aligned or anti-aligned to the wavevector $\mathbf{q}$ for light with left- or right-handed circular polarization. When shining circularly polarized light obliquely onto the surface of a TI (Fig. 1.4), electrons with a spin component parallel to $\mathbf{q}$ are preferably excited over electrons with a spin component anti-parallel to $\mathbf{q}$, which leads to an carrier distribution that is asymmetric with respect to $\mathbf{k}$ and, thus, a net photocurrent. Changing the helicity of the light then reverses the direction of the current.

These and other experiments proved that the TI surface states are extremely mobile [Kas15, Koi15], spin polarized [Wan11, Mel14] and topologically protected against gap opening [Zha09]. Remarkably, currents in the surface states can be optically controlled [McI12b, Olb14, Kas15].

These properties show the potential relevance of TIs for spintronic and opto-electronic applications. To explore the ultimate speed limit of currents in TIs, novel experiments have to reveal elementary scattering processes that occur on timescales of $\sim 10 - 1000$ fs [Sun02].

To stimulate and monitor electron transport on ultrafast timescales, we make use of the fastest available optical and electrical stimuli. (i) Femtosecond (1 fs=10^{-15} s) laser pulses

will be used to launch ultrafast current bursts. Such optical injection of currents and spin polarization in spin-orbit-materials is highly promising to boost clock rates towards optical frequencies in opto-spintronic devices. (ii) Only recently available powerful THz electric fields with peak fields of ~ 1 MV/cm [Hir11, Sel08] will be used to drive charge carriers close to the Fermi energy. The response of sub-thermal ($\hbar\omega < k_{\mathrm{B}}T$) excited carriers to high field strength meets the situation of charge transport in electronic devices.

In the following chapter we will discuss the processes that lead to current generation and control with laser pulses with frequencies ranging from THz to the optical realm.

2 Ultrafast currents

To drive and study transport of charges and spin angular momentum on ultrafast time scales (< 1 ps), extremely fast stimuli are required: femtosecond optical pulses and sub-picosecond (terahertz) electric field transients. This chapter will provide the theoretical background how these two very different stimuli can drive charge transport.

2.1 Ohmic currents

When an external electric field is applied to a solid, a charge current flows. Electric fields can be provided by, for instance, batteries, electronic oscillators operating at frequencies up to 100 GHz or optical fields. According to Ohm's law, the charge current density $\mathbf{j}$ increases linearly with the field $\mathbf{E}$ [Jac06],

$$\mathbf{j}(\omega) = \sigma(\omega)\mathbf{E}(\omega), \tag{2.1}$$

where σ is the conductivity at angular frequency ω.

Electrical conduction of metals or doped semiconductors is often described within a simple model proposed by Paul Drude in 1900 [Dru00]. In the Drude model, the conductivity is characterized by two parameters, that is, the charge carrier density n and the rate $1/\tau$ of electron collisions with obstacles which are not further specified. The Drude DC conductivity reads as [Ash76]

$$\sigma_0 = \frac{ne^2\tau}{m^*}. \tag{2.2}$$

Here, e is the elementary charge, and m^* is the effective carrier mass. The AC complex conductivity is related to σ_0 by [Ash76]

$$\sigma(\omega) = \frac{\sigma_0}{1 - \mathrm{i}\omega\tau}. \tag{2.3}$$

To understand how a THz electromagnetic field drives the electrons within the Drude theory, it is instructive to decompose the complex conductivity into real and imaginary parts

$$\mathrm{Re}\ \sigma = \frac{\sigma_0}{1+\omega^2\tau^2} \tag{2.4}$$

$$\mathrm{Im}\ \sigma = \frac{\sigma_0\omega\tau}{1+\omega^2\tau^2} \tag{2.5}$$

The real part represents the current response, in-phase with the driving field, which produces resistive Joule heating, while the imaginary part represents the $\pi/2$ out-of-phase inductive current [Jac06]. In the low frequency region ($\omega\tau \ll 1$) the resistive character of Re σ dominates. Since τ can be as short as $\sim$ 10 fs [Sun02], the response of conduction electrons in metals and semiconductors to THz radiation is often well described by a peak at zero frequency (Eq. (2.4)). The width of this Drude peak is equal to the inverse relaxation time of the electrons. In the high frequency region ($\omega\tau \gg 1$), however, the Drude theory predicts essentially an inductive carrier response (Eq. (2.5)) with the optical

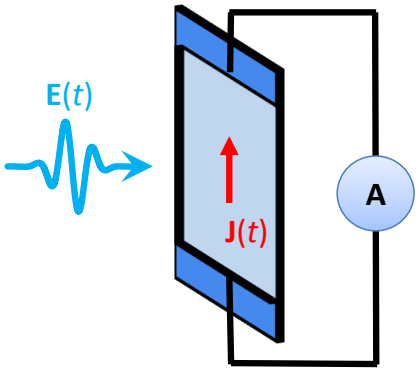

Figure 2.1: Photocurrent generation. A field $\mathbf{E}(t)$ incident on matter launches a charge current $\mathbf{J}(t)$. An optical rectified current can be detected with an amperemeter connected to the contacts at the edges of the sample.

conductivity decreasing with $1/\omega$.

In a more rigorous theory, the Drude conductivity can be understood to arise from intraband transitions between electronic Bloch states. Interband transitions, however, cannot be written in a Drude-like form.

2.2 Photocurrents

Ohm's law is a typical example of linear response, that is, the reaction $\mathbf{j}$ scales linearly with the perturbing $\mathbf{E}$ (Eq. (2.1)). Beyond linear response, the next step are currents that scale with the field squared, $\mathbf{j} \propto \mathbf{E}^2$. Such currents can be launched by irradiating matter with light and are known as photogalvanic or photovoltaic currents [Bel80]. In certain cases, one can even control the current direction with the light polarization [Gan03b, Gla14].

Photocurrents play an important role in many biological systems and electronic devices. For example, Bacteriorhodopsin, a bacterium protein, captures light energy to pump charges across a membrane and subsequently stores the absorbed light as chemical energy [Mus01]. Such light-to-chemical energy conversion is the first step of human vision process [Mus01]. The required conversion steps are light harvesting, charge separation, recombination and carrier collection. These processes are also essential to build an efficient solar cell [Hen06] to trigger photochemical reactions [Mus01] or to launch ultrafast charge and spin currents for large-bandwidth spintronic devices [McI12b, Kam13a, Sei16].

There are many more light-driven current sources. They range from heat-induced currents in pyroelectrics [vB81] over thermoelectric currents due to a heat gradient between two dissimilar conductors [Nol13] to light absorption processes in non-inversion symmetric solids [Gla14], which cause an asymmetric velocity distribution due to the optical transition between states that are different with respect to their charge center of mass or velocity [Nas06]. The last process is of special interest as it allows one to control the direction of photocurrents through the polarization of the incident light beam [McI12b, Gla14]. When an inversion-symmetric medium is photo-excited, electric-dipole-type currents cancel in the bulk material. However, at its surface, inversion symmetry is always broken. Therefore,

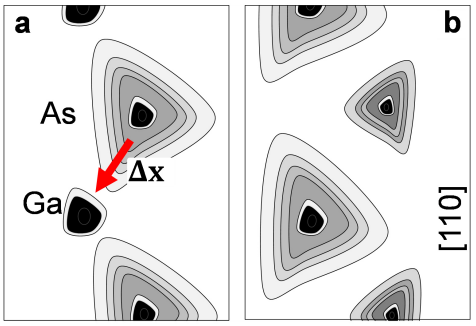

Figure 2.2: Shift current source. Electron density in the (110) plane of GaAs for **a**, the highest valence electron, and **b**, lowest Γ point conduction band. Dark regions correspond to higher densities. **a** and **b** can be considered to show an approximate "before-and-after" look on the electron density in GaAs upon optical transition from valence to conduction band. In the ground state the highest valence band electrons are localized around the arsenic atom **a**. An excitation with photon energies above the band gap can populate states nearer to the gallium atom **b**. Such transition effectively shifts charges on the order of a bondlength (arrow) on femtosecond time scales. Figure according to Ref. [Nas06].

photocurrents in inversion-symmetric media are often surface-sensitive probes[Olb14].

Note that excitation with short laser pulses on the time scale of elementary scattering processes in matter launches ultra-short current bursts with a time structure that strongly depends on the light-absorption process [Nas06], the subsequent charge transport [Joh02] and relaxation [Kra79] of the photo-excited carriers. Measurement of ultrafast current dynamics, therefore, provides insight into the mechanisms that govern current generation and relaxation [Lam05, Joh02, Bea02].

To understand photocurrents and their signatures, we need a theoretical background that describes the generation process and subsequent dynamics of charge transport. In the following, we briefly summarize theoretical aspects of three classes of photocurrents: *optical rectification*, *shift currents* and *injection currents*.

2.3 Photocurrent theory

2.3.1 Phenomenological description

Classically, an ensemble of particles with charge q_j and velocity $\mathbf{v}_j$ carry a microscopic current

$$\mathbf{J}(\mathbf{x},t) = \sum_j q_j \mathbf{v}_j \delta(\mathbf{x} - \mathbf{x}_j) \tag{2.6}$$

When a current $\mathbf{j}$ scales with $\mathbf{E}^2$, it can be phenomenologically described by the most

general quadratic relationship between $\mathbf{j}$ and $\mathbf{E}$ that can be written down as [Boy03]

$$j_i(\mathbf{x},t) = \sum_{jk} \int\int\int\int \mathrm{d}t_1 \mathrm{d}t_2 \mathrm{d}^3\mathbf{x}_1 \mathrm{d}^3\mathbf{x}_2 \, \sigma^{(2)}_{ijk}(t-t_1, t-t_2, \mathbf{x}-\mathbf{x}_1, \mathbf{x}-\mathbf{x}_2) E_j(\mathbf{x}_1,t_1) E_k(\mathbf{x}_2,t_2). \tag{2.7}$$

The response function $\sigma^{(2)}_{ijk}$ contains all relevant information of the current generation process, e.g., the symmetry of the sample, and the specific current generation mechanism given by the material and its electronic structure. An important simplification is to assume that the response is spatially local, i.e., a field at position $\mathbf{x}$ generates a current only at the very same position. A spatially local quadratic response leads to a current [Boy03]

$$j_i(\mathbf{x},t) = \sum_{\mathrm{jk}} \int\int \mathrm{d}t_1 \mathrm{d}t_2 \sigma^{(2)}_{ijk}(\mathbf{x}, t-t_1, t-t_2) E_j(\mathbf{x},t_1) E_k(\mathbf{x},t_2). \tag{2.8}$$

This simplification presumes that correlation lengths are much shorter than the length scales of the driving electric field $\mathbf{E}$. A very relevant correlation length is given by the mean free path of electrons. For example, in the topological insulator Bi_2Se_3, it is ~ 2 nm (bulk, [Hru11]), which is much smaller than the wavelength (790 nm) of light with a photon energy of 1.57 eV and its attenuation length in the bulk of Bi_2Se_3 (24 nm, [McI12a]). The nonzeroelements of $\sigma^{(2)}_{ijk}$ are constrained by the local symmetries of the medium. Most notably, $\sigma^{(2)}_{ijk} = 0$ in inversion-symmetric media.

Even though Eq. (2.8) is local in space, it is still nonlocal in time: the response to a field $\mathbf{E}(\mathbf{x},t_1)$ is "stored" for some time Δt and can interact with $\mathbf{E}(\mathbf{x},t_2)$ if $(t_2 - t_1) < \Delta t$. Δt may vary between almost zero in transparent materials and typical current relaxation times in opaque materials (femto- to picoseconds, [Jac06]). Therefore, the memory of the excitation strongly determines the temporal structure of ultrafast photocurrents [Lam05, Joh02, Bea02].

2.3.2 Boltzmann-equation approach

While the previous subsection provided a phenomenological description of photocurrents, we now discuss a microscopic model of photocurrent generation. In a single-particle picture, the quantum mechanical electronic eigenstates of a solid can be described as Bloch states $|b\mathbf{k}\rangle$ where b is the band index and $\mathbf{k}$ is the wavevector. In thermal equilibrium, that is, before optical excitation of the solid, the electronic system is characterized by the occupation number $f_{b\mathbf{k}}$ of Bloch states. According to Fermi-Dirac statistics, $f_{b\mathbf{k}}$ is given by the Fermi function.

When an optical pump pulse is incident, it couples pairs of initial states $|i\rangle$ and final states $|j\rangle$ and, thus, induces a coherent superposition of states. Shortly after the pump pulse is gone (typically after 1 - 10 fs [Sun02]), the coherence disappears and, thus, the electronic system is fully described by populations of the Bloch states [Ash76].

To calculate the population transfer from $|i\rangle$ to $|j\rangle$, one can make use of perturbation

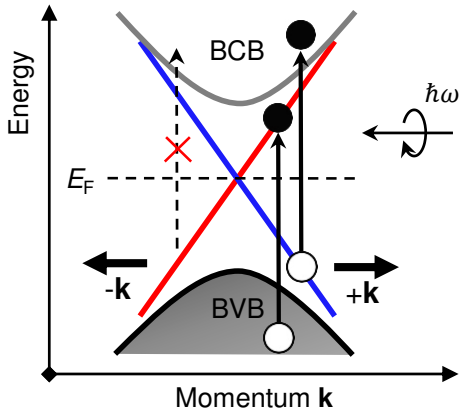

Figure 2.3: Current injection by an asymmetric momentum space population. Circular polarized light drives transitions between spin-polarized and unpolarized states in a topological insulator [McI12b]. Transition selection rules dictate that the optical excitation occurs at $+\mathbf{k}$ but not at $-\mathbf{k}$ and therefore a photocurrent is launched with a magnitude determined by the velocity difference $(\mathbf{v}_\mathrm{h} - \mathbf{v}_\mathrm{e})$ between initial and final state and the number of asymmetrically excited charge carriers.

theory and model the excitation dynamics by a rate equation [Mad72]

$$\frac{\partial f_j}{\partial t} = \sum_i \left[w_{ij} \cdot f_i(1 - f_j) - w_{ji} \cdot f_j(1 - f_i) \right]. \tag{2.9}$$

Here, w_{ij} is the transition rate that is proportional to the square of the perturbation field $\mathbf{E}$ (Fermi's golden rule).

Resonant excitation of an excited-state population launches *injection currents* [Rio12], provided the transition from $|i\rangle$ to $|j\rangle$ is accompanied by a change $\mathbf{v}_\mathrm{h} - \mathbf{v}_\mathrm{e}$ of the electrons' band velocity (Fig. 2.3). *Shift currents* [Nas06], arise when the transition drives a charge transfer by $\Delta\mathbf{x}$ (Fig. 2.2).

Spatial inhomogeneities such as interfaces or surfaces require to add a local parameter $\mathbf{x}$ to the distribution function $f(\mathbf{x}, b\mathbf{k}, t)$. Such $\mathbf{x}$-dependence can be justified by a semiclassical approach. When a potential $\phi(\mathbf{x})$ is superimposed on the periodic potential of the crystal, the electrons with band index b can be considered to form wave packets and, thus, can be treated as classical particles [Ash76, Mad72]. This approach is valid provided that the potential $\phi(\mathbf{x})$ varies sufficiently slowly on length scales much larger than the spatial extent of the wave packet. For example, in Bi_2Se_3 a relevant surface potential is induced by band bending in the order of 100 meV over 12 nm [McI12a], which is ~ 10 meV over a lattice constant, significant smaller than the band gap (300 meV).

Applying the wavepacket picture, the "local" bandstructure and, thus, "local" occupation numbers $f(\mathbf{x}, b\mathbf{k}, t)$, allow us to write down the photocurrent as

$$\mathbf{j}(\mathbf{x}, t) = \sum_{b\mathbf{k}} \mathbf{v}_{b\mathbf{k}} f(\mathbf{x}, b\mathbf{k}, t) + \frac{\partial}{\partial t} \sum_{b\mathbf{k}} \mathbf{x}_{b\mathbf{k}} f(\mathbf{x}, b\mathbf{k}, t) \tag{2.10}$$

The two terms quantify the injection and shift current, respectively [Lam05].

The current dynamics for shift and injection currents involve not only the generation process but also the subsequent evolution of the charge distributions in the sample. The kinetics of this distribution function $f(\mathbf{x}, \mathbf{v}, t)$ can be described with the Boltzmann equations for each carrier sort c (e.g. electrons and holes), electrons (c=e) and holes (c=h)

$$\left(\frac{\partial}{\partial t} + \mathbf{v}_\mathrm{c}\nabla_\mathbf{x} + \frac{q_\mathrm{c}}{m^*}\mathbf{E}_\mathrm{c}\nabla_\mathbf{k}\right) f_\mathrm{c}(\mathbf{x}, b\mathbf{k}, t) = g_\mathrm{c}(\mathbf{x}, b\mathbf{k}, t) + \left.\frac{\partial f}{\partial t}\right|_\mathrm{c}^\mathrm{coll}. \tag{2.11}$$

Here, q_c is the carrier charge and m^* the effective mass. The generation term g_c is proportional to the laser power density, and the collision term includes all scattering process with obstacles that bring the system back to equilibrium. Due to the one-dimensional geometry of our samples and laterally homogeneous excitation, we will consider in the following only gradients along z. Accordingly, the equation for the total electric field can be written down as [Hel91]

$$\frac{\partial}{\partial z}E_z = \frac{e}{\varepsilon}(n_\mathrm{h} - n_e + N^+ - N^-). \tag{2.12}$$

In this equation, n_c is the carrier density, N^+ and N^- the densities of ionized impurities and ε the dielectric function.

2.3.3 Hydrodynamic model

The Boltzmann equation (Eq. (2.11)) contains the full kinetics of carriers described by the distribution function $f(\mathbf{x}, b\mathbf{k}, t)$. However, $f(\mathbf{x}, b\mathbf{k}, t)$ can be parameterized by just a few quantities, that are, the mean values of velocity v_c, center of mass of the charges x_c and the temperature T_c. With this simplification the dynamics of the decaying current $\mathbf{j} = ne\mathbf{v}$ can be expressed by the drift velocity evolution along z of the distribution function, that is [Hel91],

$$\frac{\partial}{\partial t}v_\mathrm{c} + \frac{k_\mathrm{B}T}{n_\mathrm{c}m^*}\frac{\partial}{\partial z}n_\mathrm{c} + \frac{k_\mathrm{B}}{m^*}\frac{\partial}{\partial z}T + v_\mathrm{c}\frac{\partial}{\partial z}v_\mathrm{c} - \frac{q_\mathrm{c}E_z}{m^*} = \frac{\alpha P(t)}{\hbar\omega}\mathrm{e}^{-\alpha z} + \left.\frac{\partial v}{\partial t}\right|_\mathrm{c}^\mathrm{coll}. \tag{2.13}$$

The terms on the left hand side describe diffusion along carrier density and temperature gradients, velocity relaxation, and charge acceleration in space charge fields (Eq. (2.12)). The source terms on the right account for carrier generation and collisions where $P(t)$ is the laser power density, α^{-1} the absorption length, and $\hbar\omega$ the photon energy.

Eq. (2.13) also accounts for the important example of drift currents in space charge fields, for which the velocity evolution can be given within the Drude model [Sha04]

$$\mathbf{v}(t) = \frac{q_\mathrm{c}\tau}{m^*}\mathbf{E}(\mathrm{e}^{-t/\tau} - 1). \tag{2.14}$$

Here, τ is the Drude scattering time. Such drift currents in external bias fields are used in standard photoconductive THz emitters [Sha04].

2.3.4 Quantum-mechanical theory

In a more rigorous quantum mechanical ansatz that also accounts for coherences during the excitation, it is possible to derive similar expressions as in the last section. Assumed that only the electrons of some system interact with a classical electromagnetic field given by the vector potential $A(x,t)$, then, to first order in the light field and in Coulomb gauge, this interaction is described by the Hamiltonian [Czy04]

$$H_{\text{e-light}} = \int \mathrm{d}^3\mathbf{x}\, \mathbf{j}(\mathbf{x})\mathbf{A}(\mathbf{x},t). \tag{2.15}$$

The current operator $\mathbf{j}$ has interband contributions, that describe transitions from valence to conduction band and intraband contributions that account for dynamics within these bands. Sipe *et al.* [Sip00, Nas06] used second-order perturbation theory in the independent particle approximation and negligible scattering to find three current contributions that can be assigned to optical rectification, shift and injection currents:

$$\mathbf{j}(t) = \mathbf{j}_{\text{or}} + \mathbf{j}_{\text{sh}} + \mathbf{j}_{\text{inj}}. \tag{2.16}$$

The quantum-mechanical treatment justifies the ansatz of Eq. (2.10), but also provides additional insight into shift and injection currents. Therefore, we briefly discuss the results of Ref. [Sip00].

The *shift current* response for light polarized linearly along $j \in \{x,y,z\}$ and band occupation $f_{nm} = f_n - f_m$ is given as

$$\sigma^{\text{sh}}_{ijk}(0;\omega,-\omega) = \frac{\pi e^3}{\hbar^2}\int \frac{\mathrm{d}^3\mathbf{k}}{8\pi^3}\sum_{m,n} f_{nm} R^i_{nm} |M^j_{nm}|^2 \delta(\omega_{nm}-\omega). \tag{2.17}$$

The sum runs over all pairs of states (m,n). Here,

$$R^i_{nm}(\mathbf{k}) = \left(X^i_{nn}(\mathbf{k}) - X^i_{mm}(\mathbf{k})\right) + \frac{\partial \phi_{nm}(\mathbf{k})}{\partial k^i} \tag{2.18}$$

is the shift vector component along i that has two contributions: first, a shift of the center of charge distribution $X^i_{nn} = \int_{\text{cell}} \mathrm{i} u_{\mathbf{k},n}(r)\nabla_{\mathbf{k}} u_{\mathbf{k},n}(\mathbf{x})\mathrm{d}^3\mathbf{x}$ as determined by the periodic part of the electron Bloch function $u_{\mathbf{k},n}(\mathbf{x})$, and second, a polarization that arises from the phase ϕ of the transition dipole between the bands m and n that are related by the transition matrix element $M^j_{nm}(\mathbf{k}) = |M^j_{nm}(\mathbf{k})| e^{-\mathrm{i}\phi_{nm}(\mathbf{k})}$. If $\phi_{nm} = 0$, the shift of Eq. (2.18) is equivalent to the shift component in the population model (Eq. (2.10)) [Sip00].

In contrast to shift currents, *injection currents* vanish for linear polarized light and are only non-zero for elliptical polarized light:

$$\sigma^{\text{inj}}_{ijk}(0;\omega,-\omega) = \frac{\pi e^3}{2\hbar^2}\int \frac{\mathrm{d}^3\mathbf{k}}{8\pi^3}\sum_{n,m} f_{nm}(v^i_{nn} - v^i_{mm})[M^k_{mn}M^j_{nm} - M^j_{mn}M^k_{nm}]\delta(\omega_{nm}-\omega). \tag{2.19}$$

σ^{inj} scales with the band velocity difference between ground and excited state $(v^i_{nn} - v^i_{mm})$, and requires mixing of fields polarized along j and k that interfere when following different excitation pathways, e.i., $[M^k_{mn}M^j_{nm} - M^j_{mn}M^k_{nm}] \neq 0$ [Sip00].

A relationship similar to Eq. (2.17) and 2.17 can be provided for *optical rectification* [Nas06], which is a transient charge displacement that arises from nonresonant coupling of pairs of states whose energies differ from the incident photon energy. A process that requires the presence of the pump pulse inducing a transient superposition of Bloch states.

3 The Tool: Ultrafast THz electromagnetic pulses

Laser sources provide strong light fields that can drive a nonlinear response of matter. Consequently, light waves start interacting with each other, resulting in exchange of momentum and energy. Optical fields are generated at new frequencies, including optical harmonics as well as sum- and difference-frequency signals.

The difference-frequency component that oscillates much slower than the incident light can be employed for down conversion to terahertz (THz) frequencies. Similarly, such temporal modification of the material polarization can be detected by a subsequent weak probe pulse, a process that can be used to detect THz pulses or study charge carrier and lattice dynamics of an excited medium.

In the previous chapter we discussed second order nonlinear effects in the time domain and switched only to the frequency domain when necessary. Since generation and detection of THz fields is understood as nonlinear mixing of frequency components of light pulses, it is instructive to discuss light conversion in this chapter in the frequency domain.

3.1 Nonlinear light conversion

When an external bias field is applied to an material, its electronic charges get displaced. The induced charge displacement (polarization) can be viewed as a classical oscillating dipole that itself emits radiation at the oscillation frequency. Strong fields can even drive such polarization in the nonlinear regime. To lowest order the nonlinear polarization $\mathbf{P}$ scales with the field $\mathbf{E}$ squared. With assumptions as discussed for the time domain description (Eq. (2.8)), we can write down the spatially local response

$$P_i^{(2)}(\omega) = \sum_{jk} \int_{-\infty}^{\infty} \mathrm{d}\omega_1 \int_{-\infty}^{\infty} \mathrm{d}\omega_2 \chi_{ijk}^{(2)}(\omega;\omega_1,\omega_2) E_j(\omega_1) E_k(\omega_2) \tag{3.1}$$

$\chi_{ijk}^{(2)}(\omega;\omega_1,\omega_2)$ is the third-rank susceptibility tensor. For convenience we restrict ourselves to positive frequencies ω, ω_1, ω_2 and exploit general symmetry properties of $\chi^{(2)}$ to decompose $P_i^{(2)}$ into two components

$$\begin{aligned} P_i^{(2)}(\omega) = 2 \sum_{jk} \int \int_{\omega_1>\omega_2>0} \mathrm{d}\omega_1 \mathrm{d}\omega_2 \\ \underbrace{\chi_{ijk}^{(2)}(\omega;\omega_1,\omega_2) E_j(\omega_1) E_k(\omega_2)}_{\text{SFG}} + \underbrace{\chi_{ijk}^{(2)}(\omega;\omega_1,-\omega_2) E_j(\omega_1) E_k^*(\omega_2)}_{\text{DFG}} . \end{aligned} \tag{3.2}$$

The first term describes sum-frequency generation (SFG), whereas the second term is

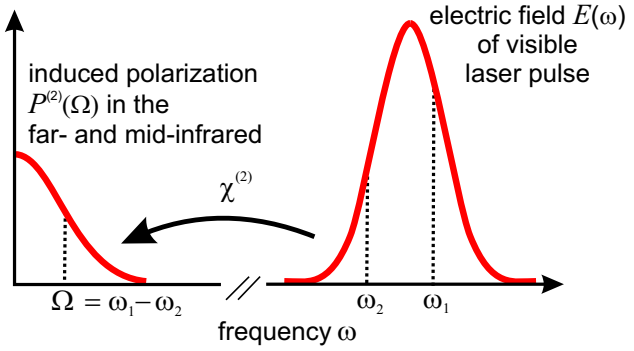

Figure 3.1: Frequency down conversion. Each frequency pair $(\omega_1, -\omega_2)$ within the spectral bandwidth of the driving pulse $\mathbf{E}$ induces a polarization $\mathbf{P}^{(2)}$ at frequency $\Omega = \omega_1 - \omega_2$.

the difference-frequency component (DFG). The photocurrent response (Eq. (2.8)) can be obtained from Eq. (3.2) by accounting for the timederivative that relates the second-order susceptibility $\chi^{(2)}$ and the conductivity tensor $\sigma^{(2)}$, $\mathbf{J} = \partial\mathbf{P}/\partial t$.

3.1.1 THz Generation

DFG can down convert optical pulses to THz frequencies $\Omega = \omega_1 - \omega_2$ (Eq. (3.2)). Within the bandwidth of the excitation all pairs of ω_1 and ω_2 induce a polarization $\mathbf{P}(\Omega)$ that itself emits radiation at frequency Ω. As depicted in Fig. 3.1 the bandwidth of the excitation pulse determines the bandwidth of the generated THz pulse. For instance, driving pulses from a Ti:Sa laser provide 100 nm ($\approx$ 50 THz) broadband pulses centered at 790 nm ($\approx$ 400 THz) that can, in principle, generate THz pulses covering a spectrum from 0 to 50 THz. However, in real crystals the total THz field $\mathbf{E}^{\mathrm{THz}}(\mathbf{x},\omega)$ is a coherent superposition of fields induced by polarizations $\mathbf{P}^{(2)}(\mathbf{x}',\omega)$ generated along the excitation path throughout the crystal. Consequently, constructive interference is required to generate a sizeable field. The total field is given by

$$\mathbf{E}^{\mathrm{THz}}(\mathbf{x},\omega) = -4\pi\frac{\omega^2}{c^2}\int \mathrm{d}^3\mathbf{x}' G_{\mathbf{x}'}(\mathbf{x},\omega)\mathbf{P}^{(2)}(\mathbf{x}',\omega) \tag{3.3}$$

where $G_{\mathbf{x}'}(\mathbf{x},\omega)$ is the propagation function that is an outgoing spherical harmonic as depicted in Fig. 3.2 for the simple case of a spatially homogenous and isotropic medium. Effectively only those components contribute to $\mathbf{E}^{\mathrm{THz}}(\mathbf{x},\omega)$ that propagate in phase with the group velocity of the excitation. This condition is best fulfilled in isotropic media with frequency-independent refractive index. In real materials, however, a frequency-dependent refractive index causes interference, and only "phase-matched" frequency components contribute to $\mathbf{E}^{\mathrm{THz}}$. Details on the calculation of THz emission from GaP and ZnTe are given in Appendix 6.A.

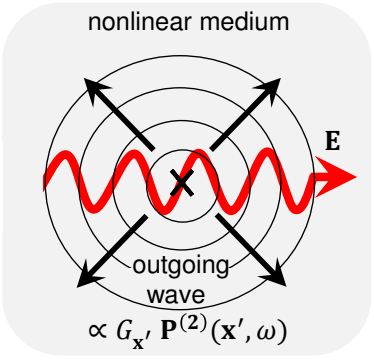

Figure 3.2: Example of an elementary THz wave. The visible pump field $\mathbf{E}$ propagates through the nonlinear medium, thereby inducing a microscopic polarization $\mathbf{P}^{(2)}$ at each point $\mathbf{x}'$. All fields generated along the propagation path add to the macroscopic field $\mathbf{E}^{\mathrm{THz}} \propto G_{\mathbf{x}'}\mathbf{P}^{(2)}(\mathbf{x}',\omega)$.

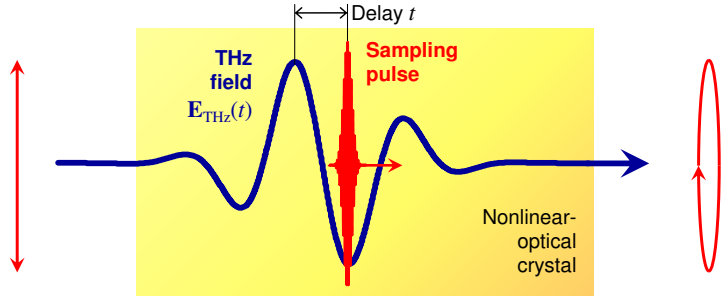

Figure 3.3: Electro-optic sampling of a THz waveform $\mathbf{E}^{\mathrm{THz}}$ with a short optical gate pulse. The THz field induces a transient birefringence of the detection crystal via the linear electrooptic effect that changes the polarization state of a co-propagating time delayed sampling pulse. The detection process is most efficient for THz frequencies with a phase velocity that matches the group velocity of the sampling pulse.

3.1.2 THz detection

THz radiation can be detected by SFG and DFG mixing of a THz field $\mathbf{E}^{\mathrm{THz}}$ and a short visible pulse $\mathbf{E}$ that co-propagate through a crystal with $\chi^{(2)} \neq 0$ (Eq. (3.2). $\mathbf{E}^{\mathrm{THz}}$ effectively modulates the refractive index of the detection crystal, which consequently changes the polarization of the optical pulse. In this way, the THz field information is transferred to the polarization state of the sampling pulse.

In more detail, this electrooptic or Pockels effect is caused by the nonlinear polarization induced by propagation of the total field $\mathbf{E} = \mathbf{E}^{\mathrm{THz}} + \mathbf{E}$ in the detection crystal. The relevant cross term $P_i^{(2)} \propto \sum_{jk} \chi_{ijk}^{(2)} E_j^{\mathrm{THz}} E_k$ corresponds to an electric polarization that is linear in $\mathbf{E}$ and $\sum_j \chi_{ijk}^{(2)} E_j^{\mathrm{THz}}$ is a change of the linear optical properties in response to $\mathbf{E}^{\mathrm{THz}}$.

The change in the linear crystal response along the THz field axis induces a transient birefringence that can be measured by a co-propagating time-delayed visible sampling pulse. As illustrated in Fig. 3.3 the transient birefringence induces a perpendicular probe-field component that results in an ellipticity of the probe-polarization. The polarization change is detected as intensity modulation on a pair of balanced photodiods behind polarizing

optics. As the THz generation, also the efficiency and bandwidth of the detection process is limited by propagation effects.

4 Experimental setup

In this work, ultrafast THz spectroscopy is used (i) to excite and detect ultrafast photocurrents and (ii) to drive electrical currents with intense THz pulses. Their investigations are highly relevant for ultrafast opto-electronics and electrical currents pushing clock rates of data processing towards THz frequencies. Concept (i), THz emission spectroscopy, is illustrated in Fig. 4.1a. An optical femtosecond laser pulse is incident on matter, where it excites a photocurrent. The accelerated charges re-emit radiation at THz frequencies that can be detected by optical means. The experimental configuration (ii) is depicted in Fig. 4.1b. In a pump-probe configuration, illumination of a sample with intense THz pulses drives an electrical current. A subsequent optical pulse monitors the pump induced change of the linear material properties.

The two concepts call for laser sources driving the THz setups optimized for the experimental needs. Concept (i) requires extreme laser stability and signal to noise ratio (SNR) to detect the small photocurrent signals. In contrast, (ii) aspires for highest available field strength and high SNR as well. This chapter will introduce the used laser systems and THz sources as well as the novel modulation technique that was developed to detect small amplitude signals only limited by shot noise.

4.1 The THz emission spectrometer

The ultrafast amperemeter for photocurrent measurements is depicted in Fig. 4.2. Visible laser pulses (20 fs, 11 nJ, 75 fs) from a MHz oscillator are tightly focused onto a sample. A potentially emitted THz field is collected by a parabolic mirror and sent to a detection crystal, e.g., ZnTe.

As discussed in Section 3.1.2, the THz field is detected by the induced transient birefringence of the detection crystal that changes the polarization of co-propagated visible sampling pulses from initially s to elliptically polarized. Behind the detection crystal, quarter and half wave plates transform the unperturbed gate polarization to 45°. A polarizing beam splitter cube then splits the pulses in s and p polarized components that are equally intense if no THz radiation is present. Power detection by a pair of balanced photo diodes eliminates intensity fluctuations of the gate pulses, but THz signal-induced polarization changes are converted into a current difference on the diodes. The complete THz waveform is scanned by a fast, continuously moving translation stage that delays the train of the THz pulses with respect to the train of gate pulses. To detect signals from THz-opaque materials, the setup can be easily modified to measure samples in reflection and 45° angle of incidence.

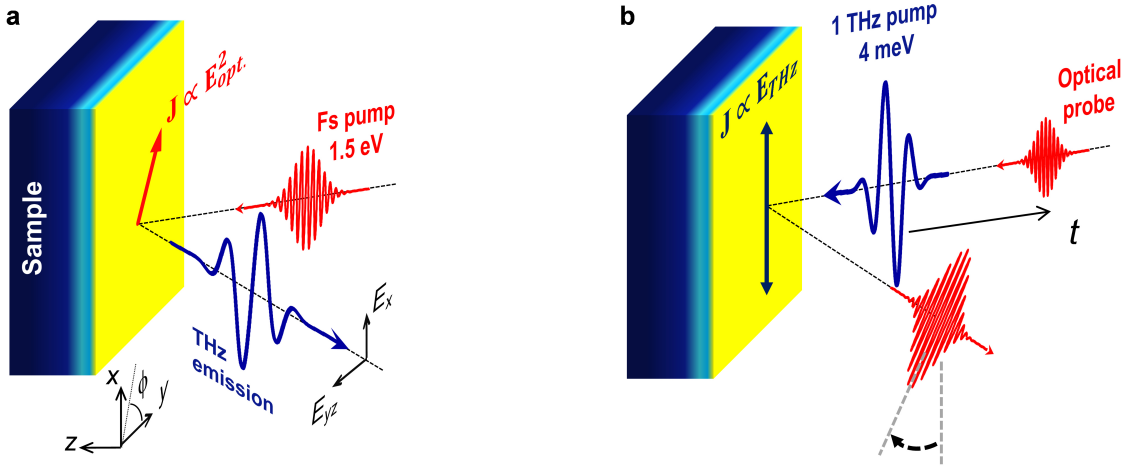

Figure 4.1: The two concepts of THz spectroscopy used in this work. **a**, Illustration of THz emission spectroscopy. An 20 fs optical pulse is incident on a sample. The ultrafast stimulus launches a short current burst that emits THz radiation. The detection of this THz radiation provides inside into the photocurrent dynamics by calculating the source current from the emission signal. **b**, A THz field-transient drives an electric current inside a sample. The induced carrier dynamics are sampled with a time-delayed probe pulse in the optical or THz (not shown) frequency range that monitors the pump-induced change in the dielectric function.

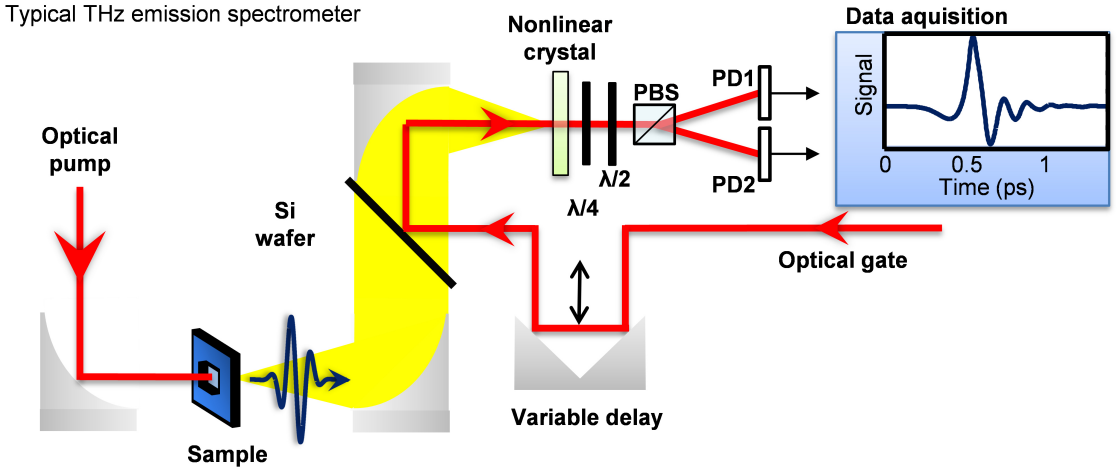

Figure 4.2: THz spectrometer. A near-infrared pulse from a Ti:sapphire laser generates THz radiation in a nonlinear crystal. The emitted THz radiation is collimated by a 90° off-axis parabolic mirror. The remaining pump light is blocked by a high-resistivity Si wafer that transmits THz pulses and combines the THz pulses with near-infrared sampling pulses such that both propagate collinearly through the detector. In the nonlinear crystal, the THz-induced birefringence causes elliptical polarization of the gate pulses that is detected by using a combination of $\lambda/4$ and $\lambda/2$ wave plates and a polarizing beam splitter (PBS) that sends perpendicular polarization components to a pair of balanced photo diodes (PD1,PD2).

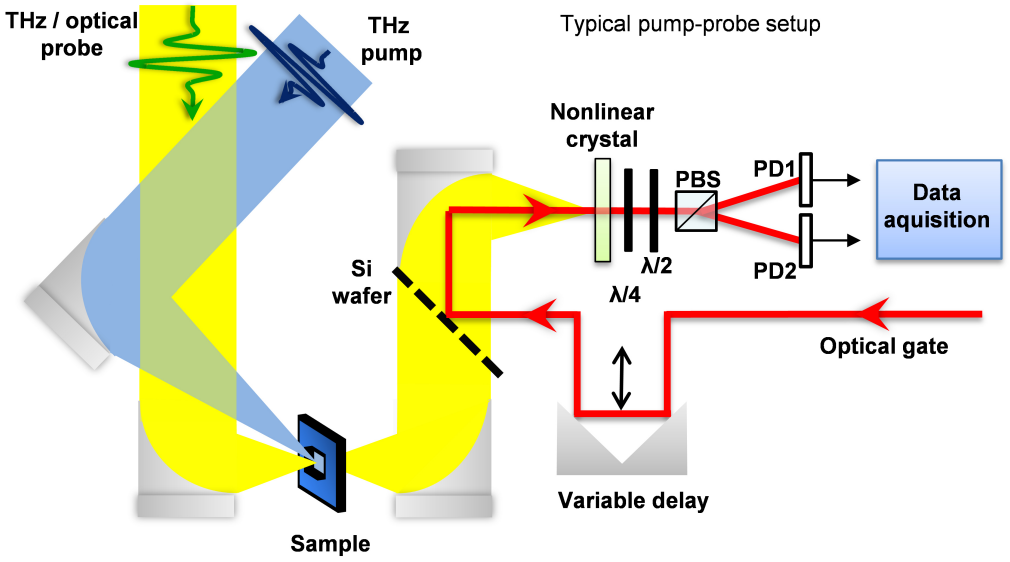

Figure 4.3: Pump-probe setup. The sample is excited by intense THz pump pulses from either the $LiNbO_3$ 1 THz or the Multi-THz source. After a delay, a weak probe pulse in the visible or THz frequency range interacts with the sample, thereby gaining information about the current sample state. Pump and probe propgate non-collinear to spatially separate these pulses before the detection. For THz probing the detection is analogue to Fig. 4.2. For an optical probe the Si wafer and the detection crystal are removed and probe-polarization changes are detected with half or quarter wave plates before the balanced photodiods.

4.2 The THz transmission spectrometer

Prior to time-resolved experiments, samples are characterized by broadband THz transmission measurements. For this purpose, a similar setup to the one described in Section 4.1 and Fig. 4.2 is used to detect the linear response of a sample at THz frequencies. The THz transmission spectrometer has an additional focus before the sample, where THz pulses are generated in a nonlinear crystal, e.g., ZnTe. Subsequently, the THz pulses are transmitted through the sample and sent to the detector.

For such single excitation pulse applications the “MHz setup” is well suited as it provides high signal to noise ratio.

4.3 The THz pump-probe setup

The second class of experiments performed in this work uses intense THz pulses to drive an excitation and probes the subsequent dynamics with a second probe pulse co-propagating through the sample, as illustrated in Fig. 4.3. Sampling pulses are either directly visible pulses or a second weak THz probe pulse train is generated. Pump and probe beam are sent to the sample non-collinear to spatially separate both beams at the detector position. Optical probe pulses are detected directly with polarizing optics and a pair of balanced photo diodes, while THz probe pulses require electro-optic sampling detection as described above.

4.4 The laser and the THz sources

THz generation by light conversion of optical fields imposes stringent technological requirements on suitable laser systems. The optical driving pulses have to be optimized addressing the following issues:

- **Bandwidth.** The THz center-frequency and bandwidth are determined by the optical excitation bandwidth. Broadband radiation is especially desired for spectroscopic applications. 10 fs pulses naturally meet the bandwidth requirement and are also short enough to detect THz frequencies from ~ 1 to 50 THz. In contrast, extremely intense narrowband THz radiation requires convenient tune ability of the excitation to match the desired difference frequency.
- **Stability.** Detection of small signals close to the ultimate "shot noise" limit require extreme stability of the laser pulses. As any additional component, such as laser amplifier, may cause additional noise, the system should be as simple as possible.
- **Repetition rate.** The modulation technique employed in the newly developed fast-scan THz detection (Section 5.2.3) pays off most at modulation frequencies above 10 kHz, thereby setting a lower limit on the repetition rate of the laser source.
- **Pulse energy.** The application of THz pulses to drive matter into the nonlinear regime requires extreme pulse intensities which are beyond the reach of stable femtosecond oscillators operating at high repetition rate.

The requirement of high stability and large bandwidth for THz emission spectroscopy is best fulfilled by a simple high-repetition rate system. Therefore, we use a MHz-laser oscillator that provides extremly stable 10 fs, 11 nJ pulses at 75 MHz repetition rate to drive our THz emission spectrometer developed to operate at the fundamental "shot noise level". In contrast, a kHz-amplified laser providing 40 fs, 15 mJ pulses at 1 kHz repetition rate drives our high-field THz sources to excite samples with > 1 MV/cm fields at 1 THz and > 30 MV/cm at 25 THz.

4.4.1 MHz-Laser Oscillator

Our laser oscillator is illustrated in Fig. 4.4. The light-amplification medium is a titanium-doped sapphire crystal that is pumped by a continuous wave Nd:YVO_4 laser at 532 nm. The Ti:sapphire provides emission over a very broad band from 670 to 850 nm [Fer02b]. The very broad gain profile originates from a homogeneous fluorescence band between 670 - 1070 nm and the design of the laser cavity of length l, which favors only longitudinal modes with an equidistant frequency spacing $\Delta f = c/2l$.

For pulsed operation, the phases of these modes have to be locked, which requires the modulation of a cavity parameter with frequency Δf. Passively such modulation is achieved by the optical Kerr-effect in the Ti:sapphire crystal. Due to the linear intensity dependence of the Kerr-effect, the Gaussian beam profile induces a lateral refractive index modulation, which allows in phase propagation of multiple modes. Acting as a transient lense [Fer02b], the lateral refractive index modulation favors the amplification of the most intense modes.

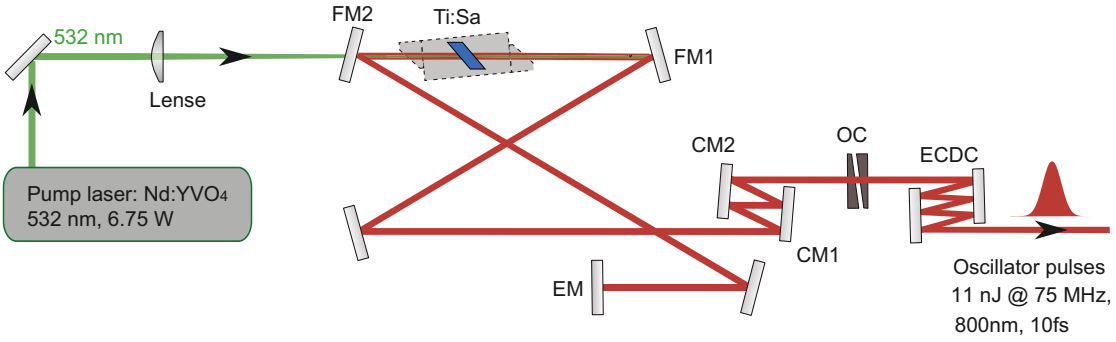

Figure 4.4: MHz-laser oscillator (Femtosource M1, Femtolasers GmbH). A continuous-wave, 532 nm, Nd:YVO_4 laser pumps the light-amplifying Ti:sapphire crystal. The optical resonator is formed by the end mirror EM and the slightly transmitting output coupler OC. A high power density in the crystal is achieved by the focusing mirrors FM1 and FM2. The dispersion along the cavity path is compensated with a pair of chirped mirrors CM1 and CM2. The double-wedge chape of the OC avoids multiple reflections into and out of the resonator. The wedges and the external cavity dispersion control ECDC, pair of chirped mirrors, can be adjusted to optimize the pulse dispersion according to optical elements in the setup.

The light intensity profile is extremely important for the laser operation and "chirped mirrors" are required to compensate for pulse dispersion. Good dispersion management allows for the generation of ultra-short 20 fs pulses. Details of the femtosecond laser-oscillator used are described in Fig. 4.4.

4.4.2 kHz-Amplified Laser System

Very high laser fields are obtained by amplifying the MHz oscillator pulses in another Ti:sapphire crystal. Since the Ti:sapphire sets an output power limit of 1-10 W, the repetition rate of the amplifier system is reduced to 1 kHz to allow for high peak amplitudes. To prevent undesired nonlinear processes or even damage of optical elements, the pulses are temporally stretched prior to amplification and compressed afterwards. Fig. 4.5 shows the kHz amplified laser system used in this work.

The amplified pulses are either directly used to drive our 1 MV/cm THz radiation source or sent into an optical parametric amplifier (OPA), which generates pulses with a central wavelength tunable in the visible spectral region. An OPA transfers intensity from a pump beam (of frequency ω_{pump}) to a signal beam ω_{s} that needs to be amplified by a nonlinear process according to Eq. (3.2). This parametric amplification process works by repeated difference-frequency mixing. First, an idler beam $\omega_{\text{i}} = \omega_{\text{pump}} - \omega_{\text{s}}$ is generated and second $\omega_{\text{s}} = \omega_{\text{pump}} - \omega_{\text{i}}$ is amplified. Wide tunability of the output wavelength is achieved by choosing the incoming weak seed pulse ω_{s} from a white-light continuum generated from a small portion of the pump pulse. A twin system of two OPAs tuned typically to wavelength 1200 nm and 1400 nm delivers the pump pulses for the Multi-THz source.

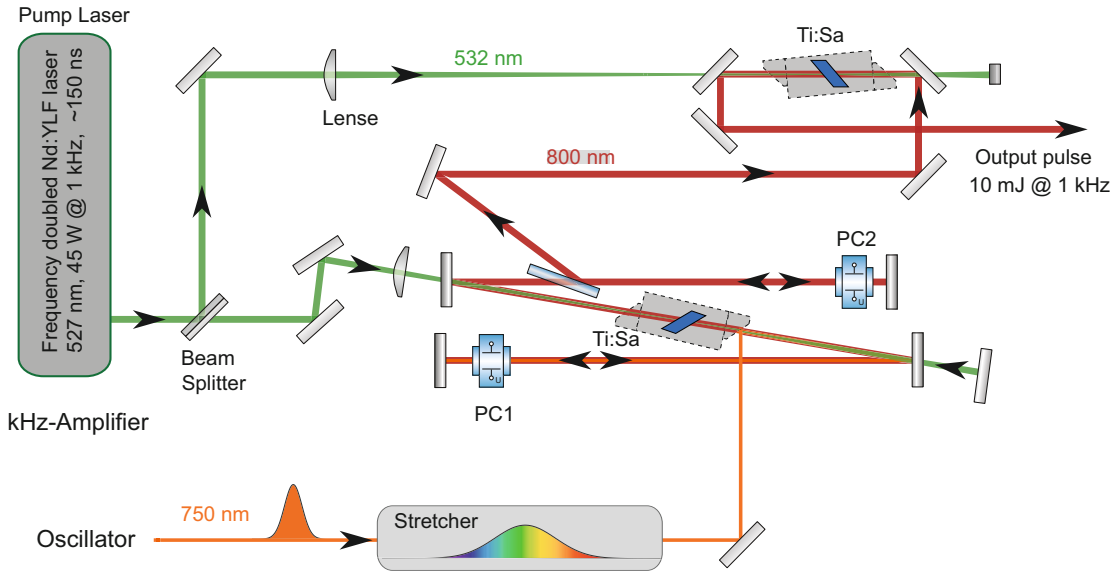

Figure 4.5: kHz-laser amplifier (TOPAS Legend Elite Cryo, Coherent GmbH). Seed-laser pulses (8 fs,75MHz) from a laser oscillator similar to Fig. 4.4 are temporally stretched. Pockels-cell pulse picker PC1 and PC2 allow only every kHz shot to pass the two amplification stages, that consist of two individual Ti:sapphire crystals pumped by a Nd:YLF laser. 800 nm, 10 mJ output pulses at 1 kHz are subsequently split compressed to 40 fs as input for the twin OPA system.

4.4.3 The THz sources

The generation of intense THz pulses is based on DFG (see Eq. (3.2)) and requires a large nonlinear coefficient of the conversion media. Among the strongest nonlinear coefficients are found in GaP (0.97pm/V), ZnTe (3.9pm/V), GaSe (14.4pm/V) and $LiNbO_3$ (33.3pm/V). In addition, the excitation pulse has to propagate in phase with the THz field inside the nonlinear generation medium, thereby setting limits for the application of different crystals.

Broadband THz pulses: GaP/ZnTe

GaP and ZnTe illuminated with 20 fs laser pulses at 790 nm provide very broadband THz pulses ranging from 0.3 to 40 THz. Coincidental phase matching enhances signal contribution below 3 THz in thick crystals, while above 3 THz random phase matching dominates the emission signal. Therefore, the broadband emission has a strong band below 3 THz whose amplitude can be reduced by using thin crystals. THz absorption that always limits THz generation in the vicinity of fundamental phonon resonances, occurs in these crystals only in a very narrow range of the Reststrahlen band. The unperturbed emission range is in GaP even larger than in ZnTe.

This THz source is used in this work to calibrate the THz emission spectrometer to allow the extraction of source currents from THz signals.

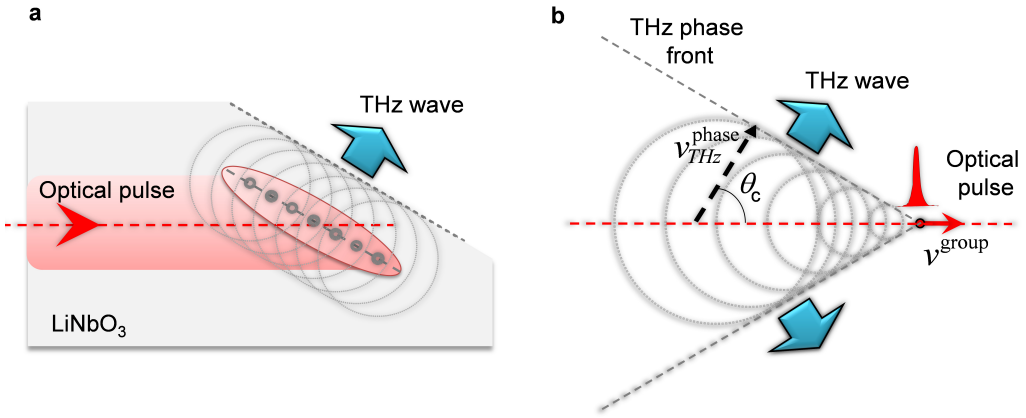

Figure 4.6: THz generation in $LiNbO_3$. **a**, The pulse front of the spatially extended optical excitation is tilted to achieve an in phase propagating THz pulse front. Efficient THz field outcoupling requires an optimized crystal cut angle. **b**, Phase matching in $LiNbO_3$ by formation of a shock wave, illustrated for a point like optical pump pulse with a group velocity much higher than the THz phase velocity, $\mathbf{v}_{\mathrm{THz}}^{\mathrm{phase}} < \mathbf{v}^{\mathrm{group}}$. The shock wave is formed due to the large difference in the refractive index at optical and THz frequencies in $LiNbO_3$.

Strong THz pulses at 1 THz: $LiNbO_3$

Intense THz fields of ∼1 MV/cm field strength centered at 1 THz can be generated in $LiNbO_3$ [Heb02] having an extremely high nonlinear coefficient (33.3pm/V). To achieve phase-matched THz emission the pump pulse front has to be tilted as shown in Fig. 4.4.3a. Phase matching is achieved by exploiting the fact that in $LiNbO_3$ the THz phase velocity is significantly lower than the excitation pulse propagation velocity, $\mathbf{v}_{\mathrm{THz}}^{\mathrm{phase}} < \mathbf{v}^{\mathrm{group}}$, and consequently a THz shock- or Cherenkov wave is formed that has a front as illustrated in Fig. 4.4.3b. To collect the phase matched THz light the crystal has to be cut along this phase front angle.

Strong THz pulses at ∼25 THz: GaSe

An extremly intense multi-THz source is driven by two incident beams from the two OPAs tuned to provide the desired THz difference frequency. Phase matching between the two driving fields and the THz wave is achieved by mixing them in GaSe, which is birefringent. The difference in the refractive index between ordinary and extraordinary axis can be used to tune the phase matching condition by rotating the crystal. For details see Ref. [Hub00]. The source delivers THz pulses that are highly tunable with the frequency difference of the incident light pulses and crystal orientation. Maximum fields of ∼ 30 MV/cm are delivered at ∼ 25 THz [Sel08].

5 Low noise data acquisition

In our THz spectrometer optical signals are transformed to a current difference at the balanced photo detection, $\Delta I = I_1 - I_2$. Such current signals ΔI carry the actual measurement signal S and parasitic effects such as intensity fluctuation of the probe pulses or pointing instabilities. To obtain S at good signal to noise ratio, the data acquisition has to suppress parasitic effects as good as possible. In the following the data acquisition methods of the two laser systems are introduced with focus on the 75 MHz system, which presents an important development made in the course of this work.

5.1 DAQ "kHz setup"

In the "kHz setup", THz pump pulses are generated with a repetition rate of 1 kHz, but the oscillator sends a probe pulse train with 75 MHz repetition rate. Therefore, only one of the MHz-probe pulses carries the desired signal ΔI_j and all other probe pulses measure noise. Thus, subtracting the previous ΔI_{j-1} or the subsequent ΔI_{j+1} probe pulse from ΔI_j suppresses the noise floor ($<$ 75 MHz). This is performed by a passive electronic difference loop, which subtracts any pair of subsequent 75 MHz pulses, $\delta_j = \Delta I_j - \Delta_{j+1}$. The only two remaining pulses $\delta_1 = -\delta_2$ carry the desired signal with strongly reduced noise floor. These signals are amplified and send to the computer, where fast digitizer card (100 MHz) allows to sample both signals individually for further analysis.

5.2 DAQ "MHz setup"

In the "MHz setup" every MHz pulse carries a signal and the procedure described above is not feasible. A general current difference signal ($I_1 - I_2$) on the photo diodes is

$$S(t) = I_1(t) - I_2(t) = s(t) + n(t), \tag{5.1}$$

where s is the real pump induced signal and n is noise. External noise sources are omnipresent in all measurements and the noise power spectrum of our setup presented in Fig. 5.1 shows that below 10 kHz the spectrum is dominated by acoustic and 1/f noise that is typical for electronic devices. Above 10 kHz the fundamental shot noise is the only limitation and, thus, signal detection beyond 10 kHz is desired.

To measure signals only limited by shot noise, we developed a new data acquisition technique that allows the detection of extremely small signals. The operation principle combines the strengths of two data acquisition concepts established for high repetition rate laser systems, namely (i) rapid-scanning schemes using a fast delay stage to sample signals in the time domain and (ii) step-scan schemes using lock-in amplifiers to extract rapidly modulated signals.

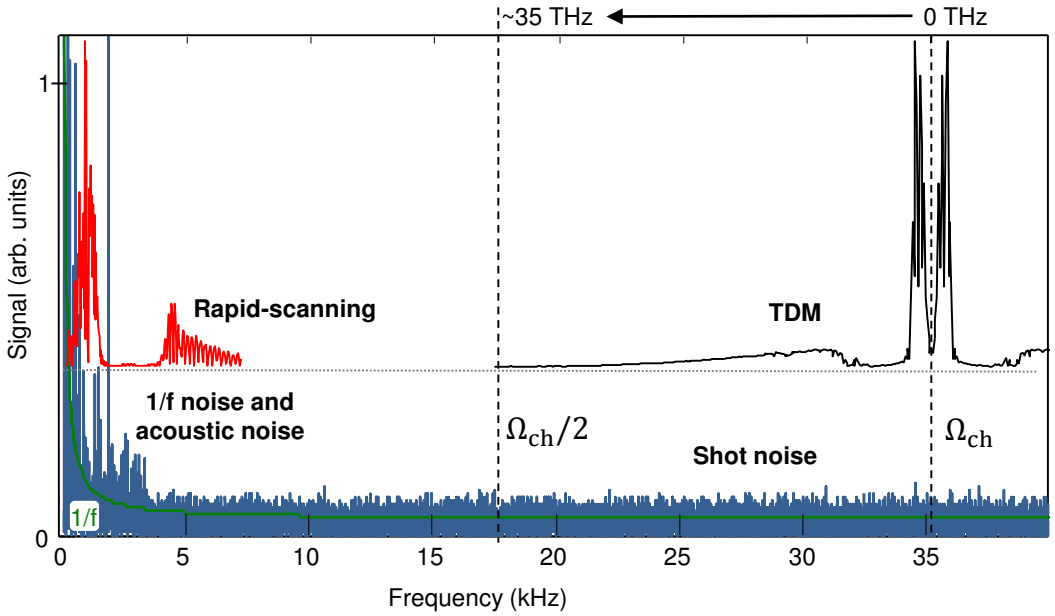

Figure 5.1: Noise power spectrum and rapidly scanned THz signals. The noise power spectrum of the "MHz setup" shows acoustic and 1/f noise that dominates the spectrum below 5 kHz. Above 10 kHz noise is constant at the shot noise limit. THz signals, ranging from 0.3 to 35 THz, obtained for rapid-scanning only (red), and the first sideband of rapid-scanning with $\Omega_{\mathrm{ch}} = 36$ kHz modulation (black) used for data aquisition in the time-domain multiplexing (TDM) technique, as they appear in the electronic signal spectrum. Curves are offset for clarity.

5.2.1 Rapid delay scanning

In our setup a fast delay sweep is implemented by a sinusoidal oscillating retro-reflector that spans a time window of up to 40 ps with a repetition rate of 25 Hz. A fast digitizer card reads the photodiod current with a 2 MHz sampling rate, which results in 2 MHz/(2 · 25 Hz = 40000 data points per unidirectional scan. The factor two accounts for forward and backward motion.

To process the data the acquisition procedure is as follows. First, all waveforms measured in a given total measurement time window are averaged. Second, the time axis is transformed from real time t to the non-equidistant axis τ given by the shaker motion. Finally, forward and backward motion of the shaker are split and averaged again over the two directions. Thus, the complete measurement time is used and the duty cycle is 100%.

To determine the signal to noise ratio, we measured the resulting THz waveform signal S_{THz} and also the noise background with blocked THz signal as shown for the Fourier transformed signals in Fig. 5.1. The signal spectra reveal that S_{THz} still has significant overlap with the increased noise level below 5 kHz. An even faster scanning is difficult with mechanical delay lines that suffer from uncertainties in the positioning reproducibility and inaccurate position readout. Therefore, another signal modulation is required that shifts the signal to higher frequencies. This modulation is exactly the idea of the ubiquitous lock-in scheme.

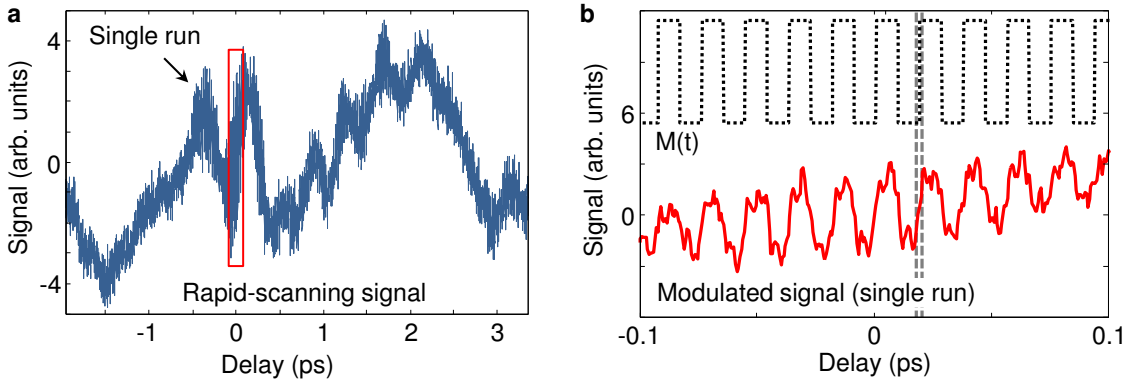

Figure 5.2: Modulation of rapidly scanned signals. **a**, Raw signal S obtained in a single run (only forward scan) of the 25 Hz rapid-scanning unit. The signal consists of 40000 data points converted from the photo detector output by an analogue to digital converter operating at 2 MHz. The desired signal s has components oscillating with a time period in the range of 3 ps to 30 fs (real-time axis not shown). **b**, Zoom into 200 fs time window (delay time, box in **a**) that shows the signal modulated with $M(t)$ induced by a mechanical chopper with $\Omega_{\text{ch}} \approx 36$ kHz. The rectangular periodic dotted line shows the modulation function $M(t)$ simultaneously optically detected. For demodulation, $D(t)$ is obtained from $M(t)$ with the temporal regions of ill defined chopper state (vertical lines) set to zero. Curves are offset for clarity.

5.2.2 Step scan, lock-in detection

Lock-in detection uses fast modulation to shift signals to higher and less noisy frequencies. In our setup, modulation of the optical beam by a mechanical chopper results in a signal

$$S(t) = I_1(t) - I_2(t) = s(t)M(t) + n(t). \tag{5.2}$$

The modulation function $M(t)$ is approximately periodic with frequency Ω_{ch} and each period has an approximately rectangular shape with a duty cycle of ≈ 0.5. $M(t)$ is shown in Fig. 5.2b as obtained by a photo diode monitoring the status of the optical chopper.

It is instructive to consider the frequency spectrum of $S(t)$,

$$\tilde{S}(\omega) = \sum_j A_j \tilde{s}(\omega - j\Omega_{\text{ch}}) + \tilde{n}(\omega). \tag{5.3}$$

Here, A_j is the Fourier amplitude of the j-th harmonic of the periodic function M with $A_j \propto (e^{i\pi j} - 1)/i\pi j$. Therefore, $\tilde{S}(\omega)$ consists of noise $\tilde{n}(\omega)$ and renormalized copies of the pure signal spectrum $\tilde{s}(\omega)$ centered at harmonics $j\Omega_{ch}$ of the chopper frequency.

A lock-in amplifier (LIA) multiplies S with a harmonic function of frequency Ω_{ch}. Therefore, the modulated signal sM shifts to frequency zero, $\omega = 0$, where it is isolated by a low-pass filter of bandwidth $1/TC$. TC is the time-constant of the LIA that determines approximately the averaging time at a single data point. Note this slow response enforces step-scan detection, that is, go to delay τ, wait for some time (5 TCs) to settle to new signal value s and acquire LIA output. The procedure has to be repeated for every delay position τ. The result shown in Fig. 5.3 has a signal to noise ratio (SNR) clearly better

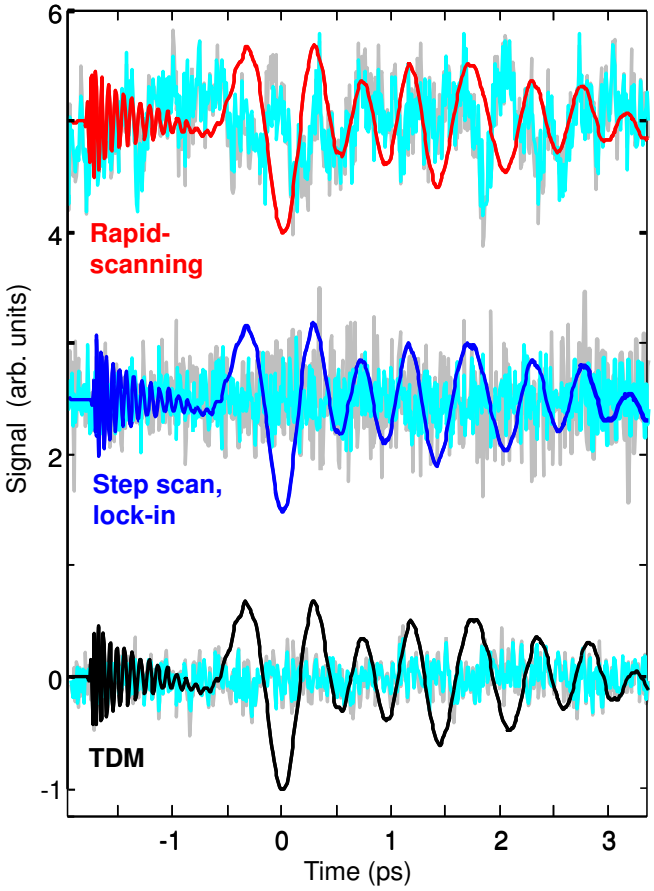

Figure 5.3: Signal to noise ratios (SNR) for three data aquisition schemes under comparable measurement conditions. A signal of a THz transient is superimposed with the background noise scaled by a factor 100 for two total measurement durations: 233 s (grey) and 324 s (blue). The time-domain multiplexing (TDM) scheme is especially useful, when a measurement requires a high SNR in shortest possible time. For instance, within a total measurement time of 233 s a factor of 2 is gained compared to the step-scan, lock-in acquisition (ENBW 6 dB, TC=30 ms, setteling time 150 ms). For optimized lock-in settings (ENBW 24 dB, TC 30 ms, setteling time 300 ms) the setteling time and, thus, the total measurement time (324 s) increases significantly and the SNR ratio with the TDM method is still a factor of ≈ 1.5 higher.

than for the fast scan scheme (Fig. 5.3). However, there is still room for improvement because the duty cycle is quite low, and slow signal changes, such as laser drift or sample degradation can distort a measured waveform in an unnoticed way.

5.2.3 Time-domain multiplexing

The time-domain multiplexing developed here combines the high duty cycle of a rapid-scanning technique with the low noise background of a lock-in modulated signal. Our strategy is to acquire $S(t) = s[\tau(t)]M(t) + n(t)$ over a full cycle of the shaker motion and then process this data set to extract the desired signal $s(t)$ with maximum SNR. This scheme is repeated for subsequent shaker runs. After averaging over all runs, the signal is transformed from t to τ [see Section 5.2.1].

Fig. 5.2b shows an example of signal S and the modulation function M. Variations of S and M are in phase showing that the pump-beam chopper multiplexes the signal S between pump on and off. The modulation M is much faster than the slowly drifting background noise of S, which will allow us to separate signal and $1/f$ noise. By Fourier transformation we obtain the power spectrum $\tilde{S}$ shown in Fig. 5.1. $\tilde{S}$ shows a similar structures at $\omega = 0$ and at the chopper frequency Ω_{ch} and its harmonics. These features are shifted copies of $\tilde{S}$ as predicted by Eq. (5.3). We emphasize that the sideband at $\omega = \Omega_{\mathrm{ch}}$ is already in a spectral region where a constant shot-noise floor is virtually the only noise contribution (see Fig. 5.1). This sideband has the highest of all amplitudes

and, thus, exhibits the best SNR. We extract the sideband by multiplying S with the demodulation function $D(t) = W(t)\sin(\Omega_{\mathrm{ch}}t + \Phi_0)$ and cut out the signal containing time window from $\omega = 0$ to $\Omega_{\mathrm{ch}}/2$. Ω_{ch} and Φ_0 are obtained from the synchronously acquired $M(t)$ which has to be in-phase with $D(t)$. The additionally introduced window function $W(t)$ assumes values of 0 or 1 and is used to set the noise to zero, when the beam is blocked, and also eliminates the ill-defined status of the chopper at times when the pump beam is only partially blocked by the chopper blade.

After averaging and transition from t to τ we obtain the waveform of Fig. 5.3. Note the SNR achieved with our rapid scan time-domain multiplexing scheme is by a factor two larger than with the step-scan scheme. We emphasize that our scheme works online, implemented using LabVIEW, although two million data points have to be processed per second.

6 An ultrafast multimeter for measuring photocurrents and -voltages with 40 THz bandwidth

In this chapter, we present how THz emission spectroscopy can be exploited for photocurrent detection with a time resolution as fast as 20 fs. We show that measurement of the transfer function of a THz emission spectrometer is straightforward by using transparent and broadband GaP and ZnTe crystals as reference emitters. Once the transfer function is known, the THz near-field accompanied by an ultrafast photocurrent in a sample of interest can be determined robustly and reliably.

The development of this reference technique is essential for the ultrafast photocurrent measurements in Chapter 7 and our recent publications in Nature Photonics [Sei16] and Nature Communications [Bra16].

6.1 Motivation

Photoinduced charge currents are ubiquitous in physics, chemistry and biology. Examples include charge separation in photovoltaic materials [Hen04], photochemical reactions in the human eye [Gro08] and ultrafast charge and spin currents in electronic [Lei99a] and spintronic [Kam13a] devices. To study the very first steps of these processes, we need to trigger and detect charge transfer with a time resolution comparable to the time scale of electronic scattering processes, that is, down to a few femtoseconds. Therefore, femtosecond laser pulses are the ideal stimulus to trigger the photoinduced charge transfer (see Fig. 6.1).

The most direct way to access the ultrafast evolution of the charge current is to measure the electromagnetic pulse that is emitted by the moving charges (Fig. 6.1). Once the electric field $E(t)$ directly behind the sample is known as a function of time t, we can in principle calculate back to the source current that has generated $E(t)$. Since the dynamics are triggered by a femtosecond laser pulse, we expect the emitted pulse to cover the full spectrum from zero up to tens of terahertz (THz).

Such THz emission spectroscopy is a very general approach and has been used to study the initial steps of ultrafast photoinduced charge-transfer processes. Examples range from charge transfer in molecules [MCB02, Gro08], electron transport in semiconductors [Lei00], nanostructures [Erh15] and metals [Ram14] over quantum beats of electronic wavepackets in semiconductors [Nus94] to acoustic pulses in multilayers [Arm09]. In addition to such charge dynamics, coherent spin precession [Kan11, Nis12] as well as spin transport [Kam13a, Hér06] were monitored in this contact- and destruction-free manner.

The THz electric field $E(t)$ directly behind the sample and the source current are linearly connected by an impedance whose precise form depends on the geometry and the linear

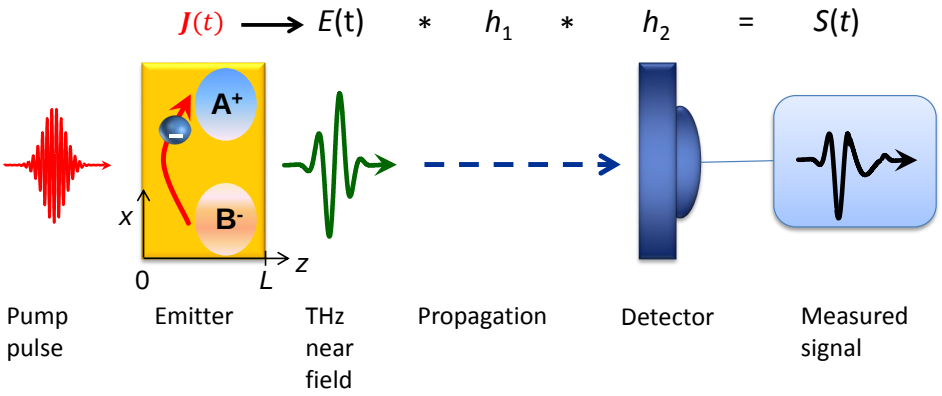

Figure 6.1: Ultrafast photocurrent amperemeter. A femtosecond laser pulse launches a transient photocurrent $J(t)$ in a sample, thereby generating a THz electric field $E(t)$ directly behind the sample. The resulting THz electromagnetic pulse propagates to a detector where its field is electrooptically sampled. The resulting measured signal $S(t)$ and THz near-field $E(t)$ are related by the linear transfer function $h = h_{\mathrm{det}} * h_{\mathrm{prop}}$ which is measured by replacing the sample by a suitable reference emitter.

optical constants of the sample in the THz range [Kam13a]. As calculation or measurement of the sample's impedance is uncritical [Sha04, Wyn05, Sei16], extraction of the THz current from $E(t)$ is straightforward.

Note, however, the THz near-field $E(t)$ is not directly measured in THz emission spectroscopy. Instead, the THz pulse propagates away from the sample to a detector in which its field is sampled, resulting in the signal $S(t)$ (Fig. 6.1). Extraction of the desired $E(t)$ from the actually measured $S(t)$ is a challenging task because the relationship between S and E sensitively depends on the details of the setup, in particular the alignment of the focusing optics and the detector characteristics. Consequently, only a few works [Lei00, MCB02, Kam13a] have made attempts to calculate back from S to E and, eventually, the underlying transient current. To fully exploit the potential of THz emission spectroscopy, a reliable and easy-to-use procedure is required that takes us from the measured signal $S(t)$ to the waveform of interest: the THz near-field $E(t)$ directly behind the sample.

Here, we present a general and robust procedure to extract the THz near-field over a large bandwidth (0.3 to 40 THz) and with excellent (20 fs) time resolution. Our approach is based on suitable reference emitters and a time-domain deconvolution procedure that allow us to determine the transfer function connecting S and E in a reliable way. We anticipate our results will help make THz emission spectroscopy a standard technique to measure ultrafast photocurrents in a contact-free manner.

6.2 Basic principle

A schematic of our THz emission spectrometer is shown in Fig. 6.1. An optical pump pulse (duration of ~ 20 fs) is incident onto the front surface of the sample where it triggers a transient photocurrent. This current, in turn, generates the electric near-field $E(t)$

directly behind the sample's rear interface. Subsequently, the THz electromagnetic pulse propagates over several focusing optics, apertures and filters and is eventually focused onto an electrooptic detector [Fer02a] where its field is sampled by another femtosecond laser pulse, resulting in the actually acquired signal $S(t)$.

Although the processes that take us from $E(t)$ to $S(t)$ are quite complex, it is important to realize that S scales linearly with E. Therefore, the measured signal and the THz near-field are connected by the general linear time-invariant relationship [Kam09]

$$S = h * E = \int \mathrm{d}t' \; h(t - t')E(t'). \tag{6.1}$$

In this convolution, all details of the propagation and detection of the THz wave are captured by the linear transfer function h. In principle, h can be calculated using established models of THz detection [Bak98, Gal99, Lei99b, vdV04, Kam07] and THz wave propagation [Kuž99, Cô3, Fau04, Kam13a, Tom13, Ahm14] that include peculiar effects of sub-wavelength source volumes, apertures and Gouy shift. However, these models rely on idealized assumptions (such as perfectly aligned setups and Gaussian beams) which are difficult to fulfill in practice over the broad bandwidth from 0 to 50 THz. Therefore, we need a method to measure rather than to calculate the transfer function h.

In our approach, we make use of a broadband THz reference emitter that generates a near-field $E_{\mathrm{ref}}(t)$ of known temporal shape. By measuring the resulting reference signal S_{ref} and inverting Eq. (6.1), we obtain the desired transfer function h.

Note the reference emitter has to fulfill important requirements: first, the reference THz beam should exhibit the same spatial characteristics (such as divergence and diameter) as the signal beam emitted from the sample under study. This goal can be achieved with a reference emitter having identical optical thickness as the sample emitter. Second, it should be possible to calculate the reference field $E_{\mathrm{ref}}(t)$ in a reliable manner. In this respect, photoconductors and other pump-absorbing emitters are problematic since their output is noninstantaneous with respect to the driving field and depends on numerous parameters (such as charge-carrier and current relaxation times) which are not easy to determine. In contrast, pump-transparent materials are much better suited as they respond instantaneously to the pump pulse. Therefore, the $\chi^{(2)}$ response function quantifying the photocurrent is often well known and described by just a few parameters [Fau66].

Consequently, we here employ pump-transparent ZnTe and GaP crystals as reference emitters. The choice of a thickness of 50 µm is a compromise. On one hand, the crystals are thin enough to support phase matching over a bandwidth of tens of terahertz. In addition, the relatively small thickness does not lead to notable modifications of the THz beam path. On the other hand, the crystals are thick enough to deliver a THz signal of sufficient strength and to provide a free time window of 1.3 ps until the first generation echo due to reflections at the crystal faces occurs.

6.3 Experimental details

Our sample emitter is a $Co_{40}Fe_{40}B_{20}$ (3 nm)/Pt(2 nm) bilayer on a 0.5 mm thick glass substrate, which provides broadband (0.3-20 THz) emission without spectral features [Sei16] (for details of the THz-emission process see Chapter 8). As reference emitters, we use (110)-oriented 50 µm thick GaP or ZnTe crystals attached to a glass substrate identical to that of the sample film. In the experiment, the THz emitters are excited by linearly polarized laser pulses (duration 20 fs, center wavelength 790 nm, energy 2.5 nJ) from a Ti:sapphire laser oscillator (repetition rate 80 MHz) under normal incidence from the substrate side (beam diameter at sample 50 µm full width at half maximum of the intensity). Laser excitation triggers an in-plane charge current and results in the emission of broadband THz radiation toward the air side of the emitters.

We use 90° off-axis parabolic mirrors to collect and focus the emitted THz wave on an electrooptic crystal of either (110)-oriented GaP (thickness of 250µm) or ZnTe (300µm) [Bak98, Gal99, Lei99b, vdV04, Kam07]. The THz electric field is sampled by copropagating optical pulses (0.6 nJ, 20 fs) from the same laser. The resulting signal $S(t)$ equals twice the THz-field-induced ellipticity of the probe where t is the adjustable delay between the THz and sampling pulse. All measurements are performed at room temperature in a N_2 atmosphere.

The THz near-field $E_{\mathrm{ref}}(t)$ generated by the GaP and ZnTe reference emitters is calculated following the theory of [Vug12] with optical constants taken from Ref. [Lei99b, Die12] (see Appendix 6.A).

6.4 Determining the transfer function

Electrooptic signals $S_{\mathrm{ref}}(t)$ obtained from the GaP and ZnTe reference emitters and the GaP sensor are shown in Figs. 6.2a and 6.2e, respectively. For comparison, the calculated THz near-fields E_{ref} are also shown (Figs. 6.2b,f). They rise almost instantaneously with the duration of the pump pulse (dashed line in Fig. 6.2a) for both reference emitters. In contrast, much slower rise is found for the signal S_{ref}, which can be considered as a clear signature of the transfer function h.

By applying a Fourier transformation to S_{ref} and E_{ref} for GaP and ZnTe, we obtain the amplitude spectra displayed in Figs. 6.2c and 6.2g. Features in the range from 5 to 15 THz coincide with the Reststrahlen band of GaP and ZnTe [Lei99b]. The reduced amplitude of S_{ref} at frequencies above 10 THz attests to a significant low-pass behavior of h.

Since both signal $S_{\mathrm{ref}}(t)$ and field $E_{\mathrm{ref}}(t)$ are known, we extract the transfer function h by inverting Eq. (6.1). We emphasize that this numerical procedure is directly performed in the time domain [Han02] (see Appendix 6.B). The resulting $h(t)$ is shown in Fig. 6.3a for both the GaP and ZnTe reference emitter. Note that the two transfer functions agree excellently, for instance in terms of the slow initial rise, the sharp negative peak at $t = 0$ and the subsequent oscillation. Good agreement is also found in the frequency domain as can be seen by comparing the amplitude and phase of the Fourier-transformed h in Fig. 6.3b.

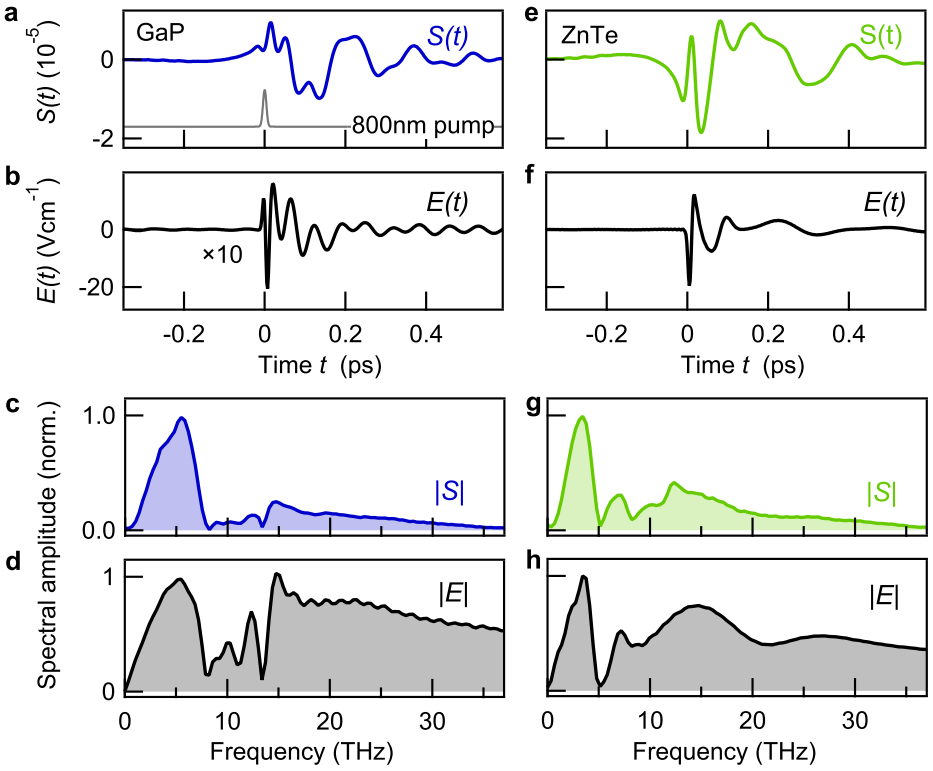

Figure 6.2: THz reference emitter. **a**, Measured electrooptic signal $S_{\mathrm{ref}}(t)$ from the 50 µm thick GaP reference emitter. **b**, Calculated near-field $E_{\mathrm{ref}}(t)$ directly behind the emitter exit face. **c,d**, Amplitude Fourier spectra of the waveforms of **a,b**. Data normalized to peak amplitude. **e-h**, Same as **a-d**, yet for the 50 µm thick ZnTe reference emitter.

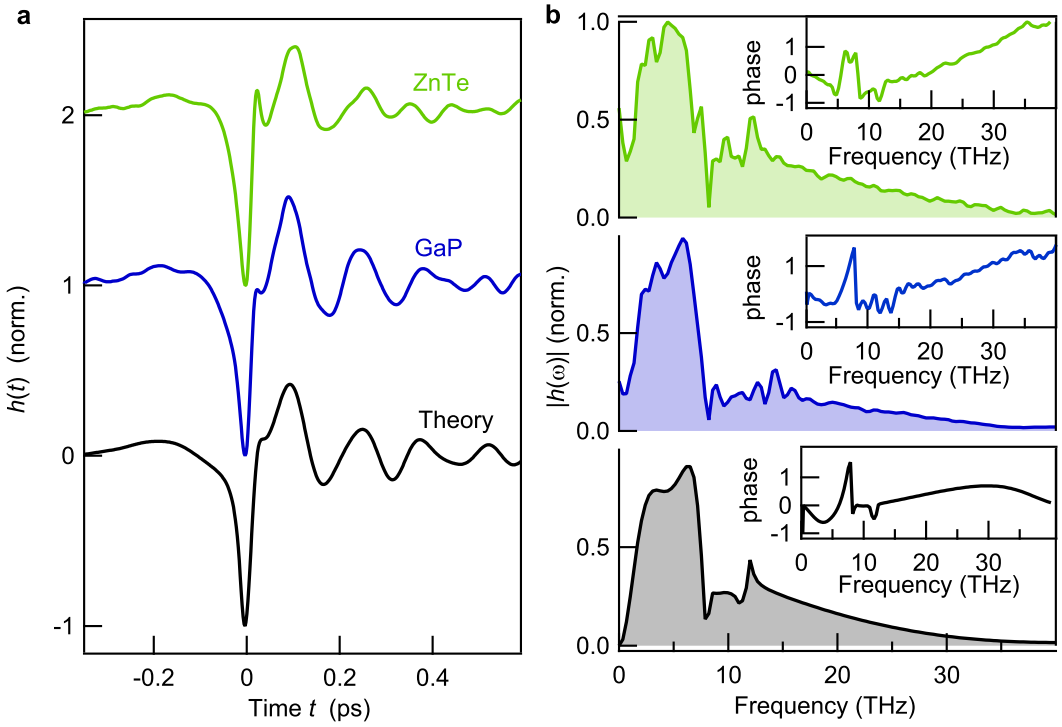

Figure 6.3: Transfer function. **a**, Transfer functions as determined using the measured signal S_{ref} and calculated field E_{ref} of the GaP and ZnTe reference emitter (see Fig. 6.2). Data normalized to peak amplitude (see text). The calculated transfer function is obtained by modeling propagation and electrooptic detection of the THz radiation. **b**, Spectral amplitude and phase spectra of **a**.

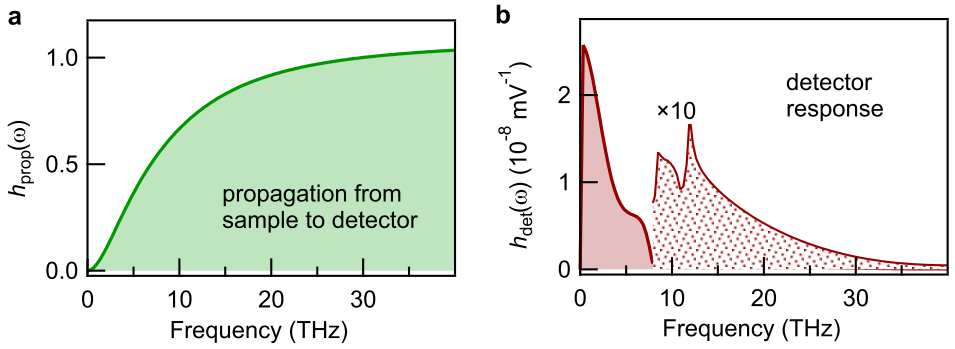

Figure 6.4: Calculated transfer-function components. **a**, Amplitude spectrum of the component h_{prop} describing the propagation from the sample to the electrooptic detection crystal. **b**, Amplitude spectrum of h_{det} which describes the response of the electrooptic detection in 250 µm thick GaP(110) crystal in conjunction with a 20 fs, 790 nm sampling pulse.

These results show that suitable reference emitters permit the consistent determination of the spectrometer transfer function h over the very large bandwidth from 0.3 to 40 THz. The good agreement

6.5 Transfer-function modeling

To gain more insight into the precise shape of the transfer function, we develop a model for the propagation and the detection of the THz pulse, each of which is captured by the transfer function h_{prop} and h_{det}, respectively. As detailed in Appendix 6.C, our modeling accounts for the sub-wavelength diameter of the THz source [Bud98], focusing elements, apertures [Kuž99, Cô3, Fau04, Kam13a, Tom13, Ahm14] and the electrooptic detection process [Bak98, Gal99, Lei99b, vdV04, Kam07]. As seen in Fig. 6.3, the calculated total transfer function $h = h_{\text{prop}} * h_{\text{det}}$ excellently reproduces the structure of the measured h, in both the time (Fig. 6.3a) and frequency domain (Fig. 6.3b). Such good agreement indicates the alignment of our setup is quite close to the idealized situation underlying our model. Therefore, we use the peak value ($2.5 \cdot 10^5 \text{mV}^{-1}$) of the calculated response (Fig. 6.3a) to get the global amplitude of our measured transfer functions.

To identify the origin of prominent temporal and spectral features of h, we separately consider its components h_{prop} and h_{det}. The spectral amplitude of h_{prop} exhibits high-pass behavior (Fig. 6.4a) which is a result of the imaging of the THz near-field onto the detector. For THz wavelengths smaller than the diameter of the emitting area ($\sim$ 50 µm, corresponding to a frequency of $\sim$ 15 THz), the THz focus is diffraction-limited. Therefore, its diameter increases with the THz wavelength, and the field amplitude in the focus approximately scales with the THz frequency ω. Further amplitude losses at long THz wavelengths are due to beam clipping at the circular apertures of the parabolic mirrors. Ultimately, at $\omega = 0$, h vanishes because DC electric fields cannot propagate into the far field. Interestingly, our calculations also reveal that the longitudinal position of the THz detection focus becomes strongly frequency-dependent if the source is not positioned in the pump focus (Appendix 6.C).

The detector response h_{det} of a 250 µm thick GaP(110) crystal in conjunction with a sampling pulse (duration 20 fs, center wavelength 790 nm) is shown in Fig. 6.4b. The low-pass behavior is due to the decreasing coherence length of the detection process with increasing frequency and due to the time resolution that is limited by the duration of the gate pulse [Kam07]. Spectral features in the range from 8 to 15 THz are related with the Reststrahlen band of GaP. The dip at 8 THz arises because electronic and Raman contributions to the electrooptic response of GaP cancel at this frequency [Fau66]. Remarkably, in the modeled total transfer function (see Fig. 6.3b), the low-pass behavior of h_{det} is to a large extent compensated by the high-pass characteristics of h_{prop}, resulting in a useful bandwidth as large as 40 THz.

In the time domain, $h(t)$ can be understood as the signal that is measured for a (fictitious) δ-like THz pulse. The dominant peak at $t = 0$ (Fig. 6.3a) shows that a large part of this δ-like input survives in the electrooptic signal. Oscillatory components at $t > 0$ are related to sharp spectral features of the Reststrahlen band (Fig. 6.3b). The slow signal at $t < 0$ does not violate causality but rather reflects the fact that part of the THz pulse propagates more slowly in the electrooptic detector crystal than the optical probe does. Therefore, even when the probe arrives after the THz pulse ($t < 0$), it may catch up with the trailing part of the THz field and lead to a nonvanishing electrooptic signal.

6.6 Field extraction and robustness

We now use the measured $h(t)$ to extract the THz near-field generated by the sample emitter by numerically solving Eq. (6.1) for $E(t)$ in the time domain. The blue curve in Fig. 6.5a shows the electrooptic $S(t)$ obtained with the GaP detector, and Fig. 6.5b displays the resulting THz near-field $E(t)$. The field exhibits a very sharp rise and subsequently changes sign on a time scale of 100 fs.

Note that the setup configuration is subject to inevitable modifications from day to day, for example in terms of direction and divergence of the pump beam, which may have a strong impact on the propagation of the induced THz beam. Therefore, it is important to test the robustness of our method. For this purpose, we apply three kinds of changes to our experiment. (i) We put an additional aperture (diameter of 1 cm) in the collimated THz beam. (ii) We move the detection crystal out of the THz focus along the optical axis by 1 mm. (iii) We substitute the GaP detection material by ZnTe.

As seen in Fig. 6.5a, the resulting signal waveforms $S(t)$ strongly differ from each other. While modification (i) is accompanied by significant high-pass filtering, changes (ii) and (iii) rather result in low-pass filtering. After measuring the transfer function of each modified setup, we extract the THz near-fields $E(t)$ shown in Fig. 6.5b. Note that the resulting field traces excellently agree with one another, in terms of both shape and amplitude, despite the drastic modifications we applied to the setup. Therefore, the results of Fig. 6.5 demonstrate that our method for extracting the THz near-field is robust and reliable.

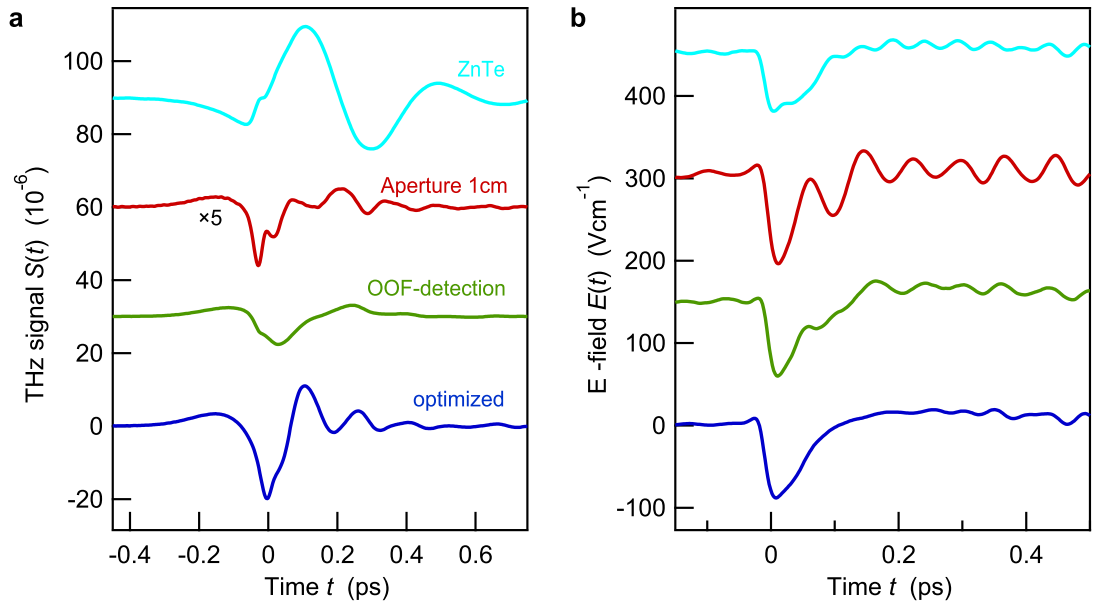

Figure 6.5: Robustness of field extraction. **a**, Electrooptic signals S from our test sample for three distinct setup conditions (see text). **b**, THz near-fields E extracted from the signals of panel **a**.

6.7 Discussion

Despite the robustness of our extraction procedure, one has to acknowledge that the degree to which $E(t)$ is faithfully retrieved relies critically on how well $E_{\mathrm{ref}}(t)$ is known. Two observations strongly indicate that our calculations of the reference field are sufficiently accurate. First, we obtain almost identical sample fields $E(t)$ for two different reference emitters, GaP and ZnTe. Second, the extracted field $E(t)$ fulfills the causality condition and rises nearly step-like with a time constant comparable to the duration of the pump pulse. Deviations of $E_{\mathrm{ref}}(t)$ from the true reference near-field would easily lead to violations nd distortions of the causal and sharp step-like shape of $E(t)$.

We emphasize that the method presented here is significantly more reliable than methods based on modeling of the transfer function [Kam13a, CÔ3, Fau04]. The reason is that calculation of the reference field E_{ref} requires a less complex model and is based on only few well-known and easily accessible parameters.

Figure 6.2 indicates that GaP is a slightly more preferable reference emitter than ZnTe. The GaP emitter provides gapless emission up to 8 THz, thereby avoiding long-lived response components arising from spectrally sharp features. Problems due to reference pulse echoes may be mitigated by using either thicker or, even better, much thinner reference emitters in which the multiple echoes merge into one pulse. Here, the recent development of THz emitters made of spintronic metals may open up a promising route as these THz sources are extremely thin and provide gapless and efficient emission from 0.5 to 30 THz [Sei16].

6.8 Conclusion

To summarize, we have shown that measurement of the transfer function h of a THz emission spectrometer is straightforward by using transparent and broadband GaP and ZnTe crystals as reference emitters. Once h is known, the THz near-field accompanied by an ultrafast photocurrent in a sample of interest can be determined robustly and reliably. Crucial ingredients of our approach are suitable reference emitters as well as performing the numerical deconvolution in the time rather than the frequency domain.

This work may help push ultrafast spectroscopy to a level that routinely permits measurements of charge transport on the timescale of elementary interaction processes. For example, we have recently used this method to reveal a first direct time-domain fingerprint of a surface shift current in a topological insulator on a 10 fs time scale [Bra16]. Since our method is applicable to all polarization components of the THz field, it provides access to ultrafast photocurrents flowing both parallelly and perpendicularly to the sample surface.

Appendix Chapter 6

6.A Reference-field calculation

The THz near-field $\mathbf{E}_{\mathrm{ref}}$ generated by the GaP and ZnTe reference emitters can be calculated within the dipole approximation following the theory of Ref. [Vug12]. Note our samples are homogeneous media and, therefore, we consider only propagation along the z-axis of a suitable component E_{ref} of $\mathbf{E}_{\mathrm{ref}}$. We first calculate the pump field $E(\omega, z')$ at position z' and optical frequency ω inside the sample:

$$E(\omega, z') = E^{\mathrm{inc}}(\omega, z') \cdot \left(t_{12} \mathrm{e}^{\mathrm{i}kz'} + t_{12} r_{23} \mathrm{e}^{-\mathrm{i}kz'} \right) \cdot M. \tag{6.2}$$

Here, E^{inc} is the incident pump field and the terms in brackets relates to forward and backword propagating waves. $t_{ij} = 2n_i/(n_i+n_j)$ and $M(\omega) = (1-r_{21}r_{23}\mathrm{e}^{2\mathrm{i}k(\omega)L})^{-1}$ account for the glas-sample transmission and multiple reflections inside the sample, associated with terms $r_{\mathrm{ij}} = (n_i - n_j)\,/\,(n_i + n_j)$. The indices $i = 1, 2, 3$ denote the media glas substrate, GaP (ZnTe) and air, respectively.

The pump field drives a second order nonlinear polarization $P_i^{(2)}$ (Eq. (3.2)) of which we are interested in the difference-frequency component oscillating at Ω,

$$P_i^{\mathrm{DF}}(\Omega) = 2 \sum_{jk} \int \int_{\omega_1 > \omega_2 > 0} \mathrm{d}\omega_1 \mathrm{d}\omega_2 \chi_{ijk}^{(2)}(\Omega; \omega_1, -\omega_2) E_j(\omega_1) E_k^*(\omega_2). \tag{6.3}$$

The magnitude of the induced polarization is given by the quadratic susceptibility [Lei99b]

$$\chi^{(2)}(\Omega) = \frac{r_e(1 + C_{\mathrm{FH}})}{1 - (\Omega^2 + i\gamma\Omega)/(\omega_{TO}^2)}. \tag{6.4}$$

Here, $C_{\mathrm{FH}} = r_i/r_e$ is the Faust-Henry coefficient that represents the ratio between the ionic and the electronic part of the electro-optic effect at $\omega = 0$ and $r_e = \frac{1}{2} n_{\mathrm{gr}}^4 r_{41}/(1 + C_{\mathrm{FH}})$ [Ber89] is the pure electronic contribution. All material constants are given in Table 6.1.

The induced polarizations emit THz radiation. We obtain the THz near-field E_{ref} by

Table 6.1: Material constants used in the calculation of THz emission and detection with ZnTe and GaP crystals. Data optimized to our crystals based on parameters given in Refs. [Lei99b, Die12, Ber89, Gal99, Xue97]. The transverse and longitudinal optical phonon frequencies, the lattice damping, the dielectric coefficient, the Faust Henry coefficient, the electrooptic coefficient and the group refractive index at a wavelength of 790 nm are denoted by ω_{TO}, ω_{LO}, γ, ε_∞, C_{FH}, r_{41}, n_{gr}.

	$\omega_{\mathrm{TO}}/2\pi$ (THz)	$\omega_{\mathrm{LO}}/2\pi$ (THz)	γ (THz)	ε_∞	C_{FH}	$r_{41}(10^{-12}\ \frac{\mathrm{m}}{\mathrm{V}})$	n_{gr}
GaP	11.01	12.082	0.129	9.65	-0.46	0.88	3.2
ZnTe	5.19	6.18	0.025	7.45	-0.07	4.45	2.9

z'-integration of all contributions $P_i^{\mathrm{DF}}(z', \Omega)$

$$\tilde{E}_{\mathrm{ref}}(L, \Omega) = -4\pi \frac{\Omega^2}{c^2} \int_0^L \mathrm{d}z' P_i^{\mathrm{DF}}(z', \Omega) G_{z'}(L, \Omega) C_{\mathrm{Ph}}. \tag{6.5}$$

$G_{z'}$ is the Green's function, which relates P_i^{DF} at z' to the THz near-field E_{ref} directly after the crystal excite face at $z = L$,

$$G(L) = \frac{\exp[i\frac{\Omega}{c} n(L - z')]}{2i\frac{\Omega}{c} n} \cdot t_{23}. \tag{6.6}$$

Here, t_{23} accounts for the crystal-air transmission. Multiple reflections are neglected in the short time window ($\sim$ 1ps) considered here. The refractive index n at THz frequencies can be parameterized by only a few constants [Lei99b],

$$n(\omega) = \sqrt{\left[1 + \frac{\omega_{\mathrm{LO}}^2 - \omega_{\mathrm{TO}}^2}{\omega_{\mathrm{TO}}^2 - \Omega_2 - i\gamma\Omega}\right] \cdot \varepsilon_\infty}. \tag{6.7}$$

The transverse ω_{TO} and longitudinal ω_{LO} optical phonon frequencies and the damping γ are given in Table 6.1 for GaP and ZnTe.

6.B Time-domain deconvolution

Eq. (6.1) states that knowledge of the signal $S_{\mathrm{ref}}(t)$ and field $E_{\mathrm{ref}}(t)$ allows to extract the transfer function h by an inversion. Such procedure requires the deconvolution of $(h * E_{\mathrm{ref}})$, which is usually done in the frequency domain. However, the essential Fourier transform requires well defined time domain data on a sufficiently long time window with an amplitude vanishing within this window. Unfortunately, the time window over which S is measured is limited. Thus, a finite measurement window has to be included in Eq. (6.1) by multiplication with a rectangular window function a,

$$S = a \cdot (h * E). \tag{6.8}$$

Problems arise when there is non-zero signal at the edges of the time window. They cause discontinuities (jumps) abd, consequently, artificial frequency components. More precisely, in the Frequency domain we get

$$\frac{\tilde{S}}{\tilde{E}} = \frac{a * (\tilde{h} \cdot \tilde{E})}{\tilde{E}} \tag{6.9}$$

Eq. (6.9) shows that $\tilde{E}$ does in general not cancel in the ratio $\tilde{S}/\tilde{E}$. Therefore, assuming $\tilde{S}/\tilde{E} = \tilde{h}$ is not generally valid and can lead to artifacts. To minimize artificial signals, an appropriate choice of the window function [Nay07] as usually done in FTIR measurements can smoothly force S to zero when t approaches the edges of the measured time window. This affects signal shape (especially broadens resonance features) and shrinks the effective measurement window.

Since this problem arises from the Fourier transformation, our solution is to deconvolve Eq. (6.8) in the time domain. We implement this by writing Eq. (6.9) as a matrix equation [Han02] which needs to be inverted. More precisely, we first rewrite the convolution in terms of a discrete mesh (t'_j, t_i)

$$S(t_i) = \sum_{j=1}^{n} E(t'_j, t_i) h(t'_j,). \tag{6.10}$$

The elements $E(t'_j, t_i)$ can be interpreted as elements m_{ij} of the $m \times n$ matrix M where m is larger than n to obtain an overdetermined matrix equation. The set of Equations (6.10) can be solved by inversion of

$$S = M \cdot h \tag{6.11}$$

with respect to h. We choose m and n such to obtain a stable solution.

6.C Modeling the transfer function

In Fig. 6.3 we show the calculated spectrometer transfer function, that contains (i) the propagation from the sample excite face to the detector (Fig. 6.4a) and (ii) the detector response (Fig. 6.4b).

(i) When the THz pulse propagates through any focusing optics, its spatial properties are modified. Such propagation is often accounted for in the framework of Gaussian-beam optics using the geometrical paramters of our spectrometer (distances, focal lengths and apertures of the parabolic mirrors) [Kuž99]. We note that that small changes of the beam propagation can significantly modify the spectrometer response function. For example, to reduce the pulse intensity but simultaneously increase the emitting area it might be of interest to move the THz emitter away from the focus position of the spectrometer. Such modification of the spectrometer response function has severe consequences on the beam focus itself as can be seen by considering the complex beam parameter q defined by the radius of curvature R of the phase front and the beam waist w [Yar89]

$$\frac{1}{q} = \frac{1}{R} + \frac{2\mathrm{i}}{kw^2}. \tag{6.12}$$

At the focus, $1/q_0 = \mathrm{i}/kw_0^2$ is purely imaginary, and since $R = R_0 = \infty$ for all frequencies, the emitted radiation has a common focus independent of the frequency. But, when we generate THz radiation at $z_1 \neq z_0$ the corresponding beam parameter is $q(z_1) = q(z_0) + z_1 - z_0$. Importantly, this implies that the distance between the field generation and the beam tail $(z_1 - z_0)$ becomes frequency dependent

$$z_1 - z_0 = \mathrm{Re}\ q(z_1) = \frac{R}{1 + \left(\frac{2R}{kw^2}\right)}. \tag{6.13}$$

In consequence, THz generation in a divergent beam induces a detection focus that depends on k, which sets a bandpass dependent on the detector position. The sensitivity to this

effect grows with decreasing Rayleigh length ($\propto$ beam waist^{2}and ω) and therefore it mainly appears as lowpass filter (Fig. 6.5). The detector z position used in our model to calculate h is adjusted within our alignment error of $\sim$ 100µm to match the frequency role off observed in our measurement (Fig. 6.3).

(ii) The detector response is calculated as published in references [Kam07] with the optical constants given in Table 6.1.

7 Ultrafast photocurrents at the surface of the three-dimensional topological insulator Bi_2Se_3

In this chapter, we excite and measure photocurrents in the model topological insulator Bi_2Se_3 *with a time resolution as high as 20 fs by sampling the concomitantly emitted broadband THz electromagnetic field from 0.3 to 40 THz. We use the THz-signal to extract the underlying source currents and find surface and bulk contributions. Strikingly, the surface current response is dominated by an ultrafast charge transfer along the Se-Bi bonds. In contrast, photon-helicity-dependent photocurrents are found to have orders of magnitude smaller magnitude than expected from generation scenarios based on asymmetric depopulation of the Dirac cone.*

This chapter has been published in Nature Communications 7, (2016) 13259, http://dx.doi.org/10.1038/ncomms13259.

7.1 Motivation

Many efforts in current solid-state research aim at pushing the speed of electronic devices from the gigahertz to the terahertz (1 THz = 10^{12} Hz) range [dA11] and at extending their functionalities by the spin of the electron.[Sta14] In these respects, three-dimensional topological insulators (TIs) are a highly promising material class. While having an insulating bulk, their surface is metallic due to a band inversion that is topologically protected against external perturbations. Bi_2Se_3 is a model TI [Zha09] as its surface features a single pair of linear Dirac-type electronic energy bands [Qi11] with spin-velocity locking and forbidden 180° backscattering.[Moo10] These properties are ideal prerequisites to induce large spin polarizations by means of surface currents.

Part of this considerable potential was demonstrated by recent works which reported the exciting possibility of launching TI surface currents by simply illuminating the sample with light.[McI12b, Dua14, Olb14, Luo13, Zhu15, Tu15, Bas15, Kas15] The direction of the photocurrent could be controlled through the polarization state of the incident light beam. The assignment to a surface process was supported by picosecond time-of-flight measurements [Kas15] showing that the ballistic photoinduced carriers were propagating at a speed comparable to the band velocity of the Dirac states. There is, however, still an intense debate about mechanisms leading to TI surface photocurrents. Scenarios based on asymmetric depopulation of the Dirac cone,[McI12b] transitions into other, higher-lying cones [Kas15] and asymmetric scattering of electrons [Olb14] have been proposed. To directly resolve the generation of TI surface photocurrents, we need to boost the time resolution of the experiment from so far $\sim$ 250 fs and longer[Luo13, Zhu15, Tu15, Bas15, Kas15] to the scale of elementary scattering events, which can be shorter than 10 fs.

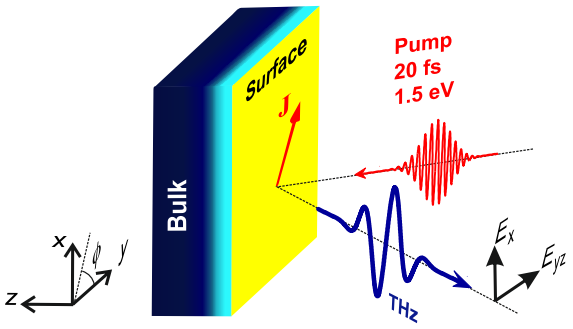

Figure 7.1: Schematic of the ultrafast photocurrent amperemeter. A Bi_2Se_3 crystal is excited by a femtosecond laser pulse, resulting in a photocurrent burst and, consequently, emission of a THz electromagnetic pulse. Measurement of the transient THz electric field components $E_x(t)$ and $E_{yz}(t)$ by electrooptic sampling provides access to the sheet current $\mathbf{J}(t)$ flowing inside the sample.

Here, we use ultrabroadband THz emission spectroscopy [Lei99a, Lei00, Kam13a] from 0.3 to 40 THz to probe the ultrafast evolution of photocurrents in the Ca-doped model TI Bi_2Se_3 with unprecedented time resolution. Based on an analysis of their temporal structure and symmetry, we identify distinct current sources. First, a slow drift current of photoinduced bulk charge carriers along the TI surface field is found. Second, we observe that currents depending on the pump helicity are orders of magnitude smaller than expected from the photocurrent generation scenario based on asymmetric depopulation of the Dirac cone [McI12b]. This remarkable result suggests a strong mutual cancelation of the contributions of the various optical transitions, much reduced matrix elements for surface-to-bulk transitions and/or relatively small pump-induced changes in the electron band velocity. Finally, for the first time, we observe a new type of photocurrent, a surface shift current, which originates from an instantaneous displacement of electron density along the Se-Bi bond. This charge transfer is localized in a surface region of $\sim$ 2 nm thickness, the natural confinement scale of topological surface states. Its relaxation time of 22 fs provides the time scale on which the optically excited surface carriers relax to an isotropic distribution. In terms of applications, the instantaneous electric field generated by the shift current could be employed to drive highly spin-polarized THz electric currents at the TI surface along an easily tunable direction.

7.2 Experimental details

7.2.1 Ultrafast photocurrent amperemeter

A schematic of our experiment is depicted in Fig. 7.1. A femtosecond laser pulse is incident on the specimen and launches a transient charge current density $\mathbf{j}(z,t)$. This photocurrent, in turn, emits an electromagnetic pulse with transient electric field $\mathbf{E}(t)$, in particular covering frequencies up to the THz range, as expected from the inverse duration of the femtosecond stimulus. The measurement of $\mathbf{E}(t)$ over a large bandwidth (0.3 to 40 THz)

permits extraction of the sheet current density

$$\mathbf{J}(t) = \int \mathrm{d}z\, \mathbf{j}(z,t) \tag{7.1}$$

with ultrafast time resolution.

As detailed in Appendix 7.B and 7.C, this approach allows us to separately determine the current component J_x directed along the x axis and the component J_{yz}, which is a linear combination of the roughly equally weighted Cartesian components J_y and J_z (see Fig. 7.1 and Appendix 7.C). By virtue of a generalized Ohm's law, the currents J_x and J_{yz} are, respectively, connected to the s-polarized electric-field component E_x and the perpendicular, p-polarized component E_{yz} directly behind the sample (Fig. 7.1). The THz near-fields E_x and E_{yz} are obtained by measuring the THz far-field using electrooptic sampling, resulting in the electrooptic signals S_x and S_{yz}, respectively (see Appendix 7.B). THz waveforms are acquired at the shot-noise limit of the setup and for various settings of the pump polarization and sample azimuth ϕ (Fig. 7.2a).

7.2.2 Ultrafast THz emission setup

To drive ultrafast photocurrents, laser pulses (duration of ≈ 20 fs, center wavelength of 790 nm, energy 2.5 nJ) from a Ti:sapphire oscillator (repetition rate 80 MHz) are focused onto the sample (beam diameter of 200 µm full-width at half intensity maximum) under 45° angle of incidence, resulting in an average intensity $< 0.3\,\mathrm{kW\,cm^{-2}}$, well below sample damage threshold. The specularly emitted THz pulse is focused onto an electrooptic crystal in which the THz electric field is detected by broadband electrooptic sampling [Fer02a]. We use a (110)-oriented GaP crystal (thickness of 250 µm) owing to its relatively flat and broadband response function [Kam13a]. The only exception are the measurements of the two-dimensional data set $S(t,\phi)$ (Fig. 7.4 and Fig. 7.8) which are sped up by using a (110)-oriented ZnTe crystal (thickness of 300 µm) which exhibits an enhanced detector response at the expense of reduced bandwidth. To calibrate the direction of the measured photocurrent, we use a photoconductive switch as a reference emitter in which the direction of the initial photocurrent burst is along the direction of the external bias field.

Optical wave plates are used to set the polarization state of the pump pulse to linear (with arbitrary rotation angle) or circular. Here, it is essential to avoid any optically birefringent elements (including mirrors) between wave plate and sample. A THz wire-grid polarizer (field extinction ratio of 10^{-2}) allows us to measure the x- and yz-components E_x and E_{yz} of the THz electric field separately, thereby disentangling current components J_x and J_{yz}, the latter being a linear combination of J_y and J_z [see Fig. 7.1 and Eq. (7.8)]. To ensure the electrooptic THz detector has an identical response to E_x and E_{yz}, a wire-grid polarizer with 45° orientation is placed in front of it. Variation of the sample azimuth ϕ is performed by attaching the sample to a computer-controlled rotation stage.

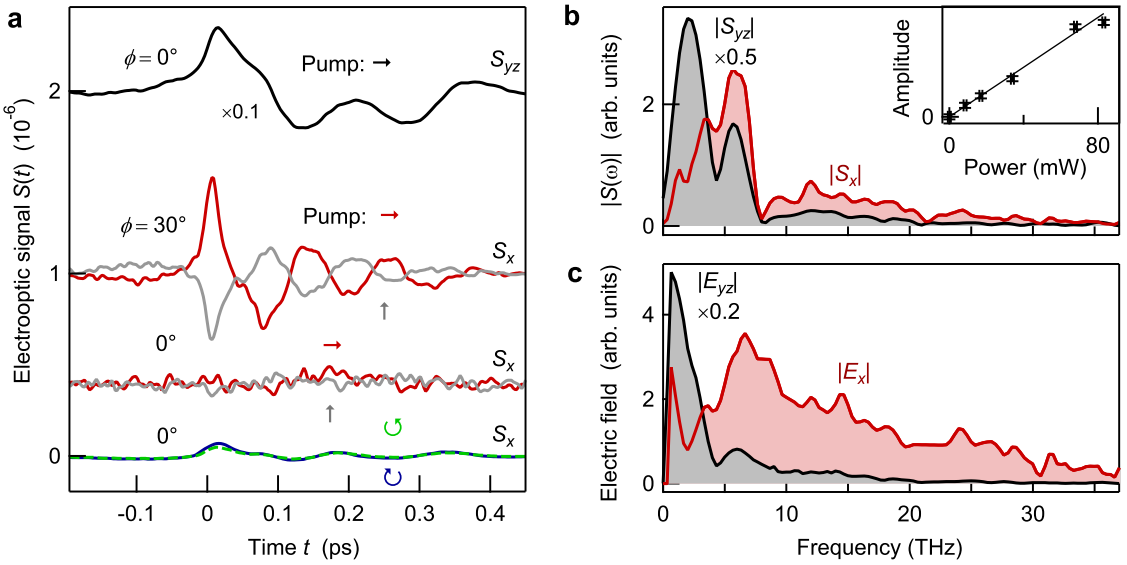

Figure 7.2: THz emission from Bi_2Se_3. **a**, Typical x- and yz-polarized THz electrooptic signals S_x and S_{yz} measured for various settings of pump polarization and sample azimuth ϕ. Signals are offset for clarity. **b**, Amplitude spectra of the THz signal and **c**, THz electric field directly behind the sample as extracted from **a**.

7.2.3 Sample properties

We study a freshly cleaved, n-type, Ca-doped Bi_2Se_3 single crystal in ambient air (see Appendix 7.A). While dipolar photocurrents in the inversion-symmetric crystal bulk (space group D^5_{3d}) cancel, optical excitation can in principle launch a current at the surface (space group C_{3v}) [Liu10]. The surface region can be thought of as being comprised of the air-crystal interface with locally relaxed lattice structure which overlaps with the Dirac surface states (thickness of ~ 2 nm) [Zha10, Roy14], followed by a space-charge region with bent bulk bands (thickness of tens of nanometers) [McI12a, Par13]. As the sample thickness (> 300 µm) is much larger than the pump penetration depth (24 nm) [McI12a], the front but not the back surface of the sample is probed. Further details on sample properties and characterization can be found in Appendix 7.A.

In what follows, we will show that our broadband current measurements allow us to discriminate different types of photocurrents and their generation in the various surface regions. This goal is achieved by first identifying two dominating components in the THz emission signal using symmetry analysis. Finally, based on their temporal structure and symmetry, the two underlying photocurrent components are assigned to microscopic generation scenarios.

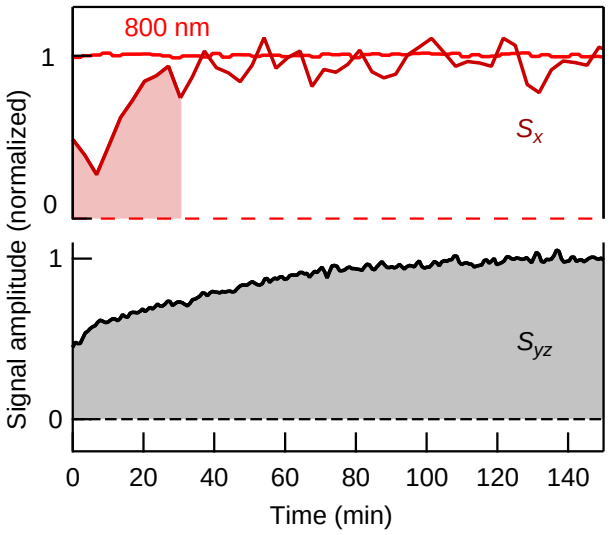

Figure 7.3: Long-term signal changes. Evolution of the amplitudes of THz signals S_x and S_{yz} and the reflectance of the 790 nm pump beam following cleaving of the sample. The constant 790 nm signal indicates that no sample damage occurs.

7.3 Results

7.3.1 Raw data

Typical THz electrooptic signal waveforms $S(t)$ obtained from our Bi_2Se_3 sample are shown in Fig. 7.2a. The THz waveforms depend sensitively on the setting of the THz polarization (x vs yz), the pump polarization and the sample azimuthal angle ϕ. The signal amplitude grows linearly with increasing pump power, without any indication of saturation (inset of Fig. 7.2b). This behavior implies that the number of excited carriers is proportional to the incident photon number.

As detailed in the following, we make the striking observation that the x- and yz-polarized components of the emitted THz field (and, thus, J_x and J_{yz}) behave very differently in terms of their magnitude (Fig. 7.2a), temporal shape (Fig. 7.2a), their behavior after sample cleavage (Fig. 7.3) and their dependence on the sample azimuth ϕ (Fig. 7.4b). First, as seen in Fig. 7.2a, S_{yz} exhibits much larger amplitude than S_x but evolves significantly more slowly. Accordingly, the amplitude spectrum of S_x exhibits a larger bandwidth than S_{yz} (Fig. 7.2b). This trend becomes even clearer when we apply an inversion procedure to these data to extract the transient THz fields E_x and E_{yz} directly behind the sample (see Appendix 7.B). The resulting spectral amplitudes are displayed in Fig. 7.2c as a function of angular frequency ω and show that $|E_x(\omega)|$ is much broader than $|E_{yz}(\omega)|$, indicating much faster temporal dynamics. The spectrum exhibits features such as the dips of $|E_x(\omega)|$ at $\omega/2\pi = 2$ THz and 4 THz whose origin becomes clear further below.

Second, to investigate the impact of surface modification on S_x and S_{yz}, we freshly cleave the sample and subsequently acquire THz signals continuously over > 2 h with the sample exposed to air. While the shape of the THz waveforms does not undergo measurable modi-

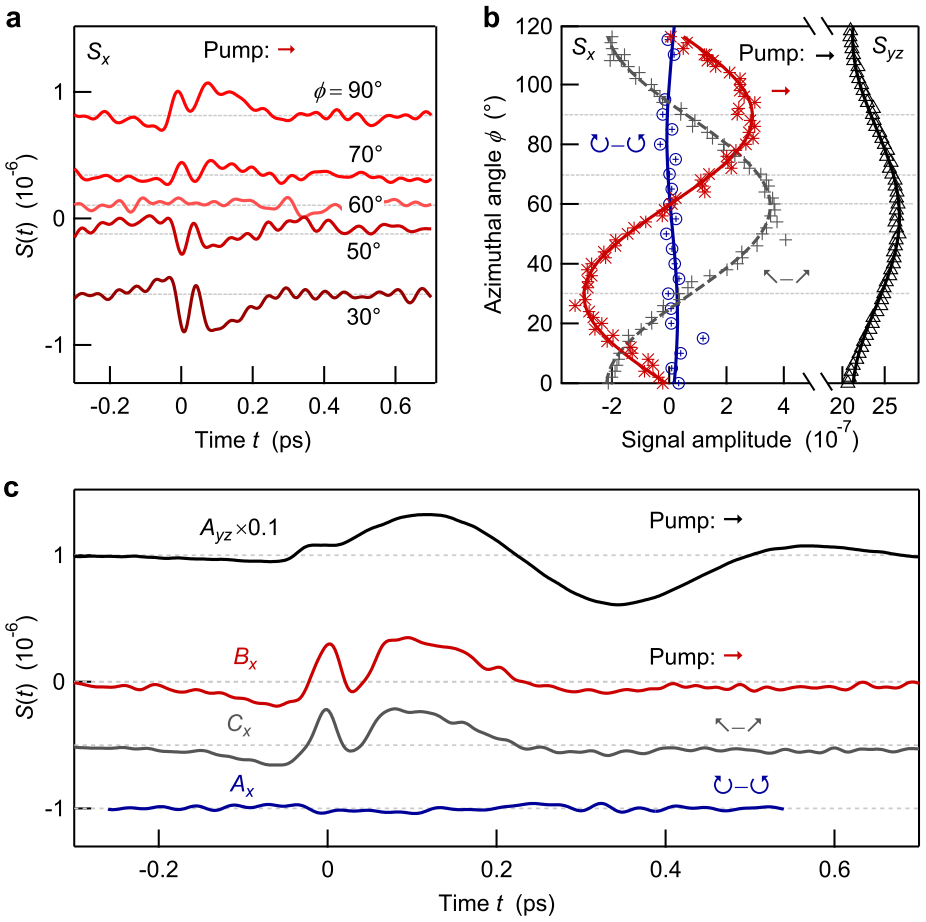

Figure 7.4: Azimuth dependence and dominant components of THz signal S_x. **a**, THz signal waveforms at various sample azimuth angles ϕ and for fixed pump polarization. **b**, Extracted THz amplitude vs ϕ for various pump-polarization settings ($\rightarrow$ and differential signals $\nwarrow - \nearrow$ and $\circlearrowright - \circlearrowleft$). While both S_x and S_{yz} exhibit a 3ϕ-type-dependent component of comparable magnitude, S_{yz} has a much larger and dominant component independent of ϕ. **c**, Dominant temporal components of signal sets $S_{yz}(t, \phi)$ and $S_x(t, \phi)$ for various pump polarizations, extracted by using Eq. (7.2) (see Appendix 7.E).

fications, their global amplitude increases by a factor of ≈ 2 in the course of time (Fig. 7.3). Note this rise proceeds within 30 min for S_x but significantly slower (within 100 min) for S_{yz}. We will later use this different evolution speed of S_x and S_{yz} to draw conclusions concerning the degree of surface localization of the currents J_x and J_{yz}. In contrast to S_x and S_{yz}, measurable changes of the sample reflectance at a wavelength of 800 nm are not observed, thereby ruling optical degradation of our sample out. In addition, we did not observe temporal changes in the signal symmetry which is discussed in the next section.

7.3.2 Signal symmetries

In addition to their different amplitude and temporal structure, S_x and S_{yz} also depend very differently on the sample azimuth ϕ. To quantify this behavior, we measure waveforms $S_x(t, \phi)$ and $S_{yz}(t, \phi)$ for an extended set of ϕ-values, example traces of which are shown

in Fig. 7.4a. To reliably extract an average signal amplitude for each ϕ, we project the time-domain signal on a suitable reference waveform (see Appendix 7.D). The resulting signal amplitude as a function of ϕ is displayed in Fig. 7.4b. While both S_x and S_{yz} exhibit a 120°-periodic component of comparable magnitude, S_{yz} has a much larger and dominant component independent of ϕ.

The threefold rotational symmetry of the THz signals is fully consistent with the symmetry groups of sample surface and bulk as shown by a detailed analysis of the second-order conductivity tensor (see Appendix 7.F) [Zha09]. Importantly, it allows us to significantly reduce the large amount of experimental data contained in $S(t, \phi)$: for a given THz polarization (x or yz) and pump polarization, each two-dimensional set $S(t, \phi)$ can be written as a linear combination of just three basis functions (see Appendix 7.E),

$$S(t, \phi) = A(t) + B(t)\sin(3\phi) + C(t)\cos(3\phi). \tag{7.2}$$

Therefore, three basis signals $A(t)$, $B(t)$ and $C(t)$ fully characterize the entire data set $S(t, \phi)$. They are, respectively, obtained by projecting $S(t, \phi)$ onto the mutually orthogonal functions 1, $\sin(3\phi)$ and $\cos(3\phi)$ (Appendix 7.E). Extracted waves are shown in Fig. 7.4c and Fig. 7.8d for the two THz polarizations and various pump polarizations.

We begin with considering the impact of the pump helicity on the photocurrent. The bottommost curve in Fig. 7.4c represents the ϕ-independent component $A_x(t)$ of the difference of the signals taken with right-handed (↻) and left-handed (↺) circularly polarized pump light. The amplitude of this waveform is comparable to the noise floor. In other words, a helicity-dependent yet simultaneously ϕ-independent THz signal is small and below our detection threshold. This notion is consistent with time-domain raw data (blue vs green trace in Fig. 7.2a) and the absence of an offset in the ϕ-dependence (blue curve of Fig. 7.4b). An analogous behavior is observed for THz signals S_{yz} (see Fig. 7.10). We note that such small magnitude of the pump-helicity-dependent and ϕ-independent photocurrent does not contradict the previously reported observation of time-integrated currents [McI12b] as will be addressed in the Discussion section.

7.3.3 Ultrafast photocurrents

Figure 7.4c leads to another important conclusion of our symmetry analysis: regardless of the pump polarization, all signals S_x and S_{yz} are, respectively, dominated by just one fast and one slow waveform. We use these signals to extract the underlying source currents (see Appendix 7.B and 7.C) which are displayed in Fig. 7.5. After an initial onset, both J_x and J_{yz} change sign, indicating a backflow of charge. Note, however, J_x proceeds much faster than J_{yz}: the rise time from 10% to 90% of the current maximum is 16 fs and 40 fs for J_x and J_{yz}, respectively. Subsequently, J_x decays with a time constant of 22 fs, while J_{yz} decays within 700 fs.

To determine the origin of J_x and J_{yz} based on their ultrafast dynamics, we briefly review known photocurrent generation mechanisms.[Nas10, Lew14, Olb14, McI12b, Hos11, Gan03a, Sch15, Pri12] In general, optical excitation transfers electrons from initial states $|\mathrm{i}\rangle$ into final states $|\mathrm{f}\rangle$ (Fig. 7.6a), followed by relaxation processes such as scattering into

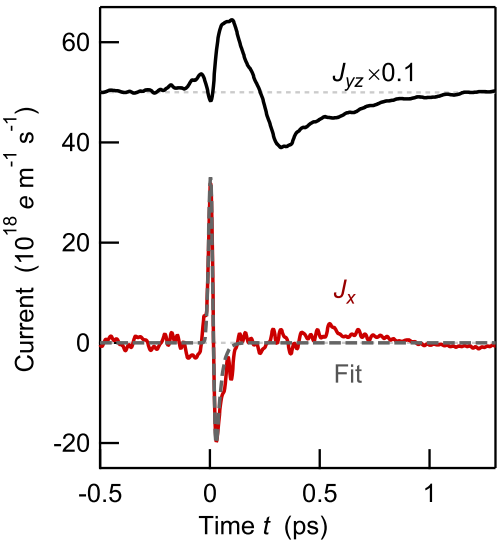

Figure 7.5: Source currents of the two dominant signal components (see Fig. 7.4). The dynamics of these currents allow us to reveal the origin of the photocurrent (see Fig. 7.6). Curves are offset for clarity.

other states, phonon emission and recombination.[Sob14] Photocurrents can arise in both regimes, that is, during the optical transition and during the subsequent relaxation. As our pump photon energy (1.57 eV) is much larger than the Bi_2Se_3 band gap, numerous vertical interband transitions are allowed [Bos15] (Fig. 7.6e) and expected to outnumber the contribution of phonon- or impurity-assisted nonvertical transitions.[Web08] In the subsequent relaxation regime, currents can arise from, for instance, scattering by a noncentrosymmetric potential,[Olb14] asymmetric recombination [Gla74] and carrier acceleration in an intrinsic surface field (drift current).[Joh02, Mal08] In all cases, inversion symmetry needs to be broken to obtain a macroscopic dipolar net current.

Drift current

As seen in Fig. 7.5, the slow current $J_{yz}(t)$ has a rise time (40 fs) significantly slower than the excitation pulse (23 fs). Therefore, it cannot arise from the initial optical transition. In fact, previous works on Bi_2Se_3 assigned the slow J_{yz} component to a carrier drift in the surface field, consistent with the strong dependence of J_{yz} on the doping level of Bi_2Se_3.[Luo13, Zhu15, Tu15] This notion is further supported by additional observations made in our experiment: first, the initial electron flow is directed toward the sample surface, along the direction of the space-charge field of our effectively n-doped sample. Second, the 40 fs rise time (Fig. 7.5) is on the order of the bulk Drude scattering time of our sample ($\sim$ 18 fs, see Appendix 7.A) that limits charge acceleration in the surface field.

Following its initial rise, J_{yz} is found to change sign. Plasma oscillation[Sha04] of the charge carriers cannot account for this feature because the short Drude scattering time ($\sim$ 18 fs, see Appendix 7.A) would strongly attenuate such dynamics in less than 100 fs, in

contrast to our observation. We consequently assign the sign change of J_{yz} to the back-flow of charge that accompanies the overall relaxation of the photoexcited system back to the equilibrium state. From photoemission studies,[Sob14] the relaxation of optically excited bulk carriers is known to occur on a time scale of 1 ps, in agreement with the relaxation time of J_{yz} (see Fig. 7.5).

Shift current

Having assigned the slow, dominant part of current J_{yz}, we now focus on the very fast, sub-100 fs dynamics of the photocurrent J_x. Concerning immediate photocurrent generation by an optical transition $|\mathrm{i}\rangle \rightarrow |\mathrm{f}\rangle$, Sipe *et al.* [Sip00, Nas10] used perturbation theory and identified three distinct mechanisms: injection currents, shift currents and optical rectification.[Nas10, Lam05] Injection currents J_{inj} arise because initial and final state of the perturbed electron have different band velocity. An example is the asymmetric band depopulation scenario [McI12b] shown in Fig. 7.6a: a circularly polarized pump excites electrons from the Dirac cone into higher-lying states with different band slope (group velocity). Therefore, for short enough excitation, J_{inj} should rise instantaneously to a magnitude that scales with the average velocity change Δv and the density N of the excited electrons. In this simplified model, the resulting current is

$$J_{\mathrm{inj}} = \sigma_{\mathrm{inj}} \Delta v \, [\Theta(t) \mathrm{e}^{-t/\tau_{\mathrm{inj}}}] * I_{\mathrm{p}} \tag{7.3}$$

where the initial sheet charge density $\sigma_{\mathrm{inj}} = eN\Delta z_{\mathrm{inj}}$ is proportional to the thickness Δz_{inj} of the emitting sheet, and $\Theta(t)$ is the unit step function. Note that relaxation processes such as electron scattering are not covered by the theory of Ref. [Nas10]. We have introduced them phenomenologically by an exponential decay with time constant τ_{inj}. Backflow of electrons is diffusive [Apo14] and ignored on the short timescales considered here. Finally, the convolution with the pump intensity envelope $I_{\mathrm{p}}(t)$ (normalized to unity) accounts for the shape of the pump pulse, resulting in a current with the typical temporal shape shown in Fig. 7.6b.

Shift currents,[Nas06] on the other hand, arise when the electron density distribution of the excited state $|\mathrm{f}\rangle$ is spatially shifted with respect to $|\mathrm{i}\rangle$ (Fig. 7.6c). For short excitation, this process leads to a step-like charge displacement $\Delta x_{\mathrm{sh}} \Theta(t)$ whose temporal derivative is proportional to the shift current J_{sh}. With arguments analogous to the injection case, we obtain

$$J_{\mathrm{sh}} = \sigma_{\mathrm{sh}} \Delta x \, \frac{\partial}{\partial t} [\Theta(t) \mathrm{e}^{-t/\tau_{\mathrm{sh}}}] * I_{\mathrm{p}}, \tag{7.4}$$

with $\sigma_{\mathrm{sh}} = eN\Delta z_{\mathrm{sh}}$. This model implies J_{sh} initially follows the profile of $I_{\mathrm{p}}(t)$ and becomes bipolar if the relaxation time τ_{sh} is comparable to or longer than the pump duration (Fig. 7.6d).

Finally, optical rectification can be understood as a transient, nonresonantly driven charge displacement that follows the intensity envelope of the pump pulse. It arises from all transitions between the initial and final states whose energy difference is different from the incident photon energy of 1.57 eV.[Côt02] To evaluate the relative importance of optical rectification in our experiment, we compared the emitted THz amplitude of our TI sample

to that of a pump-transparent ZnTe(110) crystal which is known for relatively strong optical rectification at the pump photon energy used here.[Fer02a] We find that, normalized to the thickness of the emitting crystal, the THz signal S_x from the TI sample is about two orders of magnitude larger than that from ZnTe. Therefore, optical rectification in Bi_2Se_3 is expected to make a negligible contribution, and we are left with considering ultrafast injection and shift currents.

Note the characteristic shape of J_{inj} and J_{sh} is very distinct: unipolar (Fig. 7.6b) vs bipolar asymmetric (Fig. 7.6d). Having understood how the temporal shape of a current is intrinsically linked to its origin, we now look for such fingerprints in our data (Fig. 7.5). Indeed, we find that the measured photocurrent J_x (Fig. 7.5) has bipolar asymmetric temporal shape: the signature of a shift current. In addition, fitting Eq. (7.4) to J_x yields excellent agreement (Fig. 7.5) for a pump duration of 23 fs, $\tau_{\mathrm{sh}} = 22$ fs and $\Delta x_{\mathrm{sh}} \Delta z_{\mathrm{sh}} \approx 36$ Å^2. In this procedure, we use the excitation density ($N = 6.9 \times 10^{24}$ m^{-3}) as inferred from the absorbed pump fluence (4 µJ cm^{-2}), the pump photon energy (1.57 eV) and the pump penetration depth (24 nm at 1/e intensity) [McI12a]. The amplitude spectrum of the calculated J_{sh} peaks at 6 THz (not shown), consistent with the peak position of the measured E_x amplitude spectrum (Fig. 7.2c).

One could argue that the current J_x is not a pure shift current (Fig. 7.6d) but still contains a component arising from a rapidly decaying injection current (Fig. 7.6b). We can exclude this possibility based on a symmetry analysis and photocurrent theory work [Nas10]. For example, for linear pump polarization at 45° with respect to the plane of incidence, the resulting current J_x is solely related to the second-order conductivity tensor element σ_{xxy} (see Appendix 7.F and 7.G). As dictated by symmetry, this element equals σ_{xyx} and becomes, therefore, real-valued when the photocurrent frequency approaches $\omega = 0$. From the microscopic analysis of Sipe and Nastos [Nas10], it follows that this tensor element and the related photocurrent J_x are not due to an injection current, provided that photocurrent frequencies ω higher than the current relaxation rate are considered (see Appendix 7.F).

7.3.4 Surface localization

Our photocurrent measurements and analysis directly reveal an ultrafast shift current and a drift current in the time domain. It is so far, however, unclear to which extent these currents are localized at the surface. Since the photocurrent observed here is a quadratic nonlinear-optical effect (see inset of Fig. 7.2b), it only flows in regions where inversion symmetry is locally broken [She84]. In our sample, this breaking arises from two perturbations of the inversion-symmetric bulk: (i) the surface, which extends over the first 1 to 2 quintuple layers ($\sim$ 1 to 2 nm) as indicated by the thickness of surface states [Zha10] and the depth of surface lattice relaxation [Roy14], and (ii) the space-charge field $\mathbf{E}_{\mathrm{SC}}$, which points along the surface normal and extends $\sim$ 15 nm into the depth of the sample, as implied by an estimate analogous to Ref. [McI12a].

Since the slow component of J_{yz} is a drift current of photoexcited carriers in the space-charge field [Luo13, Zhu15, Tu15], it is also localized in a depth of $\sim$ 15 nm. In addition, its amplitude changes during sample aging must arise from gradual modifications of $\mathbf{E}_{\mathrm{SC}}$

(Fig. 7.3). If J_x were also dominated by $\mathbf{E}_{\mathrm{SC}}$, its amplitude should evolve analogously to J_{yz} following sample cleaving. In contrast, we observe that J_x evolves about 5 times faster than J_{yz} (see Fig. 7.3) such that J_x cannot arise from perturbation (ii) but rather from the remaining perturbation (i). Therefore, the shift current is localized in the first 1 to 2 quintuple layers of the Bi_2Se_3 surface. The resulting Δz_{sh} of less than 2 nm and the above extracted estimate for $\Delta x_{\mathrm{sh}}\Delta z_{\mathrm{sh}}$ imply the shift distance Δx_{sh} is on the order of 1 Å.

We note that the THz emission spectra exhibit sharp features at 2 and 4 THz (Figs. 7.2b and 7.2c) which coincide with the frequencies of long-wavelength bulk phonon modes at 1.9, 2.1 and 4 THz (Ref. [Mad98b]). While the 1.9 THz mode is infrared-active and can thus absorb pump-generated THz radiation, the 4 THz mode is exclusively Raman active in the inversion-symmetric bulk. Therefore, the presence of the 4 THz feature in the emission spectrum suggests this mode is infrared-activated in the TI surface region where inversion symmetry is locally broken.[Gne11] This effect further underlines the surface sensitivity of THz emission spectroscopy.

7.4 Discussion

To summarize, we have shown that our ultrabroadband THz emission data are fully consistent with the notion that (i) the photocurrent J_x arises from an instantaneous photoinduced shift of charge density by ~ 1 Å in a ~ 2 nm thick surface region of Bi_2Se_3. The displacement relaxes on a very fast time scale of 22 fs. The much slower current J_{yz} is dominated by a drift current of optically excited carriers in the surface field. (ii) A helicity-dependent and simultaneously azimuth-independent photocurrent is smaller than our detection threshold of $10^{18}\ e\,\mathrm{m}^{-1}\,\mathrm{s}^{-1}$. This assertion is also valid for other injection-type transport scenarios such as photon-drag currents.[Pla16] It is instructive to discuss these observations and compare them to previous works.

7.4.1 The source of the shift current

Finding (i) represents the first observation of a surface shift current, which was predicted by Cabellos *et al.* very recently [Cab11]. We note that we also observe signatures of ultrafast surface shift currents in other TI samples, including thin films [Kru11] of Bi_2Se_3 and Bi_2Te_3 (not shown). We emphasize that revealing the time-domain fingerprint of shift currents relies on the 20 fs time resolution of our experiment. Longer pump pulses can easily obscure this signature, even in materials with broken bulk inversion symmetry [Lam05]. The surface shift current is probably the source of the linear photogalvanic surface currents that have been reported previously [McI12b], but not assigned.

Our results show that the displacement of bound charges occurs in a sheet with thickness $\Delta z_{\mathrm{sh}} \sim 2$ nm, which is the thickness of the layer where the Dirac states are expected to dominate charge transport [Zha10]. This notion is consistent with reports [Roy14] showing that only the first quintuple layer exhibits inversion asymmetry on the order of 10%. The shift distance $\Delta x_{\mathrm{sh}} \sim 1$ Å compares well to reported charge shifts on the order of the bond length (~ 3 Å) in noncentrosymmetric semiconductors [Nas06].

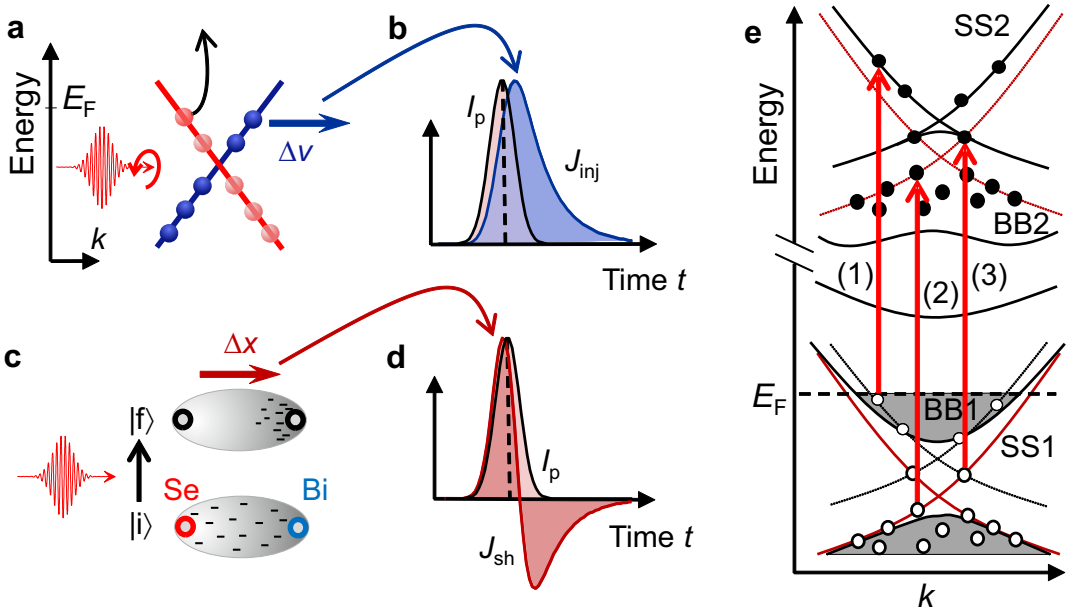

Figure 7.6: Photocurrent assignment. **a**, Example of an injection-type photocurrent. The pump pulse promotes electrons from the Dirac cone into other bands, thereby changing the electron band velocity. An asymmetric depopulation of the Dirac cone and, thus, nonzero net current is achieved by using circularly polarized light [McI12b]. **b**, Typical shape of the resulting photocurrent $J_{inj}(t)$. Here, $I_p(t)$ is the intensity envelope of the laser pulse. **c**, Scenario of a shift photocurrent arising from an ultrafast transfer of electron density along the Se-Bi bond. **d**, Typical bipolar temporal shape of the resulting sheet current $J_{sh}(t)$. **e**, Schematic of the electronic band structure of Bi_2Se_3. While BB1/BB2 represent bulk bands below/above the Fermi level E_F, SS1/SS2 refer to surface states. Red arrows indicate three examples of pump-induced optical transitions (photon energy of ~ 1.5 eV). To better illustrate the excitation process, thin black/red lines indicate copies of SS1/SS2 shifted upwards/downwards by the pump photon energy. Ground-state occupation is displayed shaded.

The threefold azimuthal symmetry of J_x (Fig. 7.4b) suggests the electron density is displaced along the 120°-ordered p-type Se-Bi bonds [Mis97]. In fact, previous studies have shown that the electron density associated with the Dirac states is known to shift gradually from Se toward Bi atoms when energies below and above the the Dirac point are considered [Zha09, Mis97, Rou09]. As Bi and Se atoms lie in different layers, the Bi-Se bond forms an angle of about 45° with respect to the sample surface normal. Therefore, the shift current also has a z-component with a strength comparable to J_x, consistent with the sharp peak present in J_{yz} at $t = 0$ fs (see Fig. 7.5 and Fig. 7.8d).

In principle, the ultrafast Se-Bi charge transfer can be driven by all kinds of optical transitions involving surface states. Examples of possible transitions induced by the 1.57 eV pump photons are shown in Fig. 7.6e: (1) surface-to-bulk, (2) bulk-to-surface and (3) surface-to-surface (intercone) transitions. Following excitation, the charge carriers undergo multiple scattering processes, finally resulting in an isotropic distribution. The time constant (22 fs) of this process found here is consistent with other measurements of anisotropy relaxation at the TI surface: ultrafast optical Kerr effect (time constant of ~ 25 fs) [Wan16] and equilibrium transport experiments (substantially smaller than 300 fs, see Appendix 7.H) [VA12, Ban12]. Note that due to spin-momentum locking at the TI surface, the decay of the anisotropy of the charge-carrier distribution is strongly connected with the decay of the transient surface spin polarization [Zha13]. The time scales of these processes are much shorter than that of the energy relaxation of the surface charge carriers (~ 1 ps) [Sob14].

7.4.2 The absence of circular photocurrents

Result (ii), the absence of a pump-helicity-dependent photocurrent, is surprising and imposes significant constraints on the generation mechanism of this current. We first note this result is consistent with the photocurrent magnitudes found by previous electrode-based time-integrating [McI12b] and picosecond-resolved [Kas15] measurements. From these works, it follows that under excitation conditions similar to ours, the pump-helicity-dependent photocurrent reaches a peak value that is slightly below the detection threshold $10^{18}\ e\,\mathrm{m}^{-1}\,\mathrm{s}^{-1}$ of our setup (see Appendix 7.I).

It is instructive to compare the upper photocurrent limit set by our experiment to a recently suggested microscopic scenario[McI12b] in which the pump-helicity-dependent photocurrent arises from asymmetric depopulation of the Dirac cone by optical transitions into rapidly decaying bulk states (Fig. 7.6a). Based on this injection-type scenario, we use Eq. (7.3) to estimate the initial ballistic sheet-current density as $Nev_{\mathrm{D}}\Delta z_{\mathrm{D}}$, where $v_{\mathrm{D}} = 0.5\ \mathrm{nm\,fs}^{-1}$ is the band velocity in the Dirac cone [Sob14], $\Delta z_{\mathrm{D}} = 2\,\mathrm{nm}$ the thickness of the Dirac states [Zha10], and N is the bulk excitation density. The resulting magnitude of $10^{22}\ e\,\mathrm{m}^{-1}\,\mathrm{s}^{-1}$ is four orders of magnitude larger than the maximum current measured in our experiment.

Possible reasons why the photocurrent magnitude predicted by this plausible scenario so drastically exceeds the actually measured pump-helicity-dependent photocurrent are as follows. First, matrix elements for bulk-surface optical transitions are much smaller than

for bulk-bulk transitions. In other words, light absorption is much more pronounced in the bulk than at the surface, in contrast to the tacit assumption of homogeneous absorptivity made in the estimate above. Second, the band velocity of initial and final state are approximately equal [see Eq. (7.3)]. Finally, there is a great deal of cancelation when summing over the contributions of all optical transitions. Indeed, as shown theoretically, a zero net current results when only optical transitions within the Dirac cone are considered [Jun13]. Experiments employing pump pulses with tunable pump photon energy [Kur16, SB14] will likely provide more insights into the nature of the pump-helicity-dependent photocurrent, in particular in terms of intracone and below-gap optical transitions [Hos11, Jun13, Kur16].

7.5 Conclusion/Outlook

In conclusion, we have measured the dynamics of ultrafast photocurrents on the surface of the Ca-doped three-dimensional model TI Bi_2Se_3 with a time resolution as short as 20 fs. We find that the peak amplitude of pump-helicity-dependent photocurrents is much smaller than predicted by a recent model based on asymmetric optical transitions between Dirac-cone and bulk states [McI12b]. For the first time, we have observed a surface shift photocurrent which arises from a charge displacement at the TI surface. The fast decay time (22 fs) of this current attests to the rapid loss of charge-carrier surface anisotropy.

On a more applied note, the shift current is potentially interesting for ultrafast optical manipulation of the TI surface, thereby ultimately modifying its topological properties [Liu15]. The local electric field generated by the shift current could be employed to drive highly spin-polarized THz electric currents at the TI surface. The direction of this secondary current could easily be controlled by the pump-beam polarization, thereby opening up new possibilities to access the TI surface states. Finally, our results highlight broadband THz emission spectroscopy as a novel and highly sensitive probe of surfaces.

Appendix Chapter 7

7.A Sample details

Single crystals of Ca-doped Bi_2Se_3 were grown by the Bridgman-Stockbarger method by pulling a sealed quartz ampoule in a vertical temperature gradient. A fresh surface is obtained by cleaving using adhesive tape. The dimensions of the sample used for THz emission spectroscopy are approximately $2 \times 3 \times 0.3$ mm^3.

For characterization of the sample by angle-resolved photoelectron spectroscopy (ARPES), the sample was studied directly after cleaving under ultrahigh-vacuum conditions (pressure $2 \cdot 10^{-10}$ mbar) and, a second time, after exposing the sample to an ambient-pressure atmosphere of N_2 for a few seconds. ARPES measurements on the N_2-exposed surface confirm the presence of Dirac surface states with the Fermi energy located roughly 100 meV above the bulk conduction band minimum (see Fig. 7.7). From these data, a conduction-band electron mass of 0.115 bare electron masses is inferred [Xia09].

Hall measurements [Hru11] yield a bulk hole density of 1.34×10^{17} cm^{-3} and a mobility of 275 cm^2 V^{-1} s^{-1}. Using these values, the effective mass inferred from ARPES data and the Drude formula, we extract a velocity relaxation time of 18 fs in the bulk material.

7.B From electrooptic signals to THz fields

To proceed from the measured electrooptic signal $S(t)$ to the THz electric field $\mathbf{E}(t)$ directly above the sample surface, we note that there is a linear relationship between the two quantities. For example, in the frequency domain, the THz field component E_x and the corresponding signal S_x are connected by the transfer function $h(\omega)$ through the simple multiplication

$$S_x(\omega) = h(\omega)E_x(\omega). \tag{7.5}$$

A completely analogous relationship is valid for E_{yz} and S_{yz}. We measure the transfer function of our setup by using 50 µm thick GaP(110) as a reference emitter placed before the TI sample that has been substituted by an Ag mirror.

Fig. 7.9 shows the steps and transfer functions that take us from the detected electrooptic signal to the THz electric field directly after the sample (Fig. 7.9f). The calculated transfer functions [Kam13a] account for the effects of THz field propagation (h_{prop}, see Fig. 7.9a) and electrooptic detection (h_{det}, Fig. 7.9b), resulting in a total transfer function h that agrees well with that determined experimentally (Fig. 7.9c).

Fig. 7.9d displays spectra of electrooptic signals S_x and S_{yz}. Spectral features in the range from 8 THz to 15 THz correspond to the Reststrahlen band of the GaP electrooptic detector. The dip at 8 THz arises because electronic and Raman contributions to the electrooptic response of GaP cancel at this frequency. Division of the signal spectra by

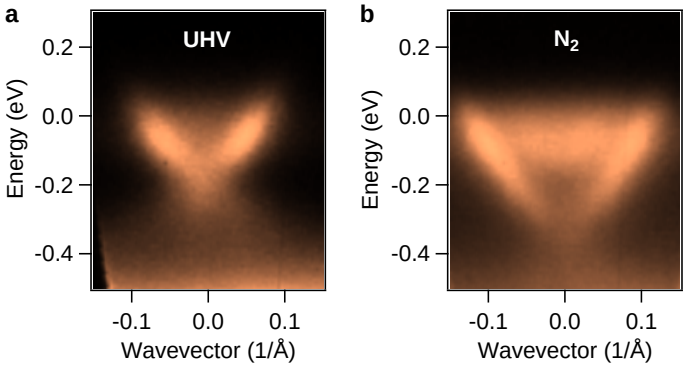

Figure 7.7: Photoemission data of the Ca-doped Bi_2Se_3 sample crystal. **a**, Angle-resolved photoemission data confirm the existence of topological surface states in our sample. Measurements on the pristine surface, obtained directly after cleaving in ultrahigh vacuum, reveal the chemical potential at the lower edge of the conduction band minimum. **b**, Following exposure to 1 bar of N_2 gas, n-type doping shifts the chemical potential into the conduction band, indicating a downward band bending at the surface on the order of 100 meV.

$h(\omega)$ greatly cancels these features and yields the field spectra E_x and E_{yz} shown in Fig. 7.9e and Fig. 7.2c. The frequencies of the spectral features at 2 THz and 4 THz agree with Bi_2Se_3 phonon resonances[Mad98b]. Below 1 THz, the response decreases sharply to zero because electromagnetic radiation is emitted less efficiently at decreasing frequency.

7.C From THz fields to THz currents

To finally obtain the source current $\mathbf{J}(t)$ from the THz electric field $\mathbf{E}(t)$ measured directly above the sample surface, we make use of the following generalized Ohm's law [Sha04]:

$$E_x(\omega) = -\frac{Z_0}{\cos\alpha + \sqrt{n^2 - \sin^2\alpha}} J_x(\omega) \tag{7.6}$$

$$E_{yz}(\omega) = -\frac{Z_0\sqrt{n^2 - \sin^2\alpha}}{n^2\cos\alpha + \sqrt{n^2 - \sin^2\alpha}} J_{yz}(\omega). \tag{7.7}$$

Here, $\omega/2\pi$ is the THz frequency, $Z_0 \approx 377\ \Omega$ is the vacuum impedance, $n(\omega)$ is the refractive index of Bi_2Se_3 taken from Ref. [VA12], $\alpha = 45°$ is the angle of incidence, and

$$J_{yz}(\omega) = J_y(\omega) - \frac{\sin\alpha}{\sqrt{n^2 - \sin^2\alpha}} J_z(\omega) \tag{7.8}$$

is a weighted sum of the currents flowing along the y and z directions. For Bi_2Se_3 and frequencies above 5 THz, the weighting factor $\sin\alpha/\sqrt{n^2 - \sin^2\alpha}$ of J_z is on the order of 0.3. The inverse Fourier transformation of the resulting current spectra yields the currents in the time domain (Fig. 7.5).

We note that the overall magnitude of the extracted currents is subject to an estimated uncertainty on the order of 3 which arises from the cumulated effects of uncertainties of beam parameters (such as beam diameter and divergence), of the precise optical material

properties (in particular close to phonon frequencies) and from the deviations of the optical and THz beam from a perfect Gaussian profile.

7.D Waveform mean amplitude

To characterize a complete THz waveform $S(t)$ by a single mean amplitude $\bar{S}$, an often-used procedure is to calculate the mean root-mean square $\left[\int \mathrm{d}t\, S^2(t)\right]^{1/2}$. The drawback of this method is that it is based on nonlinear operations which annihilate phase information and make the identification of additive signal components difficult. Therefore, calculation of a mean amplitude $\bar{S}$ of a given signal should be linear with respect to $S(t)$. Our solution is to project $S(t)$ on a suitable and normalized reference waveform $S_{\mathrm{ref}}(t)$ by means of the scalar product

$$\bar{S} = \frac{1}{N}\langle S_{\mathrm{ref}}, S\rangle = \frac{1}{N}\int \mathrm{d}t\; S_{\mathrm{ref}}(t)S(t) \tag{7.9}$$

where $N = \langle S_{\mathrm{ref}}, S_{\mathrm{ref}}\rangle^{1/2}$ normalizes S_{ref}/N to unity. As required, this operation is linear with respect to $S(t)$ and, therefore, does not mix up additive signal components.

In the case of our two-dimensional data set $S(t,\phi)$, we use the most intense signal (with respect to ϕ) as reference. This choice is arbitrary, but we checked that other reference waveforms yield qualitatively identical results within our signal-to-noise ratio. According to Eqs. (7.2) and (7.9), the basis functions $A(t)$, $B(t)$ and $C(t)$ of the data set $S(t,\phi)$ are then obtained by multiplying $S(t,\phi)$ with $1/2\pi$, $\sin(3\phi)/\pi$ and $\cos(3\phi)/\pi$, respectively, and subsequent integration from $\phi = 0$ to 2π.

7.E Azimuthal symmetry analysis

The inset of Fig. 7.2b shows the THz signal grows linearly with the pump power, that is, with the square of the pump field $\mathbf{F}(t)$. Therefore, the resulting current density can phenomenologically be described by the general nonlocal relationship[Mil12]

$$\begin{aligned} j_i(\mathbf{x},t) \;=\; & \sum_{jk}\iiiint \mathrm{d}t_1\; \mathrm{d}t_2\; \mathrm{d}^3\mathbf{x}_1\; \mathrm{d}^3\mathbf{x}_2 \\ & \sigma_{ijk}(t-t_1, t-t_2, \mathbf{x}-\mathbf{x}_1, \mathbf{x}-\mathbf{x}_2) \\ & \cdot F_j(\mathbf{x}_1,t_1)F_k(\mathbf{x}_2,t_2). \end{aligned} \tag{7.10}$$

Here, F_j is the jth Cartesian component of the pump field, and σ_{ijk} is a third-rank tensor field describing the quadratic material response. Upon sample rotation described by the matrix $R_{i'i}$, the nonlinear response function transforms according to

$$\sigma'_{i'j'k'} = \sum_{ijk} R_{i'i}R_{j'j}R_{k'k}\sigma_{ijk}. \tag{7.11}$$

When we focus on rotations about the sample normal by an angle ϕ, the matrix elements $R_{i'i}$ are given by linear combinations of of the functions 1, $\cos\phi$ and $\sin\phi$ or, equivalently,

1, $\exp(\mathrm{i}\phi)$ and $\exp(-\mathrm{i}\phi)$.

Since the $R_{i'i}$ show up in third order in the response transformation described by Eq. (7.11), the transformed $\sigma'_{i'j'k'}(\phi)$ is a third-order mixed polynomial with respect to 1, $\exp(\mathrm{i}\phi)$ and $\exp(-\mathrm{i}\phi)$, that is, a linear combination of the terms $\exp(\mathrm{i}m\phi)$ where the integer m runs from -3 to $+3$. From these seven terms, however, only $\exp(-3\mathrm{i}\phi)$, $\exp(3\mathrm{i}\phi)$ and 1 remain since our sample is invariant under rotation by $2\pi/3 = 120°$ about the surface normal. In other words, $\sigma'_{i'j'k'}(\phi)$ is a linear combination of the functions 1, $\sin(3\phi)$ and $\cos(3\phi)$.

As seen from Eqs. (7.1), (7.6), (7.7) and (7.8), the THz field emitted by the current-density distribution $\mathbf{j}$ is linear with respect to $\mathbf{j}$ with a proportionality constant that depends on the material only through the linear-optical constants at THz frequencies. Since for our sample these constants are invariant under azimuthal rotations, the ϕ-dependence of the THz signal is inherited by that of $\mathbf{j}$ and, thus, $\sigma'_{i'j'k'}$.

To summarize, the THz signal depends on the sample azimuth ϕ through a linear combination of the three terms 1, $\sin(3\phi)$ and $\cos(3\phi)$ [see Eq. (7.2)]. This conclusion is consistent with our experimental observations (see Fig. 7.4b and Fig. 7.8c).

7.F Extended symmetry analysis

While the previous subsection focused on rotations about the sample surface normal by an angle ϕ, we now also allow for variations of the pump beam's angle of incidence α (Fig. 7.1) and the polarization state of the pump field. By using the electric-dipole approximation and a Fourier transformation with respect to time, Eq. (7.10) yields the photocurrent-density amplitude[Mil12]

$$j_i(\mathbf{x},\omega) = 2\sum_{jk}\int\limits_{\omega'>0} \mathrm{d}\omega'\ \sigma_{ijk}(\mathbf{x},\omega'+\omega,-\omega')F_j(\mathbf{x})f_k^*(\mathbf{x}) \tag{7.12}$$

at THz frequency $\omega > 0$. Here, $\mathbf{F}$ and $\mathbf{f}$ are the complex-valued pump-field Fourier amplitudes at frequencies $\omega+\omega'$ and ω', respectively.

The third-rank tensor σ_{ijk} is nonzero only in regions of broken inversion symmetry, that is, at the surface region of our sample. According to the C_{3v} symmetry of the sample surface, there are only five independent tensor elements: $\eta_1 = \sigma_{xzx} = \sigma_{yzy}$, $\eta_2 = \sigma_{xxz} = \sigma_{yyz}$, $\eta_3 = \sigma_{zxx} = \sigma_{zyy}$, $\eta_4 = \sigma_{yyy} = -\sigma_{yxx} = -\sigma_{xxy} = -\sigma_{xyx}$ and $\eta_5 = \sigma_{zzz}$. The other tensor elements are zero [She84].

If the driving field has an angle of incidence α and polarization components F_s, f_s and F_p, f_p along the directions perpendicular and in the plane of incidence, respectively, the

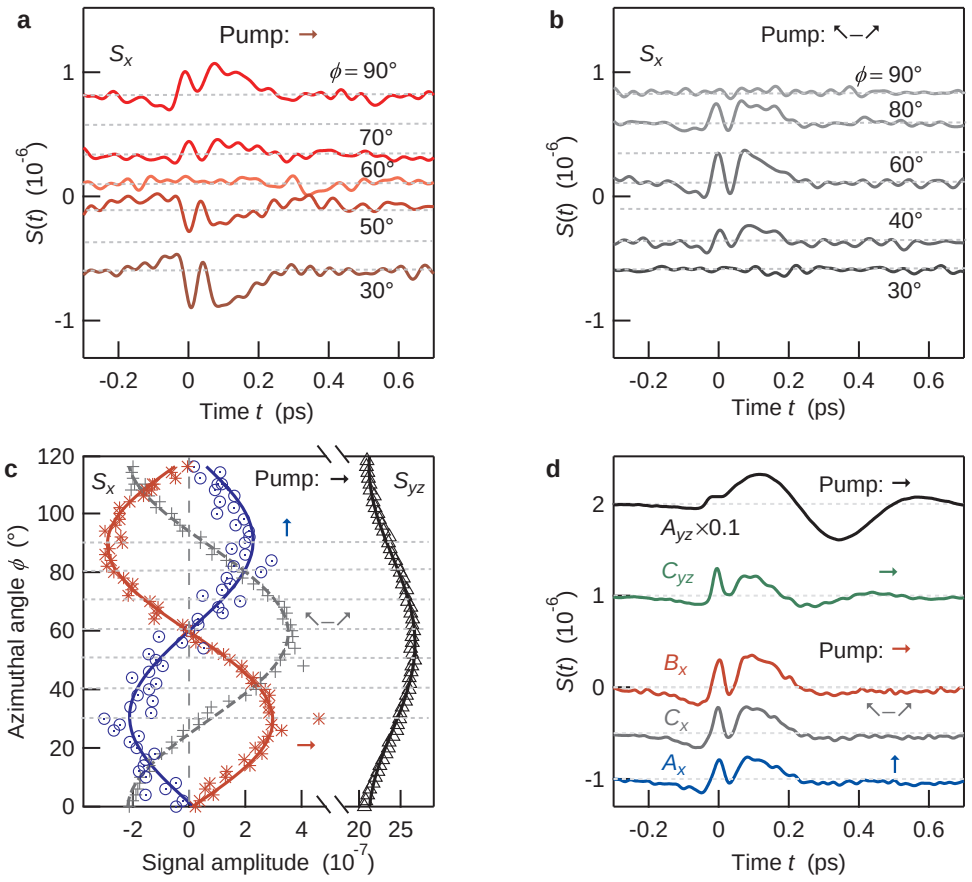

Figure 7.8: Azimuth-dependence and dominant THz signal components. **a**, THz signal waveforms at various sample azimuth angles ϕ and p-polarized pump field. **b**, Additional waveforms for the differential signals $\nwarrow - \nearrow$. **c**, Extracted THz amplitude vs ϕ for various pump-polarization settings ($\rightarrow$, $\uparrow$ and differential signals $\nwarrow - \nearrow$). Dotted lines indicate azimuthal angles of the data shown in **a** and **b**. **d**, Dominant temporal components of signal sets $S_{yz}(t,\phi)$ and $S_x(t,\phi)$ for various pump polarizations, extracted by using Eq. (7.2).

resulting photocurrents are given by

$$\begin{aligned} j_x &= -\eta_4 \cdot (F_s f_s^* - F_p f_p^* \cos^2\alpha)\sin(3\phi) \\ &\quad -\eta_4 \cdot (F_p f_s^* + F_s f_p^*)\cos\alpha\cos(3\phi) \\ &\quad -(\eta_1 F_p f_s^* + \eta_2 F_s f_p^*)\sin\alpha \end{aligned} \tag{7.13}$$

$$\begin{aligned} j_y &= -\eta_4 \cdot (F_s f_s^* - F_p f_p^* \cos^2\alpha)\cos(3\phi) \\ &\quad +\eta_4 \cdot (F_s f_p^* + F_p f_s^*)\cos\alpha\sin(3\phi) \\ &\quad -(\eta_1 F_p f_p^* + \eta_2 f_p F_p^*)\sin\alpha\cos\alpha \end{aligned} \tag{7.14}$$

$$\begin{aligned} j_z &= \eta_3 \cdot (F_s f_s^* + F_p f_p^* \cos^2\alpha) \\ &\quad +\eta_5 F_p f_p^* \sin^2\alpha. \end{aligned} \tag{7.15}$$

Here, we have omitted the frequency integral and the factor of 2 of Eq. (7.12) for brevity. These equations in conjunction with Eqs. (7.1), (7.6), (7.7) and (7.8) show that the threefold-symmetric current contributes about equally to S_x and S_{yz}, consistent with the

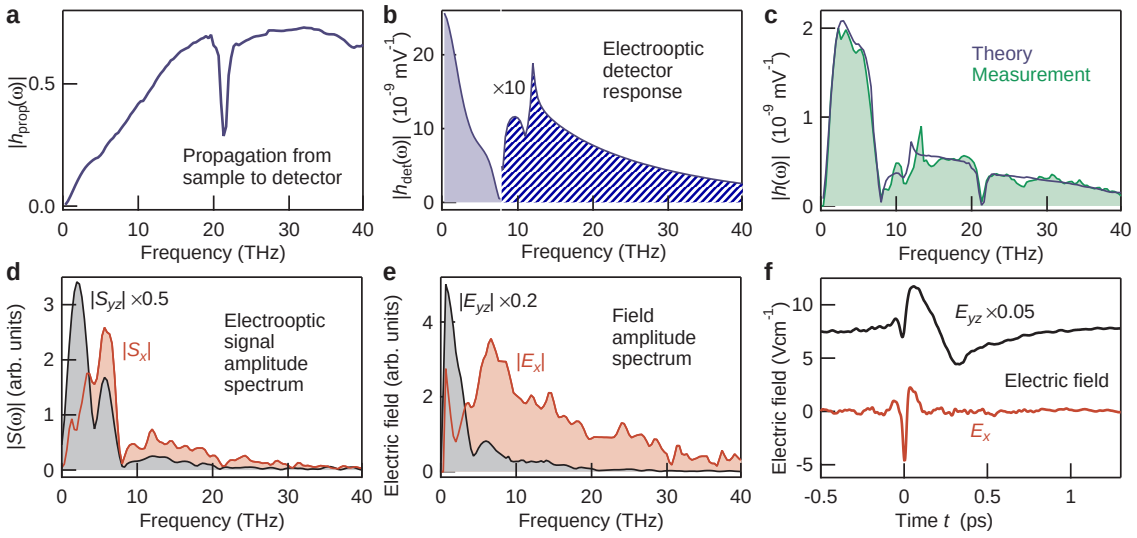

Figure 7.9: From THz signals to THz fields. **a**, Transfer function h_{prop} describing the propagation from the sample to the electrooptic detection crystal. Focusing of the THz pulse leads to the typical high-pass behavior of h_{prop}. The absorption dip at 21 THz arises from the substrate of the wire-grid polarizer used. **b**, Transfer function h_{det} of the electrooptic detection consisting of a 250 µm thick GaP(110) crystal in conjunction with a 20 fs, 790 nm sampling pulse. **c**, Measured and calculated total transfer function $h(\omega) = h_{\mathrm{prop}}(\omega)h_{\mathrm{det}}(\omega)$ of our setup over a broad bandwidth from $\omega/2\pi = 0.3$ to 40 THz. Sharp spectral dips and peaks are related to the Restrahlen band of the GaP detection crystal (see text). **d**, Spectra of typical THz emission signals S_x and S_{yz} clearly exhibit central features of the total transfer function of our spectrometer. **e**, Field spectra obtained by dividing the signal spectra of panel **d** by the transfer function h of panel **c**. **f**, Transient electric field $\mathbf{E}(t)$ of the THz pulse directly after the sample as obtained by an inverse Fourier transformation of $\mathbf{E}(\omega)$. Curves are offset for clarity.

observed amplitude variations seen in Fig. 7.8d.

Note the tensor element $\eta_4 = -\sigma_{xxy} = -\sigma_{xyx}$ is symmetric under exchange of the last two indices. Therefore, η_4 becomes purely real-valued when the frequency approaches $\omega = 0$. Based on photocurrent theory work [Nas10], this property is indicative of a shift current. In contrast, injection currents require σ_{ijk} to be purely imaginary [Nas10], which implies sign inversion under exchange of the last two tensor indices. Therefore, any possible injection or pump-helicity-dependent photocurrent is related with η_1 and η_2, and it is independent of the sample azimuth ϕ. We note these conclusions are based on the assumption of negligible current relaxation [Nas10]. Therefore, they apply at frequencies ω higher than the current relaxation rates $1/\tau_{\mathrm{inj}}$ and $1/\tau_{\mathrm{sh}}$.

7.G Signal azimuthal symmetries

The σ_{ijk} symmetry analysis (see Appendix 7.F) allows us to predict the dependence of the THz signal on the experimental geometry (including sample azimuth and pump polarization). Most notably, all signals exhibit the threefold azimuthal symmetry of the sample surface (see Fig. 7.4b and Fig. 7.8c). We now discuss features related to the dependence on ϕ and the pump polarization in more detail.

For example, when the y-axis is parallel to an in-plane mirror axis of the $Bi_2Se_3(111)$ surface ($\phi = 0°$ in Fig. 7.1), the σ_{ijk} tensor elements of the shift-current signal fulfill $\sigma_{xxy} = \sigma_{xyx}$. Consequently, the pump field amplitude vectors $(E_s, E_p) = (1, 1)$ (i.e. $\nearrow$) and $(1, -1)$ (i.e. $\nwarrow$) make an entirely reversed contribution to J_x, as is also directly apparent from Eqs. (7.13) and (7.14). Similar arguments apply when the sample is rotated by 30° (such that the in-plane mirror axis coincides with the x axis) and pump fields $(E_s, E_p) = (1, 0)$ (i.e. $\uparrow$) or $(1, 0)$ (i.e. $\rightarrow$) are used. Finally, at arbitrary ϕ, we obtain a superposition of the effects parallel/perpendicular to the mirror axis.

In Fig. 7.8, we present raw data of the shift current detected along x for (a) p-polarized pump field and (b) the difference signal ($\nwarrow - \nearrow$) for representative azimuthal angles ϕ. As expected, when the sample is rotated by 30°, the shift current signal has maximum/minimum magnitude. After a half-cycle rotation ($\phi = 60°$), the signal arising from a p-polarized pump has reversed sign. In Fig. 7.8c, we plot the amplitude dependence of the same signals (Fig. 7.8a,b) for an extended set of azimuthal angles. The amplitude dependence for s polarization as well as for the S_{yz} signal are also shown.

Having identified the symmetry of the signal (Fig. 7.8c), we use our projection method (see Appendix 7.E) to extract basis signals $A(t)$, $B(t)$ and $C(t)$ from each two-dimensional data set $S(t, \phi)$ [see Eq. (7.2) and Fig. 7.8d]. We find that the signal with threefold azimuthal symmetry observed under various pump polarizations and detector orientations derives from only one basis waveform.

7.H Spin relaxation in Bi_2Se_3

The magnitude of optically excited spin-polarized currents depends strongly on the spin relaxation time. In Bi_2Se_3 and at room temperature, optical pump-probe experiments have shown that the optically spin polarization relaxes on a time scale of 100 fs [Bos15, Wan16, McI12b].

This value is consistent with equilibrium transport measurements [VA12, Ban12]. Broadband THz conductivity measurements at 6 K yielded a velocity relaxation time of 1 ps for the surface electrons [VA12]. Due to spin-momentum locking, this time constant must equal the surface spin-relaxation time. By increasing the sample temperature to 300 K, the DC surface resistivity has been found to increase by a factor 3 [Ban12]. Therefore, an upper limit of the surface velocity-relaxation time is given by ~ 1 ps$/3 \sim 300$ fs. The precise value is probably substantially smaller than 300 fs because the increase of surface resistivity due to an increased carrier scattering rate is counteracted by the increase of carrier density with temperature (which is known to decrease resistivity).

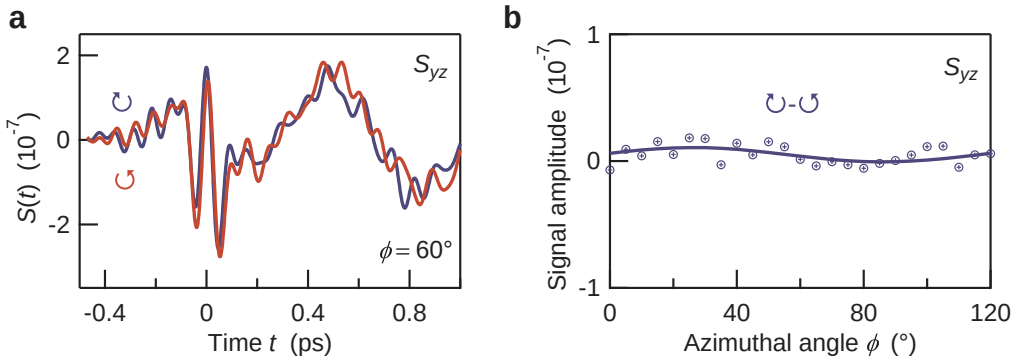

Figure 7.10: Helicity-independence of S_{yz}. **a**, Typical THz signals $S_{yz}(t)$ for circularly polarized pump pulses. **b**, Amplitude of the difference signal (↻ − ↺) for various azimuthal angles. There is no helicity dependence of S_{yz}, consistent with the σ_{ijk} symmetry analysis in Appendix 7.F.

7.I Current magnitude of the pump-helicity-dependent photocurrent

In our experiment, we find the magnitude of the pump-helicity-dependent and ϕ-independent photocurrent is below the detection threshold 10^{18} $e\,\mathrm{m}^{-1}\,\mathrm{s}^{-1}$ of our experiment (see Fig. 7.5). This result is consistent with the photocurrent magnitudes determined by previous electrode-based time-integrating[McI12b] and time-resolved[Kas15] measurements with a time resolution of ~ 1 ps.

For example, McIver *et al.*[McI12b] obtained a DC photocurrent of $\overline{J} \sim 10^{13}$ $e\,\mathrm{m}^{-1}\,\mathrm{s}^{-1}$, normalized to the pump power of our experiment. Assuming the photocurrent flows over a time $\tau_0 \sim 100$ fs and with a repetition rate of $f_{\mathrm{rep}} \sim 100$ MHz, we find the peak current amounts to $J_0 \sim \overline{J}/f_{\mathrm{rep}}\tau_0$, slightly below the detection threshold of our experiment. Note that this comparison has assumed a conservatively small current lifetime τ_0 that is determined by the pump-pulse duration used in Ref. [McI12b]. For longer lifetimes, the peak current J_0 would decrease accordingly. A similar consideration can be made for the experiment of Kastl *et al.*,[Kas15] also resulting in peak current values below the detection threshold of our setup.

We note that our straightforward comparison of electrode-based photocurrent measurements [McI12b, Kas15] with our contact-free THz emission approach is justified by the Shockley-Ramo theorem[Son14].

8 Ultrafast spin-to-charge-current conversion in $BiSbTe_3$/CoFeB

In this chapter, we investigate the spin-to-charge-current conversion in topological insulators by using bilayers of a topological insulator (TI) thin film and a ferromagentic (FM) layer. We find an ultrafast spin-injection across the FM/TI interface, that leads to an sizable current burst and, thus, to THz emission. Such ultrafast spin-current to charge-current inversion is far from obvious when it is driven at THz frequencies that correspond to the typical energy scale of spin-orbit coupling ($\sim 100\ meV \mathrel{\widehat{=}} 24\ THz$).

8.1 Motivation

Topological insulators (TIs) have robust metallic surface states with unique properties including spin-momentum locking and high mobility [Qi11, Zha09, Moo10]. The coupling of spin and momentum facilitates the exciting possibility to convert charge-currents to spin-currents by simply applying an electric field [Li14]. The induced spin accumulation can be used to electrically manipulate adjacent magnetic materials [Mel14]. For example, driving a small current in the topological insulator could efficiently read information stored in an adjacent magnetic layer, while a larger current could potentially flip the magnetic orientation, thereby writing magnetic information.

Charge-current to spin-current conversion in TIs has been demonstrated for Bi_2Se_3 / permalloy bilayers driven at microwave frequencies [Mel14]. However, to fully exploit the potential of spin-to-charge current conversion in topological insulators for spintronic devices one has to investigate such conversion at the cut-off frequency of conventional field-effect transistors, which gradually approach the THz scale [dA11]. Beside its technological potential, it is also of high fundamental interest how spin currents behave, when they are driven at THz frequencies that correspond to the typical energy scale of spin-orbit coupling (~ 100 meV $\mathrel{\widehat{=}}$ 24 THz).

In this work, we investigate the ultrafast charge-to-spin current conversion by starting with the exploratory and technically simpler to implement inverse effect. As schematically shown in Fig. 8.1, a femtosecond optical laser pulse launches an ultrashort spin-polarized current burst at the interface of a thin ferromagnetic film and a topological insulator due to the ultrafast spin-dependent Seebeck effect [Ale16]. When the current enters the TI, spin-orbit coupling converts the spin current into a transverse charge current. Recently, our group could show that such spin-to-current conversion in metallic bilayer structures of thin ferromagnetic Iron and Platinum is extremely efficient. It was shown, that the induced ultrafast charge current is so large that it emits radiation in the THz range that outperforms standard THz emitters (e.g. 1 mm ZnTe) in amplitude and bandwidth [Sei16].

Here, we show in a proof-of-principle study that indeed the optical excitation of a bilayer of CoFeB and $(Bi_{0.63}Sb_{0.43})_2Te_3$, an intrinsic bulk insulating TI, emits THz radiation, thereby

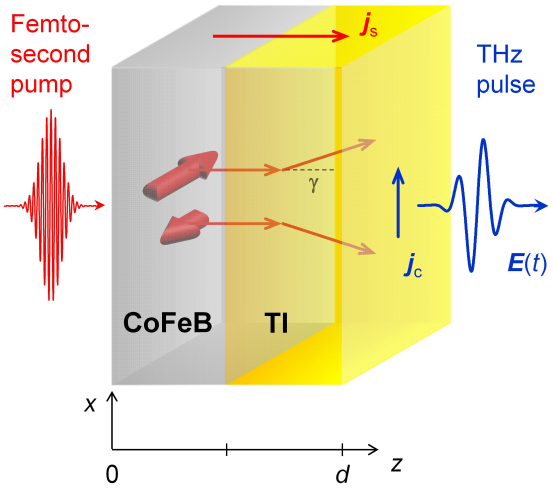

Figure 8.1: Spin-to-charge current conversion by the inverse spin Hall effect. A fs optical laser pulse launches a spin-polarized charge current from a thin ferromagnetic CoFeB film into a $BiSbTe_3$ thin film due to the spin-dependent Seebeck effect. When the current enters the TI, the strong spin-orbit coupling converts the spin current into a transverse charge current that emits an electromagnetic pulse in the THz frequency range.

indicating ultrafast spin-to-charge current conversion. We discuss tuning parameters to optimize the conversion process in TI materials.

8.2 Experimental details

8.2.1 Detection of ultrafast spin transfer

The experiment is sketched in Fig. 8.1. A FM/TI bilayer is excited with optical laser pulses (10 fs, 800 nm, 50 mW, 80 MHz) focused on a 50 µm spot. The resulting ultrafast charge transport in the FM/TI bilayer causes emission of an electromagnetic pulse, potentially extending to frequencies up to the THz range. The emitted dipole radiation is collected and co-propagated with a time-delayed optical probe pulse through a 1 mm ZnTe crystal, where it is detected via electo-optic sampling [Fer02a]. The sample is excited under normal incidence.

8.2.2 Ferromagnet/topological-insulator bilayer

The sample is a 3 nm ferromagnetic CoFeB layer on a 150 nm $(Bi_{0.63}Sb_{0.43})_2Te_3$ ($BiSbTe_3$) film on a Si(111) substrate. We apply an external magnetic bias field of about 0.1 T that saturates the in plane magnetization of the 3 nm FM layer. For comparison, we also measure THz emission from a 3 nm CoFeB film on a MgO substrate and a 150 nm $BiSbTe_3$ film on Si(111). All samples are protected against oxidation by a 2.5 nm MgO capping.

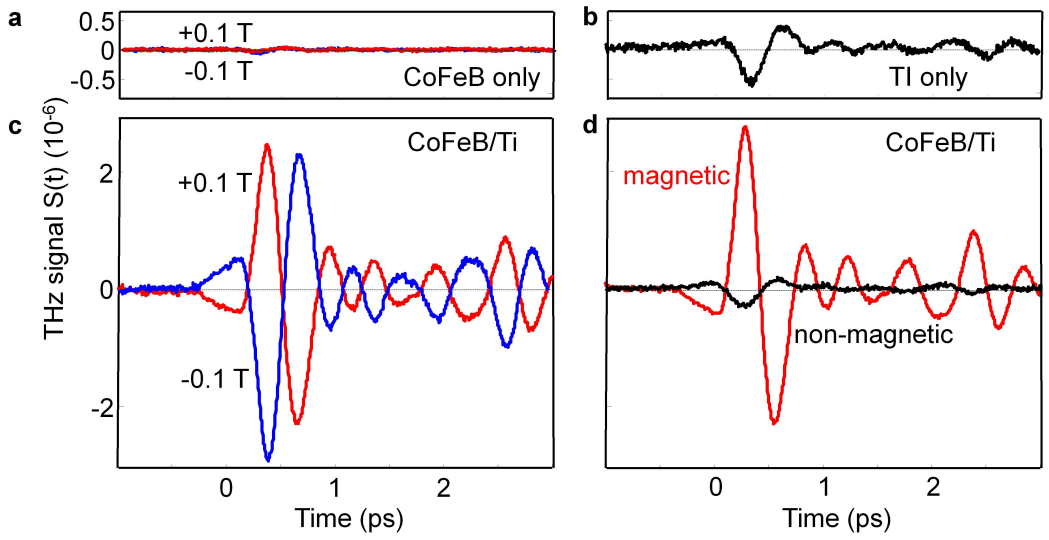

Figure 8.2: Raw data: THz emission of three samples in an external field of 0.1 Tesla. **a**, Emission signals of a single ferromagnetic CoFeB layer, **b**, a single topological insulator (TI) layer and **c**, a FM/TI bilayer. The individual components show only small THz emission signals. The bilayer signal (**c**) is significantly enhanced and the magnetic field dependence is about two orders of magnitude larger than in the pure CoFeB film (**a**). **d**, Magnetic field dependent and independent components of data shown in (**c**).

8.3 Results

Fig. 8.2a shows THz emission signals from a single 3 nm CoFeB layer in an external magnetic field excited by our 10 fs optical stimulus. The emitted field is very small, close to our detection threshold of 0.1 V/cm (field strength directly after the sample). When we reverse the magnetic field orientation from +0.1 T to −0.1 T, we observe an amplitude variation of $\sim 10\%$. Secondly, when we excite a single TI layer we find it emits THz pulses with an amplitude about an order of magnitude stronger than the signal from the pure CoFeB film (Fig. 8.2b). The emission is independent of the magnetic field (not shown).

Strikingly, as seen in Fig. 8.2c, the combination of both films leads to an emission signal enhanced by a factor ~ 5 compared to the pure TI film. The magnetic-field-dependent component is about two orders of magnitude larger than the signal from the pure FM layer.

8.4 Discussion

We have shown that ultrashort laser excitation of bilayers of a thin FM and a TI (Fig. 8.2c) leads to the emission of radiation in the THz frequency range. The emitted radiation is found to be at least a factor of ~ 5 higher than any other emission signal (Fig. 8.2a,b) observed from the individual layers alone. The THz source current is found to flow in the sample plane since our detection geometry ensures that no current along the sample normal can be detected. We find that the field direction and, thus, the current direction

reverses with the magnetic field aligned parallel to the sample surface.

These results are consistent with the mechanism outlined in Fig. 8.1 and, thus, consistent with a SH current that can flow in the bulk material of topological insulators. However, in the TI interface states a transverse spin accumulation can also be induced by the Rashba-Edelstein (RE) effect that associates spin currents to charge currents flowing in spin split bands. Such RE charge-current to spin-current conversion was demonstrated in Bi_2Se_3/permalloy bilayers at microwave frequencies [Mel14] and the inverse effect was shown to be operative at 10 GHz [RS16].

Since both iRE and iSH effects may contribute to our signal, further studies on the spin diffusion length may allow to separate the RE effect confined to the interface state (~ 2 nm) and the SH effect in the bulk by variation of the sample thickness. A further promising route to separate interface and bulk effects is to exploit the fact that iSH and iRE effect depend on the mobility of interface and bulk carriers and tuning the Fermi level position may strongly alter the mobility of the interface carriers [Koi15]. Therefore, Fermi level tuning with gate voltages or material doping as well as thickness variation of the TI film is of fundamental interest to explore spin-to-charge current conversion in TIs and disentangle the role of the TI bulk and the TI interface.

Finally we note that contributions of bulk and surface not only cause a more complex spin-to-charge current conversion process in TIs than in normal metals, but also cause a large optimization potential to significantly enhance the conversion process. Note the amplitude of the emitted THz radiation, indicating the conversion efficiency, from our not optimized TI/CoFeB bilayer, is already about 1% of the optimized Pt-based spintronic THz emitter [Sei16].

8.5 Conclusion/Outlook

Our results show the proof of principle that the strong spin-orbit coupling in topological insulators can be exploited to convert spin-currents to charge-currents in FM/TI bilayers at THz frequencies. In the future, treatment of the interface roughness or interface-dusting as well as variation of the TI film thickness, has to show if the iSH effect in the bulk material and/or the iRE effect drive the conversion. We have shown that the conversion efficiency in TIs is sizeable. Therefore, tuning of sample thickness and Fermi level position have a great potential to enhance the THz emission to application-oriented relevance. For example, the field of THz spectroscopy is still in need of efficient emitters of broadband THz radiation that can be driven with a low-cost femtosecond laser oscillator.

9 Sum frequency excitation of coherent phonons in Bi_2Te_3 and Sb_2Te_3

In this chapter, we replace the optical pump by a strong THz electric field to drive electron and lattice dynamics and study their relaxation with subsequent time-delayed laser pulses that probe the pump induced optical anisotropy. Importantly, the low pump photon energy (4meV) induces an excited state that can be described by a Fermi-Dirac distribution and, thus, we can investigate the ultrafast energy relaxation of electrons under conditions similar to those in electronic devices. We find that quasi-thermal electrons at the topological insulator interface relax significantly faster than those in the bulk material. To obtain these results, we show how THz-pump-optical probe experiments in combination with variation of the film thickness can access electron and lattice dynamics at a buried interface. We further find that a pump-induced charge-carrier displacement drives a coherent phonon at the same interface. Remarkably, and in stark contrast to all previous coherent phonon studies, the pump-induced force acting on the lattice oscillates at the sum-frequency (rather than the difference frequency) of all frequency pairs of the THz pump spectrum. We show that these results are general as they where observed in n-type Bi_2Te_3 *as well as in p-type* Sb_2Te_3.

9.1 Motivation

Topological insulators (TIs) have robust metallic surface states with unique properties including spin-momentum locking and reduced backscattering [Qi11, Zha09, Moo10]. The coupling of spin and momentum facilitates the exciting possibility to launch spin-polarized charge currents by simply applying an electric field [Bru10b, Li14], a property of high interest for applications in spintronic devices.

Up to now, however, most transport measurements on topological insulators have been performed at frequencies below 10 GHz [Mel14], significantly lagging behind charge carrier switching rates in conventional field-effect transistors, which gradually approach bit rates on the THz scale [dA11]. Fundamental scattering processes occur on timescales of $\sim$ 10 - 1000 fs (1 - 100 THz), which is often addressed with fastest available stimuli [Sun02]. So far optical pump-probe experiments have provided insight into the sub-picosecond dynamics of carriers excited to an energy of $\sim$ 1 eV above the Fermi energy E_F [Sob14, Oni15]. In contrast, electric-field-driven transport in electronic devices is carried by electrons close to the Fermi energy. Therefore, to address the ultrafast dynamics of near-equilibrium carriers an excitation energy below the thermal energy ($k_BT \approx 25$ meV at room temperature) is desired. Beside the switching rate, a further material challenge is the high electric peak field amplitude in transistors. For example, if we assume a source-drain distance of 10 nm and a typical bias voltage of 1 V [Fio14], the corresponding peak field amplitude is as high as 1 MV/cm. Therefore, to fully exploit the potential of TIs for future information processing and high field devices charge and spin transport must proceed at THz rates

and high electric fields also. To explore the underlaying fundamental electronic scattering processes intense THz-pulses are ideal suited.

Here, we use ultrashort electric-field pulses, centered at 1 THz (4 meV) with a peak field amplitude of 1 MV/cm to drive near-equilibrium dynamics in thin films of the topological insulators Bi_2Te_3 and Sb_2Te_3 that have a band gap of $\sim$ 150 meV [Zha09]. The small excitation energy has the incentive benefit not to drive interband transition across the TI band gap and the long THz-pulse wavelength allows us to excite front and rear-interface in the TI thin-films homogeneously without field gradients. We observe electron and lattice dynamics occurring on $\sim$ 100 fs - 10 ps. We find a strong dependence of signal amplitudes on the sample thickness and show that thickness variation in the order of the optical penetration depth can be used to separate bulk and rear-interface signals. Comparison of n-type Bi_2Te_3 and p-type Sb_2Te_3 provides us insight into electron-phonon relaxation in the near-equilibrium regime. Finally, we reveal a new sum frequency Raman mechanism that drives the E_g^2 phonon.

9.2 Experimental details

Fig. 9.1a shows a schematic of our THz-pump-optical-probe setup. An electric field transient $E(t)$ (1 THz central frequency, peak field $\sim$ 1 MV/cm, Fig. 9.1b) from a $LiNbO_3$ source [Wu14] excites topological insulator thin-films on Si(111) substrates. A time delayed approximately *s*-polarized (that is perpendicular to the plane of incidence) sampling pulse (7 fs, 800 nm) probes the pump-induced anisotropy change of the material [Dha94] in reflection geometry with a pair of balanced photodiodes. Pump and probe are incident collinear under an angle of incidence of approximately 45° to the sample normal.

Our samples are thin-films of Bi_2Te_3 (13 nm and 34 nm thick) and Sb_2Te_3 (15 nm and 37 nm) on Si(111) substrates. Their structural properties are very similar and because the bulk of both samples belongs to space group D_{3d}^5 with a conventional hexagonal unit cell, consisting of periodically arranged layers of Bi (Sb) and Te stacked to quintuples along the c axis [Wan13]. The five atoms in each primitive cell give rise to three acoustic phonon branches and twelve optical phonon branches. The twelve optical branches are two A_{1g} and two E_g modes (all Raman active) and two A_{1u} and two E_u modes (IR active). The transverse modes are degenerate [Wan13]. Throughout this study we focus on Bi_2Te_3 and support our results with measurements on Sb_2Te_3.

9.3 Raw data Bi_2Te_3

The pump induces signal of a 34 nm thick Bi_2Te_3 thin-film is shown in Fig. 9.1b. Upon excitation with the intense THz pump pulse, the signal features a step-like rise and a monoexponential decay. When we perform the same measurement on a 13 nm thick sample, we observe a similar step-like response which, however, initially decays much faster.

Surprisingly, when we rotate the sample by 90° around the sample normal, we observe a

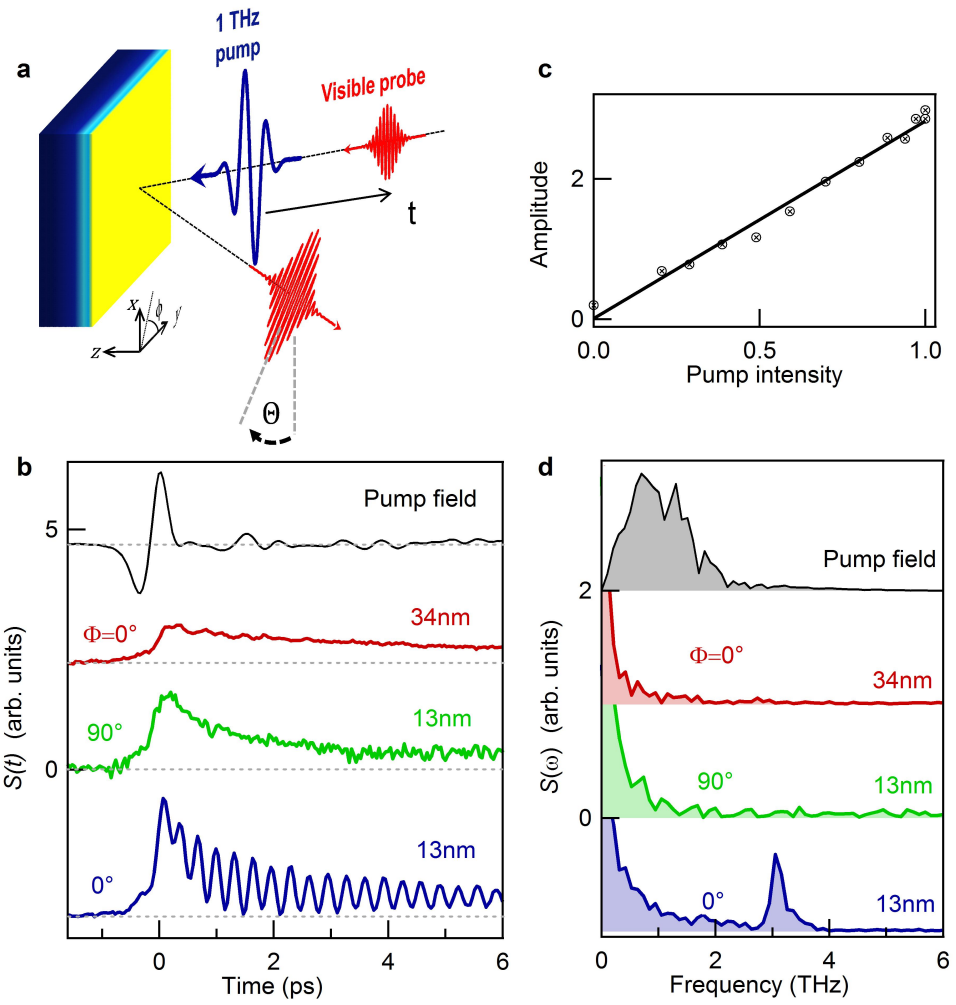

Figure 9.1: Intense THz excitation of topological insulators. **a**, An intense THz field excites a Bi_2Te_3 thin film. The transient modulation of the refractive index is detected with a time-delayed 7 fs laser pulse. **b**, Transient electric field of the pump pulse and pump-induced variation of the dielectric function for two sample thicknesses and azimuthal orientations. **c**, Fluence dependence of the oscillation amplitude in the 13 nm sample. **d**, Fourier spectra of the data shown in **b**. Signals are offset for clarity

strong oscillatory component that appears in the 13 nm sample only. Remarkably, the oscillation frequency of 3.08 THz is significantly outside the amplitude spectrum of the pump pulse (Fig. 9.3d).

We emphasize that all signal amplitudes increase linearly with the pump fluence as shown in Fig. 9.1c, thereby ruling out strong-field effects. This fact is important since the 1 MV/cm pump pulses could, in principle, accelerate charges to energies of ~ 1 eV[Kam13b], much larger than the pump photon energy and the bulk band gap of the sample. Such effects, however, have a highly nonlinear fluence dependence, a behavior that is not observed in our experiment.

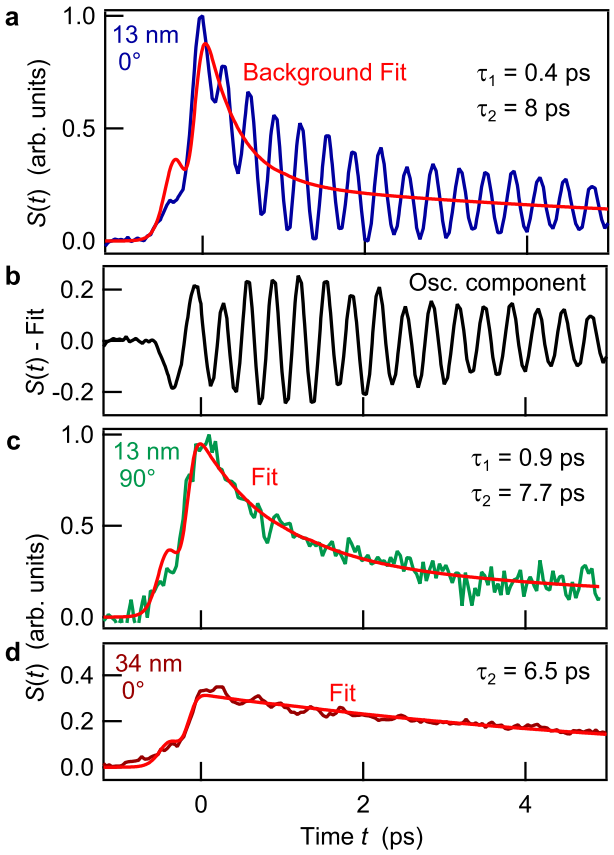

Figure 9.2: Separation of lattice and electronic response. **a**, Fit of the electronic background in the 13 nm sample. **b**, Oscillatory component extracted from **a** by substracting the electronic background. **c**, Electronic decay in the 13 nm sample rotated by 90°. **d** Signal from the 34 nm sample and fit to electronic decay.

9.4 Signal separation

As can be seen from Fig. 9.1b, the detected signal has two contributions: a step-like response and an oscillatory component that appears in the 13 nm sample only. The oscillation frequency of 3.08 THz corresponds to the E_g^2 Raman mode of Bi_2Te_3 [Wan13]. Since the E_g^2 mode is antisymmetric, its excitation induces a change in the offdiagonal elements $\Delta\epsilon_{xy}$ of the dielectric function that can be measured with our anisotropic detection scheme. The A_{1g} Raman modes are symmetric and consequently not observed in our experiment.

The step-like background signal relaxes on a picosecond timescale (Fig. 9.2a). we assign it to the dynamics of the electronic subsystem. The picosecond lifetime is surprisingly long for a pump-induced electronic anisotropy, which is expected to relax with the Drude scattering time of 75 fs in our sample (see Appendix). Therefore, this signal cannot be assigned to anisotropic electron decay $\Delta\epsilon_{xy}$ but rather to isotropic electron relaxation. The resulting $\Delta\epsilon_{xx}$ appears in our signals even though it is strongly reduced by the anisotropic detection scheme. Consequently, we measure anisotropic and isotropic electron and phonon dynamics simultaneously.

To separate electron and phonon response, we fit the electronic signal $K(t)$ of the electrons with a double-exponential function convoluted with our pump pulse intensity:

$$K(t) = \{\Theta(t)\,[A_1\,\exp(-t/\tau_1) + A_2\,\exp(-t/\tau_2)]\} * E^2(t) \tag{9.1}$$

Here, A_1 and A_2 are scaling factors and $\Theta(t)$ is the Heaviside step function.

Fig. 9.2a shows a fit of Eq. (9.1) to the data of the 13 nm sample at 0° azimuth. The fit reproduces the sharp rice of the signal well and the picosecond-relaxation follows approximately the offset of the oscillatory component (Fig. 9.2a). The fast-component allows us to define the time zero of pump and probe overlap with a precision of 30 fs. The fit of the offset signal enables us to separate electron and phonon dynamics by simply subtracting the fit from the raw data. Fig. 9.2b shows the remaining oscillatory component, which we will discuss in Section 9.6.3.

9.5 Electronic component

To gain insight into the electronic response and possibly identify signatures of surface and bulk dynamics, we compare results for two sample orientations and two film thicknesses. Figs. 9.2a,c,d show fits of Eq. (9.1) to the data sets of these samples. We find that the step-like charge carrier response of the 13 nm thick sample follows a double exponential decay (Fig. 9.2a). The resulting decay times τ_1 and τ_2 are shown in Table 9.1. Note τ_1 and τ_2 are, respectively, very similar for sample azimuth 0° (Fig. 9.2a) and 90° (Fig. 9.2c). Since an anisotropic response is expected to occur only for $\Phi = 0°$, the similarity of the relaxation supports the assignment of this signal to an isotropic electronic relaxation mainly independent of the lattice oscillation occurring at 0° azimuthal sample orientation. The slightly shorter τ_1 for $\Phi = 0°$ may indicate an additional fast component of electronic anisotropy relaxation, not considered in Eq. (9.1) (Fig. 9.2c).

Remarkably, when we fit Eq. (9.1) to data of the 34 nm sample, we find that the electronic signal relaxes with a single decay time, only (Fig. 9.2d). We will show in Section 9.7 that we can use this thickness dependence to assign the two electronic decay times τ_1 and τ_2 to interface and bulk contributions.

9.6 Resonant sum-frequency Raman excitation

We now focus on the strong oscillations observed for the 13 nm sample only. The oscillation frequency of 3.08 THz coincides with the E_g^2 transverse phonon mode [Wan13]. Since the signal amplitude increases linearly with the pump power (Fig. 9.1c), the oscillations are not driven by a single field interaction E (Fig. 9.3a) but rather by a two field interactions E^2, that is, a Raman-type interaction (Fig. 9.3b).

Note that conventional Raman excitation (Fig. 9.3b) is based on difference-frequency (DF) mixing of the two interacting fields, a familiar phenomenon in nonlinear optics. However, a quadratic field interaction is also accompanied by the generation of signals at the sum

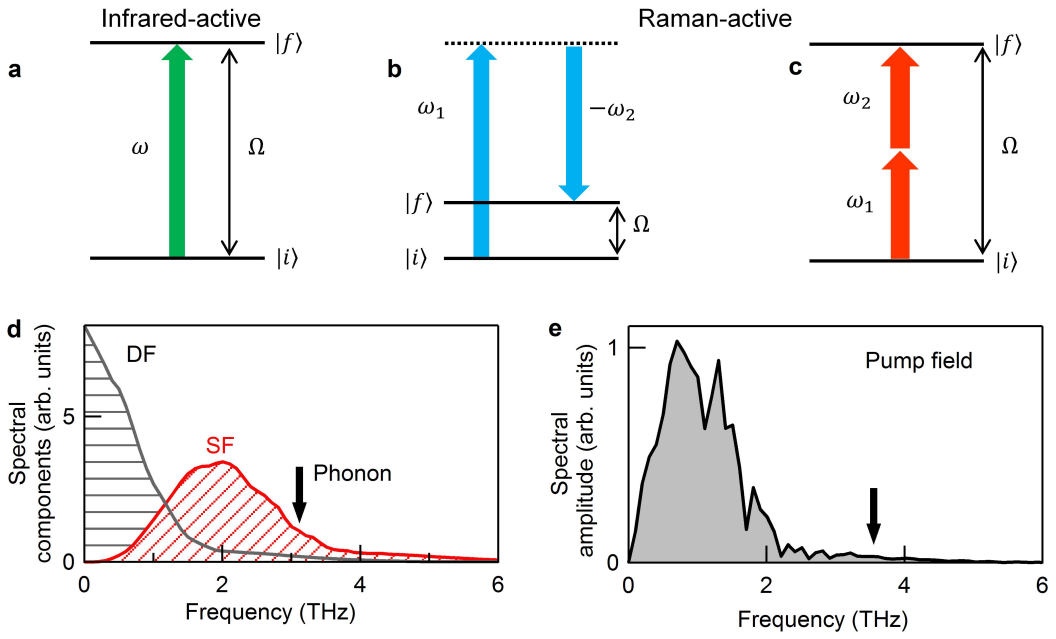

Figure 9.3: Comparison of coherent phonon driving mechanism. **a**, IR-excitation: the pump frequency ω is resonant with the phonon mode Ω. **b**, Raman excitation via difference mixing of two fields (ω_1, ω_2) to drive a phonon mode (Ω). **c**, Excitation of the same resonance via sum frequency Raman scattering. **d**, Driving field components. At the phonon frequency, 3.08 THz, the SF component is ~ 5 times stronger than the DF component. **e**, Amplitude spectrum of the pump pulse.

of the incident frequencies (Fig. 9.3c). Such sum-frequency (SF) Raman scattering has been so far neglected because the laser frequencies (~ 500 THz) were typically one order of magnitude higher than the highest phonon resonances (~ 40 THz).

9.6.1 Sum-frequency or difference-frequency excitation?

To determine whether DF or SF Raman scattering induce the coherent phonon observed in Bi_2Te_3, we write down the most general quadratic relationship between the phonon amplitude $Q(t)$ and the driving THz field $E(t)$

$$Q(t) = \int\int \mathrm{d}t_1 \mathrm{d}t_2 \; R(t-t_1, t-t_2) E(t_1) E(t_2). \tag{9.2}$$

We assume the two subsequent field interactions occur within a certain memory time, which is short compared to the pulse duration. The upper limit of this memory time is given by the Drude relaxation time, which we measure to be 75 fs (see Appendix), more than one order of magnitude shorter than the inverse central excitation frequency (1 THz=1/ps). Therefore, we can make the approximation $R(t-t_1, t-t_2) \propto \delta(t_1 - t_2)$, and Eq. (9.2) simplifies to

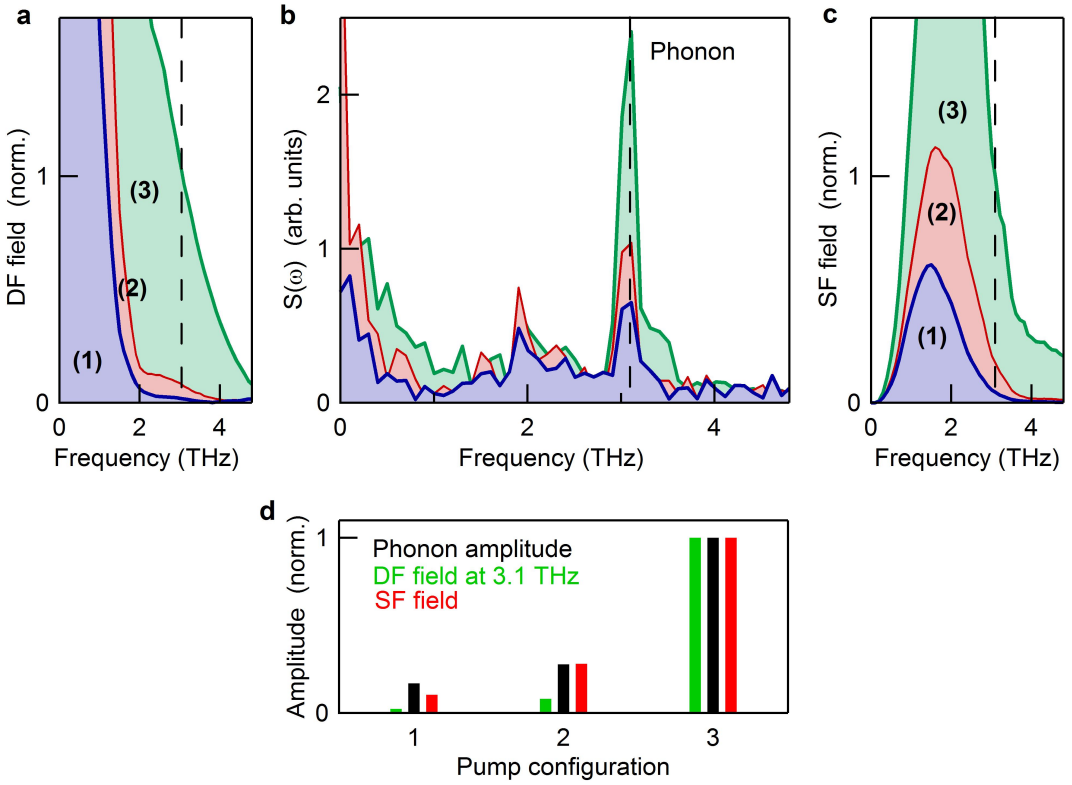

Figure 9.4: DF and SF force for three different pump configurations. **a**,**c**, Force spectra resulting from DF and SF Raman for three pump configurations $j \in \{1, 2, 3\}$. **b**, Corresponding signal spectra. **d**, DF and SF driving force magnitude at the phonon frequency 3.08 THz for each pump configuration normalized to the phonon amplitude $|Q_j|$, obtained from data in (**a-c**)

$$Q(t) \approx \int \mathrm{d}t_1 \; R(t - t_1, t - t_1) E^2(t_1) = (R * E^2)(t) \tag{9.3}$$

which in Fourier space reads as

$$\tilde{Q}(\Omega) \approx \tilde{R}(\Omega) \mathcal{F}\left(E^2(t)\right). \tag{9.4}$$

We can write the Fourier spectrum of the squared pump field $E^2(t)$ as the sum of a DF and a SF contribution:

$$\begin{aligned} \mathcal{F}\left(E^2(t)\right)(\Omega) = & \underbrace{\int_0^\infty \int_0^\infty \mathrm{d}\omega_1 \mathrm{d}\omega_2 \widetilde{E}(\omega_1) \widetilde{E}(-\omega_2) \delta(\Omega - (\omega_1 - \omega_2))}_{\mathcal{F}\left(E^2|_{\mathrm{DF}}\right)(\Omega)} \\ & + \underbrace{\int_0^\infty \int_0^\infty \mathrm{d}\omega_1 \mathrm{d}\omega_2 \widetilde{E}(\omega_1) \widetilde{E}(\omega_2) \delta\left(\Omega - (\omega_1 + \omega_2)\right)}_{\mathcal{F}\left(E^2|_{\mathrm{SF}}\right)(\Omega)}. \end{aligned} \tag{9.5}$$

To reveal whether DF or SF components make the dominant contribution in our experiment, we exploit the fact that variation of the pump pulse should have different impact on $E^2|_{\mathrm{DF}}$ and $E^2|_{\mathrm{SF}}$. Therefore, we consider various pump pulses $E_j(t)$, $j \in \{1,2,3\}$, obtained by applying various filters to the pristine pulse: 0.5 mm fused silica, 1 mm Teflon and no filter.

Each pump configuration $j \in \{1,2,3\}$ causes individual DF and SF driving fields as shown in Fig. 9.4a together with the amplitude spectra of the respectively induced phonon response. For convenient comparison, we normalize all amplitudes to pump configuration $j = 3$:

$$\frac{\mathcal{F}(E_j^2)(\Omega)|_{\mathrm{SF}}}{\mathcal{F}(E_3^2)(\Omega)|_{\mathrm{SF}}} \quad ; \quad \frac{\mathcal{F}(E_j^2)(\Omega)|_{\mathrm{DF}}}{\mathcal{F}(E_3^2)(\Omega)|_{\mathrm{DF}}} \quad \text{and} \quad \frac{|\tilde{Q}_j(\Omega)|}{|\tilde{Q}_3(\Omega)|}. \tag{9.6}$$

The normalized amplitudes are shown in Fig. 9.4d. We observe that the phonon amplitude follows the trend of the SF component in an unambiguous manner, thereby revealing that a sum-frequency excitation is the macroscopic mechanism that drives the 3.08 THz phonon.

9.6.2 Is the phonon force impulsive?

Having revealed a SF Raman process as the dominant contribution, we now explore the time structure of the force $F(t)$ driving the lattice oscillations. For this purpose, we divide the phonon driving mechanism in two subsequent steps:

$$E^2(t) \xrightarrow{C_{\mathrm{FE}}} F(t) \xrightarrow{C_{\mathrm{QF}}} Q(t). \tag{9.7}$$

First, the field E^2 is transformed into a driving force F through C_{FE}, which is almost equivalent to the stimulated Raman tensor, and second, F drives the phonon coordinate Q through a lattice response C_{QF}. C_{FE} and C_{QF} are linear transfer functions that describe the conversion steps. The impulse response,

$$C_{QF}(t) = \Theta(t)\exp(-\gamma_{\mathrm{ph}}t)\sin(\Omega t), \tag{9.8}$$

can be obtained from considering the phonon as a driven damped harmonic oscillator with resonance frequency Ω_0 and damping constant γ

$$\left(\partial_t^2 + \gamma\partial_t + \Omega_0^2\right) Q(t) = F(t). \tag{9.9}$$

To describe the driving force $F(t) = (C_{\mathrm{FE}} * E^2)(t)$, there are three standard models, which we discuss in the following.

(i) Impulsive stimulated Raman scattering (ISRS)

Pump-transparent materials have a very short memory of the driving field E^2, much shorter than the phonon oscillation period. Consequently, the transfer function C_{FE} is δ-like, and,

therefore, called impulsive. The resulting force F is proportional to the instantaneous laser intensity [Yan85],

$$F(t) \propto E(t)^2. \tag{9.10}$$

This model is known as impulsive stimulated Raman scattering (ISRS) [Yan85].

(ii) Displacive excitation of coherent phonons (DECP)

In pump-opaque matter, energy dissipation into the electronic system can cause another extreme case of excitation: displacive excitation of coherent phonons (DECP) [Zei92]. Here, the force arises from a displacement of the electron density distribution via resonant excitation of charge carriers [Zei92]. Consequently, the force can be longer-lived than the driving pump field. The transfer function is often modeled as $C_{\mathrm{FE}} \propto \Theta(t)\mathrm{e}^{-t/\tau_e}$ where τ_e quantifies the lifetime of the electronic excitation and thus, force. Therefore, the force is

$$F(t) \propto \int_0^t \mathrm{d}t' \; \Theta(t')\mathrm{e}^{-t'/\tau_e} E(t-t')^2. \tag{9.11}$$

Originally, the DECP mechanism was proposed for the spatial case of high-symmetry modes that are excited by a pump-induced gradient along the sample normal [Zei92]. To drive the E_g^2 mode of Bi_2Te_3, oscillating in the sample plane, an anisotropic charge displacement in the (0001) plane is required. The pump-induced electronic anisotropy vanishes on the timescale of momentum relaxation [Li13]. Therefore, we approximate τ_e with the Drude relaxation time in Bi_2Te_3 (75 fs, see Appendix).

(iii) Generalized phonon response

A more general description of the transfer function describing the force was derived by Li *et al.* [Li13] who obtained

$$C_{\mathrm{FE}}(\omega_1, -\omega_2) \propto \frac{\epsilon(\omega_1) - \epsilon(-\omega_2)}{\omega_1 - \omega_2 + i\Gamma} \tag{9.12}$$

Here, Γ accounts for a finite lifetime of the excitation. Note that this expression refers to DF Raman excitations, because it describes the excitation with a field $E(\omega_1)$ going "up" and a second field $E(-\omega_2)$ going "down" as illustrated in Fig. 9.3b. Thus, for a SF Raman excitation, we heuristically replace $-\omega_2$ by ω_2 since both fields go "up" (Fig. 9.3c). We obtain

$$C_{\mathrm{FE}}(\omega_1, \omega_2) \propto \frac{\epsilon(\omega_1) - \epsilon(\omega_2)}{\omega_1 + \omega_2 + i\Gamma} \tag{9.13}$$

This transfer function is of interest for Raman excitations when the excitation cannot be described in one of the limiting cases, impulsive or displacive. We put Eq. (9.13) to test by assuming that the electronic response has no memory, $\epsilon(t) \propto \delta(t)$, which is the limiting

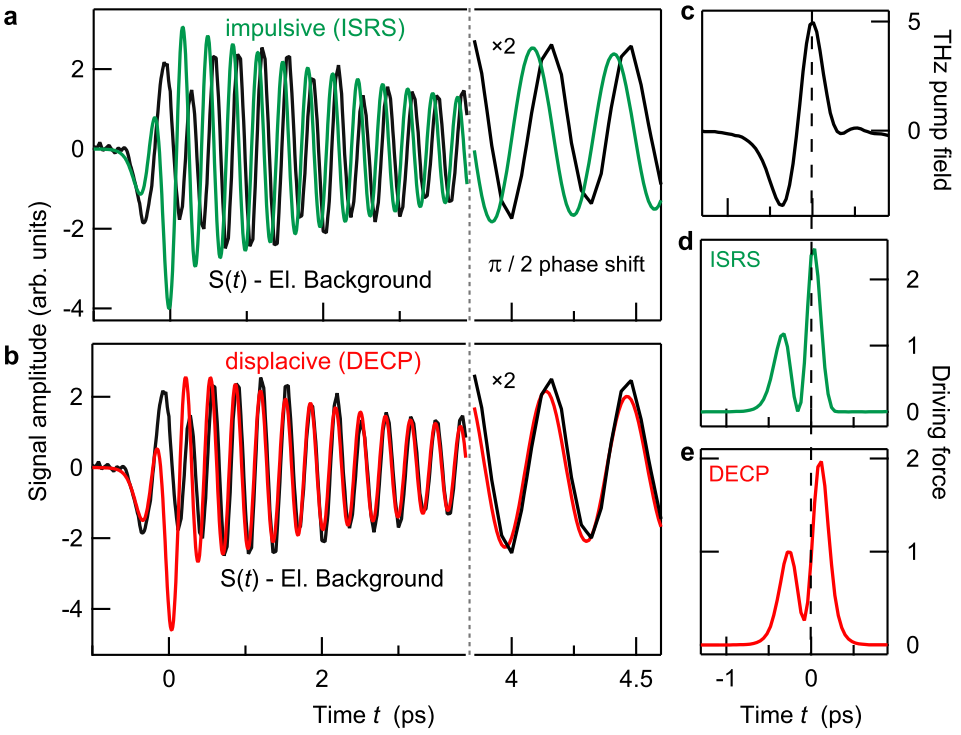

Figure 9.5: Coherent phonon modulation: DECP vs ISRS. **a**, Time domain data of the coherent phonon oscillation and fit for the ISRS model. A clear $\pi/2$ phase shift shows the failure of the model. **b**, Same as **a**, but modeled for DECP. The perfect agreement shows that the driving force is displacive. **c** Driving field as measured. **d-e** Impulsive and displacive driving forces.

case of ISRS. We follow Ref. [Li13] and Taylor-expand Eq. (9.13) around ω_1 and obtain

$$C_{\mathrm{FE}} \propto \left.\frac{\partial \epsilon}{\partial \omega}\right|_{\omega_1} \frac{\omega_1 - \omega_2}{\omega_1 + \omega_2 + i\Gamma}. \tag{9.14}$$

THE ISRS scenario implies a constant $\epsilon(\omega)$ over all frequencies. Consequently, the difference in Eq. (9.14) is zero, and therefore this model predicts no response for the situation considered here. It appears that the generalized model of the stimulated Raman force is not directly applicable to the usually neglected SF excitation. For this reason, we restrict data modeling to (i) ISRS and (ii) DECP.

9.6.3 Fit results

To reveal if the time structure of the driving force is impulsive or displacive, we fit both models, ISRS and DECP, to the phonon oscillation obtained after subtraction of the electronic background (Fig. 9.2b). The fit function of the oscillatory component is simply the convolution of the driving force with the impulsive response of a harmonic oscillator (Eq. (9.8)).

$$S(t) \propto Q(t) = [\exp(-\gamma_{\mathrm{ph}} t)\sin(\Omega t)] * F(t) \tag{9.15}$$

The fit parameters are the phonon frequency Ω, the phonon attenuation γ_{ph} and an amplitude scaling factor.

We first model the phonon contribution with the ISRS model (Eq. (9.10)). As can be seen in Fig. 9.5a, the ISRS model fails to fit our data because the coherent oscillations are phase-shifted by $\approx \pi/2$ compared to the prediction of the ISRS model. This phase shift shows that the ISRS model with its zero electronic memory is not capable of reproducing our experimental data. Therefore, we introduce memory effects by using the DECP model.

To account for an electronic memory of the DECP model, we set the electronic isotropization time equal to the measured Drude relaxation time, that is, $\tau_e = 75$ fs (see Appendix). Accordingly we calculate the corresponding DECP driving force (Eq. (9.11)) and plot the result in Fig. 9.5c-e in comparison to the ISRS force and the pump field. As can be seen from Fig. 9.5e, the relatively short electronic memory leads to a time shift of the force peak amplitude by ~ 100 fs with respect to the pump field E (Fig. 9.5c). In Fig. 9.5b, we find the DECP model reproduces well the phonon's phase in our data. The coherent oscillation can be fitted with $\Omega = 3.08$ THz and $\gamma_{\mathrm{ph}} = 1/(4.3\ \mathrm{ps})$.

These results demonstrate for the first time a displacive excitation of coherent phonons via a SF Raman excitation rather than a DF excitation.

9.7 Spatial localization

We now address the question which sample regions contribute how strongly to the measured dynamics. In principle, the signal can be generated over the entire bulk of the film, or it can be generated at inhomogeneities, that is, the front-surface and rear-interface of the film. Surface and rear-interface host the metallic TI surface states that were recently shown to significantly absorb THz radiation [VA12, Luo13]. However, a residual bulk conductivity may also significantly contribute to THz absorption in Bi_2Te_3. Strikingly, we show that we can use our thickness-dependent experimental data to separate the contributions of surface, rear-interface and bulk (see Fig. 9.6a).

Before we focus on the signal localization, it is instructive to recall our basic observations. The pump-induced signals in Fig. 9.1b feature two kinds of responses, a step-like electronic and an oscillatory lattice component. Remarkably, the fast electronic relaxation τ_1 (Table 9.1) as well as the phonon oscillation have a strong thickness dependence and appear only in the 13 nm sample. In the following, we show that we can understand this behavior by considering spatial details of the signal generation and detection.

The signal generation process is schematically shown in Fig. 9.6a. It can be described with the following equation:

$$\Delta E(\omega, 0^+) \propto \int \mathrm{d}z \Delta\epsilon(\omega, z) E_{\mathrm{probe}}(\omega, z) G_z(\omega, z, 0^+). \tag{9.16}$$

Here, $\Delta E(\omega)$ is the field component due to a pump-induced change $\Delta\epsilon$ of the dielectric function. $\Delta\epsilon$ causes additional scattering of the probe field E_{probe} resulting in a perpendicular field component $\Delta E(z)$ that induces an rotation and/or ellipticity of the probe

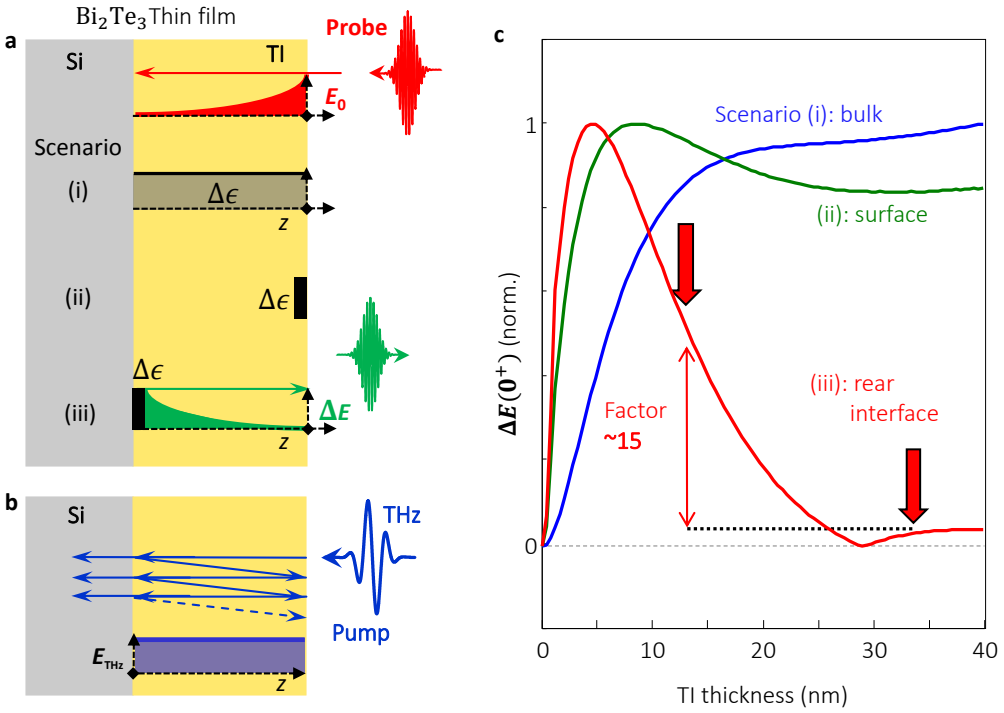

Figure 9.6: Signal generation and detection. **a** Probe pulses undergo a strong exponential decay. Therefore, is the probe field ($\Delta E(0^+)$ amplitude directly after the sample sensitive to the location of the source layer, as indicated for a pump induced $\Delta\epsilon$ located in regions (i), (ii) and (iii). **b**, The air-sample-substrate structure forms a Fabry-Pérot cavity for THz pump pulses. Since the THz attenuation length is much larger than the film thickness, the field density inside the sample is constant and independent on the sample thickness. **c**, Signal amplitude simulated for the three source layer scenarios indicated in **a**. For details on the simulation see Appendix.

field. All the microscopic fields $\Delta E(z)$ generated at each position z contributes to the macroscopic field $\Delta E_\Omega(0^+)$. Details of the propagation to $z = 0^+$, that is, z directly after the sample excite face, are accounted for by $G_z(z, 0^+)$, the plane wave's Green function. Both, incident probe field E_{probe} and $G_z(z, 0^+)$ decrease with thickness (see Appendix).

For a qualitative assignment, it is instructive to consider probe intensity profiles for three source-layer scenarios: (i) entire bulk, (ii) 1 nm surface layer at the air-sample-interface, and (iii) 1 nm layer at the Bi_2Te_3-Si-substrate interface (Fig. 9.6a). The strong probe attenuation causes a more efficient probing of the front surface than the rear-interface. Thus, a rear-interface signal decreases in the thicker sample (Fig. 9.6a). For example, if the signal comes from a 1 nm layer at the TI-substrate-interface, only, the short probe penetration depth of 12 nm Ref. [Mad98c] causes already a signal attenuation of $I(13\text{ nm})/I(34\text{ nm}) \approx 5$.

A quantitative calculation of the signal amplitude has to account for multiple reflections at the film interfaces (included in Eq. (9.16)) and also account for the THz pump field (for details see Appendix). Since the pump wavelength ($\sim 300\mu$m) is much larger than the film thickness, the pump field is homogeneous across the film (Fig. 9.6b), and the pump-induced change in the dielectric function $\Delta\epsilon$ is proportional to the deposited energy,

$$\Delta\epsilon(\Omega, z) \propto \int \mathrm{d}t E^2(z). \tag{9.17}$$

In the bulk, $\Delta\epsilon$ is constant, whereas it may be different at the interfaces. Therefore, we quantitatively model the signal amplitude for the scenarios (i)-(iii) by using Eq. (9.16) and Fig. 9.6a,b. Based on this modeling, we obtain the signal amplitude as a function of sample thickness that is characteristic for each of the individual scenarios (i)-(iii) (Fig. 9.6a).

Fig. 9.6c shows that the film thicknesses of 13 nm and 34 nm are perfectly suited to separate interface and bulk signal sources. For example, signals for scenarios (i) and (ii) do not change much in the range from 13 nm to 34 nm (Fig. 9.6b). In contrast, the signal for scenario (iii) varies significantly with thickness, and the signal amplitudes for the two samples differ by a factor of ~ 15. Fig. 9.6c and the significant thickness dependence of the signal strongly indicate that the oscillations and the electronic signal relaxing with τ_1 are located at the Bi_2Te_3-Si interface.

We note the only feature appearing for both sample thicknesses is the step-like response that relaxes with time constant τ_2 (Table 9.1). Consequently, we assign it to charge-carrier relaxation in the bulk. Since this feature appears in all measurements we normalize the amplitude of all data to its amplitude at $t = 6$ ps.

9.8 Comparison to Sb_2Te_3

Our measurements on Bi_2Te_3 and their analysis strongly indicate that SF Raman scattering (Fig. 9.3) drives the E_g^2 phonon at the TI/substarte interface via a displacive charge carrier excitation. To support our results on the phonon driving mechanism in Bi_2Te_3, we perform additional measurements on Sb_2Te_3 with a low p-type bulk conductivity.

9.8.1 Exclusion of other phonon driving mechanism

We have so far only considered electronically mediated forces acting on the lattice (e.g. DECP). However, a lattice mode can also be driven by anharmonic interaction with other phonon modes [For11] and its overtones [Bow16]. Further, Raman signals from tellurium rich sample regions of Bi_2Te_3 have been reported [Mis15]. To exclude these other possible phonon signal sources and check if our results are general, not restricted to Bi_2Te_3, we perform measurements on Sb_2Te_3 with a low p-type bulk conductivity.

In Fig. 9.7, we show measurements for a 15 nm and a 37 nm thick sample. We observe dynamics analogous to Bi_2Te_3: strong oscillations on an exponential background (Fig. 9.7). For 15 nm thick Sb_2Te_3, we observe a step-like response that relaxes double exponentially (Fig. 9.7a) and strong coherent oscillations at 3.34 THz which decay with a time constant of 1.6 ps. Importantly, the frequency of the oscillation coincides with the E_g^2 resonance of Sb_2Te_3 [Sha12].

The fact that in Bi_2Te_3 as well as in Sb_2Te_3 the oscillation frequency coincides with the E_g^2 resonance, respectively, strongly indicates that the signal originates from this mode

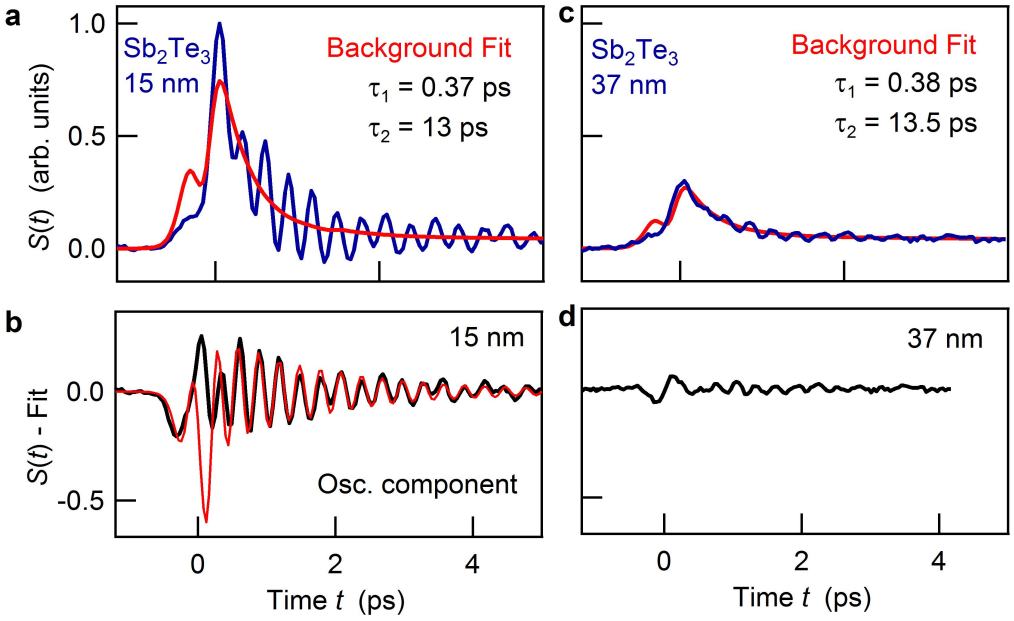

Figure 9.7: THz excitation (4 meV) of $\mathbf{Sb_2Te_3}$. **a**, Raw data and electronic background fit of a 15 nm Sb_2Te_3 sample upon THz excitation. **b**, Oscillatory component extracted from **a** and fit with the DECP model. **c**, Excitation of a 37 nm sample reveals an electronic response similar to **a**, but with the relative amplitude of the component relaxing with τ_1 reduced by a factor ~ 5. **d**, Oscillatory component from data in **c**. Compared to the 15 nm sample the oscillation amplitude is also reduced by a factor ~ 5.

driven by an electronically mediated forces.

9.8.2 Displacive excitation of coherent phonons in Sb_2Te_3

In Fig. 9.5, we have shown that fitting of the oscillatory signal components with Eq. (9.11) and Eq. (9.15) reveals the displacive excitation of the E_g^2 mode of Bi_2Te_3. Analogously, we fit the oscillatory component of Sb_2Te_3 based on the DECP model (Fig. 9.7b). As with Bi_2Te_3, the driving force generated by the pump-induced anisotropic electron distribution is assumed to decay with the Drude relaxation rate, which is 100 fs in Sb_2Te_3. We find reasonable agreement of data and fit (Fig. 9.7b) which shows that also in Sb_2Te_3 the driving force of the coherent phonon is of electronic origin.

When we excite a 37 nm sample, we observe an electronic decay similar to the 15 nm sample (Table 9.1), and also a small oscillatory component (Fig. 9.7c). Importantly, the contribution of the fast electronic response as well as the oscillations (Fig. 9.7d) in the 37 nm sample are reduced by a factor ~ 5. This thickness dependence is very similar to our observations in Bi_2Te_3 (Fig. 9.2). The by a factor of ~ 3 smaller amplitude difference is caused by the slightly larger penetration depth of 16 nm (calculated from Ref. [Mad98a]) in Sb_2Te_3.

These very similar results in n-type and p-type TI materials show that we can separate surface and bulk contributions in TIs, despite a residual bulk conductance.

Table 9.1: Electronic relaxation in Bi_2Te_3 and Sb_2Te_3 upon 4 meV excitation.

Sample	Bi_2Te_3 13 nm, $\Phi = 0°$	Bi_2Te_3 13 nm, $\Phi = 90°$	Bi_2Te_3 34 nm	Sb_2Te_3 15 nm	Sb_2Te_3 37 nm
τ_1 (ps)	0.4	0.9	-	0.37	0.38
τ_2 (ps)	8	7.7	6.5	13	13

9.9 Discussion

In summary, we have driven electron and phonon dynamics with photons sharing energies below the TI band gap. In this near-equilibrium excitation regime, we observed for the first time sum-frequency Raman excitation of coherent phonons in an opaque material. Further, we have shown that sample thickness variation on the order of the probe pulse penetration depth is very suitable to separate the response of the sample-substrate interface and bulk regions. With this technique we observe electron dynamics in Bi_2Te_3 and Sb_2Te_3 that is significantly faster at the rear-interface compared to relaxation in the bulk states. In the following will discuss the electron dynamics at rear-interface and bulk and possible sources of the electron displacement driving the coherent phonon at the rear-interface.

9.9.1 Electron dynamics

Table 9.1 shows the electronic relaxation times τ_1 (interface) and τ_2 (bulk) for all investigated samples. Remarkably, we observe only very slow relaxation of bulk electrons on a timescale of several picoseconds. To associate this timescale with a relaxation mechanism, it is instructive to first consider what is the excited state upon 4 meV excitation, and which scattering processes are possibly involved in the energy decay.

Electron excitation

Our excitation energy is 4 meV, which is significantly smaller than thermal energy ($k_BT \approx$ 25 meV). In this regime it was shown that intense THz radiation predominantly heats the electrons [Mic15], which can be described always with a Fermi-Dirac distribution. Due to the small number of interband transitions at 4 meV excitation, Drude-type intraband transitions significantly contributes to THz-pulse absorption [Kam05], consistently observed in THz transmission measurements in Bi_2Te_3 (see Appendix). Thermalization of the electron population may occur on a sub-100 fs timescale [Mic15]. Thus, ultrafast thermalization, much faster than the 1 ps timescale of the THz field oscillation (Fig. 9.1b), allows to consider the pump process as intraband heating of a Fermi-Dirac like electron distribution.

Electron relaxation

Upon excitation, the pump-induced thermal electrons can relax through electron-phonon and phonon-phonon coupling [Sun02]. Electron-phonon scattering in the surface states

and at the conduction band minimum is restricted to phonons close to the Γ point, which was similarly observed in graphite [Kam05]. The small size of the Fermi surface causes a maximum phonon wavevector of $q_{max} = 2k_F$ where k_F is the Fermi wavevector [Kam05]. Remarkably, we find electron-phonon relaxation to occur much faster at the rear-interface than in the bulk.

In the bulk, we observe a slow single exponential electronic decay (τ_2 Table 9.1), which indicates that electron-phonon scattering heats the Γ-phonons to thermal equillibrium with the electrons within the excitation pulse duration ($\ll$ 1 ps), and is therefore not resolved in the experiment. Consequently, we consider the pump to heat electrons and Γ-phonons in the bulk in thermal equilibrium. Subsequently, further energy relaxation is limited by phonon-phonon cooling to the cool phonon bath. Therefore, we assign τ_2 to the time constant of phonon-phonon scattering. Consistently, similar slow electron relaxation in the bulk conduction band has been observed upon optical excitation of p-type Bi_2Se_3 [Sob14].

On the surface, we find a much faster electronic decay (τ_1 Table 9.1), which we assign to electron-phonon coupling on the interface. Remarkably, we find no signature of quasi-steady filling of the surface state from an excited bulk population as it was observed upon optical excitation of Bi_2Se_3 [Sob12]. Since we only heat Fermi-Dirac electrons such filling effect would dominate already directly after excitation. Thus, we conclude that the observed relaxation time constants can be assigned to bulk and interface relaxation without significant interaction. The discrepancy between τ_1 detected in the 13 nm Bi_2Te_3 film for different sample orientations is likely caused by fast decay of the initial electronic anisotropy that contributes only for $\Phi = 0$, when also the oscillatory component is present.

9.9.2 Source of electron displacement

The short-lived anisotropic charge distribution is an interface charge current. Such current can be induce by intraband or interband transitions that either launch a rectified current by asymmetric intraband scattering in the TI-surface state proposed for THz-AC currents [Olb14] or drive, in principle, interband transitions between initial (interface) and final (bulk) states with a shifted center of charge distribution as observed for optical (1.5 eV) excitation of Bi_2Se_3 (see Chapter 7). At 4 meV a interband transitions can only occur, when the surface band approaches the conduction band. Since the transition energy between the linear interface state and the parabolic bulk bands depends strongly on the Fermi level further systematic tuning of the Fermi level has to reveal the role of interband transitions to the anisotropic charge distribution. However, both scenarios might be enhanced at the sample-substrate interface compared to the air-sample interface due to strain of the first film monolayers and step edges of the substrate, which both may increase the anisotropy, or suppression of the front surface state conductance by oxidation. Even though the high quality of our films [Kru11] reduces these perturbations to a minimum, transport measurements on similar TI thin films [Bac16] have revealed a surprising dominance of a single interface state, consistent with our observation.

9.9.3 Sum frequency DECP

Regardless of its origin, the anisotropic charge displacement drives a coherent phonon at the rear-interface of our thin films. Our anisotropic detection suppresses the A_{1g} modes and from the remaining E_g Raman modes we observe only the E_g^2 oscillating at 3.08 THz. We find that this phonon mode is coherently driven via sum-frequency Raman scattering, that is, the THz-pump-pulse deposits electromagnetic field energy at its sum frequency component into the electrons that causes a transient charge displacement driving the phonon. We emphasize that the new sum-frequency Raman excitation was only recently observed in Diamond and is here reported for an opaque material for the first time.

9.10 Conclusion/Outlook

Our experiment revealed insight into the poorly explored regime of near-equilibrium excitation and relaxation dynamics of electrons and phonons in TIs with ultrafast time resolution. We have found a new sum-frequency-excitation mechanism that can drive coherent phonons in opaque materials via the displacement of charges. We have further shown how THz-pump-optical probe experiments in combination with variation of the film thickness can access electron and lattice dynamics at a buried interface. We find that near-equilibrium electrons in the bulk and at the interface relax without significant interaction, in contrast to highly non-equilibrium electron populations [Sob12]. The found interface sensitivity is of fundamental importance for further studies on electron dynamics in bulk insulating and non insulating TIs, but has also the potential for fast and destruction free characterization of interface properties, for instance, in post-production investigation of interface sensitive devices.

Appendix Chapter 9

9.A TI dielectric function at THz frequencies

In order to measure the timescale of momentum relaxation in the Bi_2Te_3 bulk material we performed THz transmission spectroscopy on our thin film sample to obtain the dielectric function at THz frequencies. The principle idea of THz transmission spectroscopy is that a THz probe field is transmitted through a sample and changes in the waveform due to the dielectric response of the material are detected. Such THz transients after sample transmission are shown in Fig. 9.8a for a Si-substrate as reference sample and a sample with Bi_2Te_3 film. The THz field amplitude is attenuated in Bi_2Te_3 showing that THz radiation is absorbed. To extract the dielectric function we are interested on the field directly behind the sample $E(0^+)$. This field is related to the actual detected signal S by

$$S(\omega) = h(\omega)E(0^+,\omega) = h(\omega)R(\omega)E_{\mathrm{inc}}(0^+,\omega) \tag{9.18}$$

The function $h(\omega)$ describes the THz pulse propagation from the sample to the detector and the detector response function (details see Chapter **??**). The measurement of sample and reference than allows to cancel the spectrometer response and extract the desired sample response

$$\frac{E(0^+,\omega)}{E_{\mathrm{inc}}(0^+,\omega)} = t_{12}t_{23}M\exp(2\pi i\frac{\omega}{c}n_2 d) \tag{9.19}$$

Here, $M = 1/\left(1 - r_{21}r_{23}\exp\left(4\pi i\frac{\omega}{c}n_2 d\right)\right)$ accounts for multiple reflections inside the sample and the quantities $t_{ij} = 2n_i/(1+n_2)$ and $r_{\mathrm{ij}} = (n_i - n_j)\,/\,(n_i + n_j)$ are Fresnel transmission and reflection coefficients. $n_i = \sqrt{\epsilon_i}$ is the refractive index of medium i where $i = 1, 2, 3$ denotes air, Bi_2Te_3 and Si substrate, respectively.

We fit the extracted dielectric function in Fig. 9.8 with the Drude formula

$$\epsilon^{\mathrm{Drude}}(\omega) = 1 - \frac{\Omega_{\mathrm{pl}}^2}{\omega^2 + i\omega/\tau_e}. \tag{9.20}$$

The fit yields a screened plasma frequency $\Omega_{\mathrm{pl}} \approx 100$ THz and a drude relaxation time of $\tau_e = 75$ fs.

9.B Modeling of pump and probe propagation

To find the spatial localization of the pump-induced change in the dielectric function of the Bi_2Te_3 thin films it is essential to understand the details of pump and probe propagation The incident pump field E^{inc} induces a field $E(\omega, z)$ that we have to evaluate for all positions z along the pump propagation inside the sample

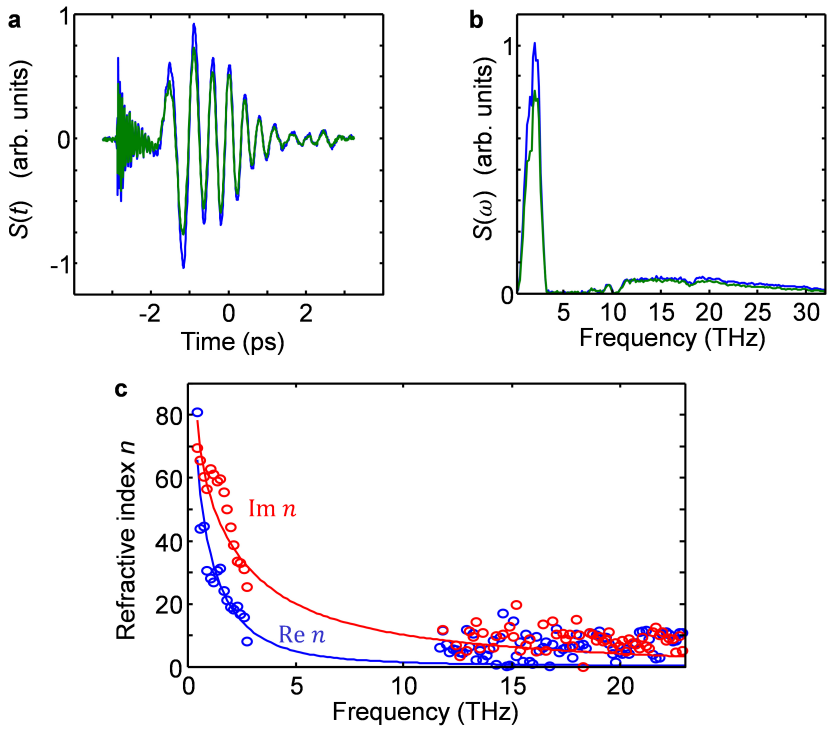

Figure 9.8: TI refractive index from THz transmission spectroscopy. **a**, Raw data of THz signals obtained after transmission through the Bi_2Te_3 sample and a Si-substarte as reference. **b**, Fourier transformed data of **a**. **c**, Refractive index (n) extracted from data in **b**. The line is the fit result to a Drude-type optical response.

$$E(\omega, z) = t_{12}(1 + r_{23})/(1 - r_{21}r_{23}) \cdot E^{\text{inc}}. \tag{9.21}$$

$E(\omega, z)$, is related to the incident field E^{inc} by the air-sample transmission $t_{12} = 2/(1+n_2)$ and multiple reflections inside the sample, associated with terms $r_{\text{ij}} = (n_i - n_j)\,/\,(n_i + n_j)$. The indeces $i = 1, 2, 3$ denote the media air, Bi_2Te_3 and Si substrate, respectively. This thin film formula is independent of the film thickness d, since $d/\lambda << 1$, which simplifies the more general multiple reflection term M used below in Eq. (9.24). Consequently, the total sample integrated signal increases linearly with the source layer thickness.

In contrast to the pump field, the probe field is sensitive to the sample thickness. The main reason is the short penetration depth of only 12 nm [Mad98c] . However, the large refractive index causes that also multiple reflections are not negligible. To include the full propagation and simulate the influence of different source layer as shown in Fig. 9.6, we model the whole probe process as follows. The probe field propagates through the sample and "feels" a pump induced change of the dielectric function, $\Delta\epsilon_\Omega$, causing a microscopic polarization $\Delta P = \Delta\epsilon_\Omega E_{\text{probe}}$. Along the probe path, all these microscopic polarizations at positions z induce a macroscopic field at $(z = 0^+)$ directly after the sample

$$\Delta E_\Omega(0^+, \omega) \propto \int \mathrm{d}z \Delta\epsilon_\Omega(z, \omega - \Omega) E_{\text{probe}}(z, d, \omega - \Omega) G_z(0^+, d, \omega). \tag{9.22}$$

Here, both the plane waves Green's function determined at the air sample interface (0^+)

$$G_z(0^+,\omega) = t_{21}M(\mathrm{e}^{ik_2 z} + r_{23}\mathrm{e}^{2ik_2 d - ik_2 z})/(2ik_2). \tag{9.23}$$

and the probe pulse

$$E_{\mathrm{probe}}(z,\omega) = t_{12}M(\mathrm{e}^{ik_2 z} + r_{23}\cdot \mathrm{e}^{2ik_2 d - ik_2 z})\cdot E_{\mathrm{inc}}(\omega) \tag{9.24}$$

depend on the sample thickness d; $M = 1/\left(1 - r_{21}r_{23}\exp\left(4\pi i\frac{\omega}{c}n_2 d\right)\right)$ accounts for multiple reflections. The thickness dependence of G_z and E_{probe} significantly modifies the linear factor between the interference signal S on the detector and $\Delta\epsilon_\Omega$. Most importantly, according to Eq. (9.22) S also depends on the source layer position ($\Delta\epsilon_\Omega(z_{\mathrm{source}}) \neq 0$) along z: $S(d, z_{\mathrm{source}}) \propto \Delta E(z_{\mathrm{det}}, d, z_{\mathrm{source}}, \omega+\Omega)E^*_{\mathrm{probe}}(z_{\mathrm{det}}, d, \omega)$.

10 Electron-phonon dynamics on the surface of $(Bi_xSb_{1-x})_2Te_3$

In this chapter, we replace the optical probe by a THz pulse, to probe more selectively electrons around the Fermi energy. Such THz-pump/THz-probe technique is used to drive and probe TI surface carriers with photon energies below the band gap (< 150 meV). We chose the system $(Bi_xSb_{1-x})_2Te_3$ as variation of x permits control over the Fermi-level alignment in these films. We find a strong dependence of the electron relaxation dynamics on the Fermi level. While in n-doped samples electron-phonon coupling in the bulk material dominates the excited state relaxation, we observe in p-type samples, and excitation across the Dirac point, strong indications for surface dominated electron-phonon relaxation. Remarkably, we find that upon excitation the phonons on the TI surface reach thermal equilibrium with the electrons within ~ 3 ps. Then, the small Fermi surface acts as a bottleneck that limits further cooling of the electrons by the lattice for times longer 400 ps.

10.1 Motivation

The surface of topological insulators hosts robust [Zha09] and highly mobile [Qi11] charge carriers that have a spin orientation locked to the propagation direction [Moo10]. The linear surface band dispersion of massless Dirac particles [Qi11] was shown in angle-resolved photoemission spectroscopy (ARPES, [Hsi09b]). However, the direct measurement of surface transport at roomtemperature remains challenging due to residual bulk conductance [Bar14, She14, Ait13].

To access the charge carrier dynamics, the relaxation of non-equilibrium carriers has been investigated with optical pump-probe techniques [Sob14, Wan12]. These studies have clarified the processes of thermalization and subsequent cooling of highly excited (~ 1 eV) surface and bulk states by emission of acoustic phonons [Wan12], and revealed a quasi-steady filling of the surface state from the bulk [Sob14]. Recently, low energy excitation pulses (~ 1 eV to $0.25 - 0.4$ eV) [Oni15, Kur16]) were used to reduce the excess energy of bulk electrons and, thus, their signal contribution. In this regime, Auger recombination reduces the surface-state filling from the bulk [Oni15], and surface state excitation by intercone transitions have been reported [Kur16]. So far, the in-gap (< 300 meV) transport properties, measured with probe energies as small as 4 meV (1 THz), have been investigated mainly upon excitation with optical photons and, thus, the surface electron dynamics were found to be strongly coupled to highly nonequilibrium bulk electrons [VA15, Sim14]. To exploit the full potential of probing with THz pulses and potentially reveal signatures of surface-carrier relaxation unperturbed by hot bulk electrons, pump and probe photon energies below the band gap are desired.

Here, we present a novel THz-pump/THz-probe technique to drive and probe TI sur-

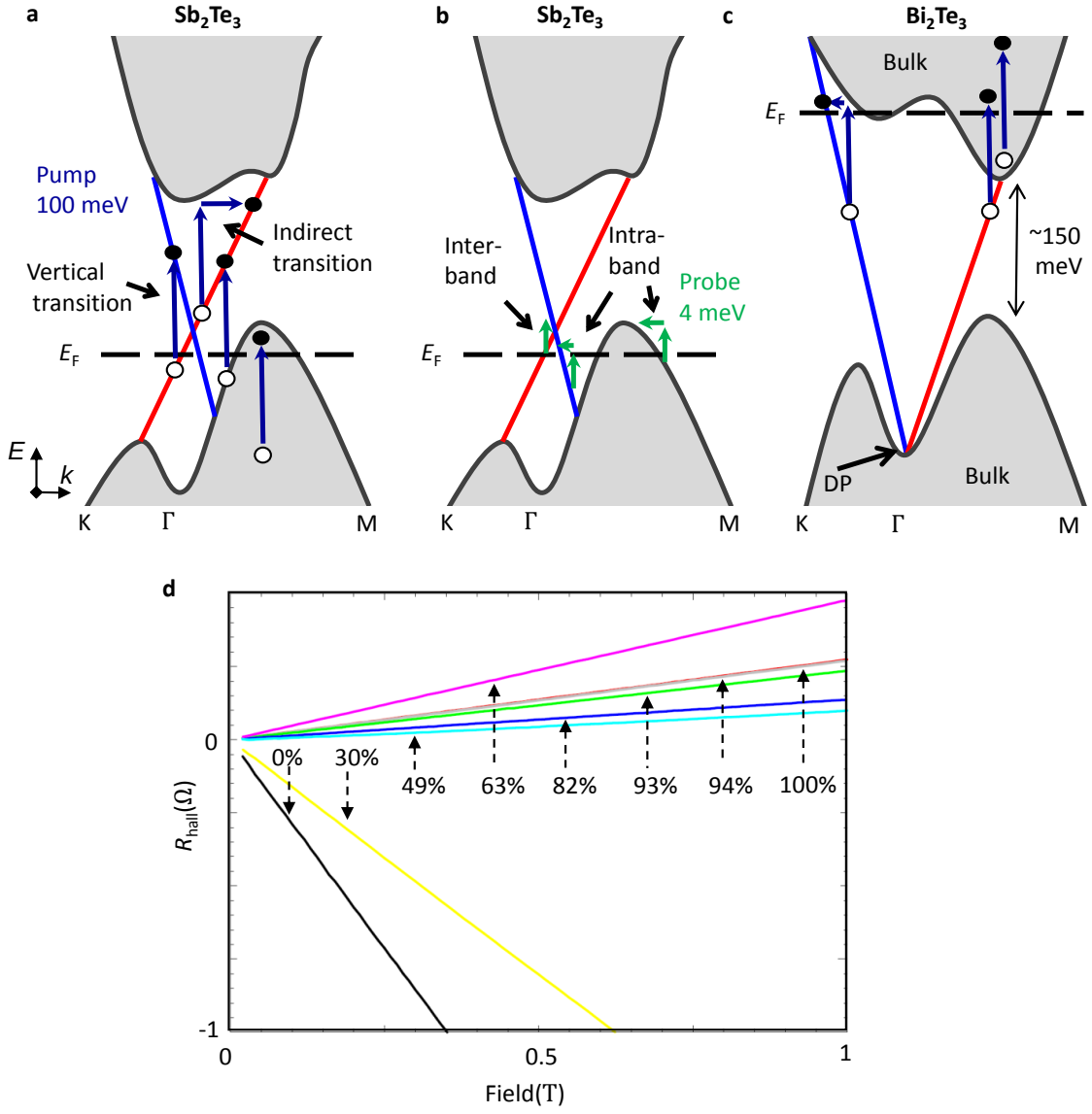

Figure 10.1: Suggested THz transitions involving the TI surface states. **a**, Schematic of the electronic band structure Sb_2Te_3 [Zha11] along with electronic transitions excited with sub-band gap photons (26 THz ≈ 100 meV). **b**, Possible optical transitions driven by the 1 THz (4 meV) probe pulse. **c**, Possible pump-transitions in Bi_2Te_3. **d**, Hall resistance of our $(Bi_xSb_{1-x})_2Te_3$ samples. Percentages indicate the substitution of Bi by Sb from n-doped Bi_2Te_3 (0%) to p-doped Sb_2Te_3 (100%).

face carriers with both pump and probe photon energies smaller than the band gap (< 300 meV). With this low pulse energy, we explore surface-carrier relaxation unperturbed by excited bulk states, that may assist energy relaxation of the surface by electron-electron scattering.

We use 26 THz (100 meV) pump and 1 THz probe pulses (4 meV), spectrally well separated to investigate the pump induced carrier dynamics. We chose the system $(Bi_xSb_{1-x})_2Te_3$ as sample because variation of x permits control over the Fermi-level alignment in these films [Zha11, Wey15, Kel15]. The low energy excitation below the band gap (~ 150 meV, Ref. [Hsi09b]) and the tuning of the Fermi level across the band gap is used to separate surface-electron dynamics from those of bulk electrons. We find a long-lived (> 400 ps) excited state, which we assign to reduced electron-phonon energy relaxation at the Dirac point. In contrast, we find strong indications that electron-phonon-coupling relaxes an excited bulk population within several picoseconds.

10.2 Experimental details

10.2.1 Sample characterization

Our samples are $(Bi_{1-x}Sb_x)Te_3$ (BST) thin films with a thickness of ~ 30 nm on a Si(111) substrate. Systematic substition of Bi by Sb tunes the Fermi level from n-type Bi_2Te_3 over $(Bi_{1-x}Sb_x)Te_3$ compounds with $x \in \{0.3, 0.43, 0.63, 0.82, 0.93\}$ to p-type Sb_2Te_3. A schematic of the band structure of Sb_2Te_3 is depicted in Fig. 10.1a. The indirect band gap is ~ 150 meV [Hsi09b] and the Fermi level is in the bulk valence band, ~ 50 meV below the Dirac point [Zha11].

Hall measurements confirm the p-type character of our Sb_2Te_3 sample ($x = 1$, Fig. 10.1d). Further, the Hall resistance decreases with decreasing x, indicating a monotonous upward shift of the Fermi level into the bulk band gap. The only exception of the monotonous resistance change is the $x = 0.63$ sample. For $x \leq 0.3$, n-type resistance indicates the Fermi level is located inside the conduction band (Fig. 10.1c). This is consistent with angle resolved photoemission (ARPES) data on similar samples to ours published in Ref. [Pla16]. For $x \geq 0.82$ ARPES data in Ref. [Wey15] confirm consistently with the p-type Hall resistance that the Fermi-level is located at the top of the bulk valence band within $\sim$ 100 meV of the Dirac point energy (Fig. 10.1a).

10.2.2 The THz-pump/THz-probe setup

The THz-pump/THz-probe experiment is depicted in Fig. 10.2a. Pump pulses with a central frequency of 26 THz and peak field of 10 MV/cm are generated via difference frequency mixing of 1200 nm and 1400 nm optical pulses in a 10 μm GaSe crystal. They are incident on the TI thin film samples. A timedelayed 1 THz pulse probes the pump-induced transmission change. The probe pulses are detected by electrooptic sampling in a 300 μm thick ZnTe crystal. Pump and probe beam are set to a relative angle of incidence

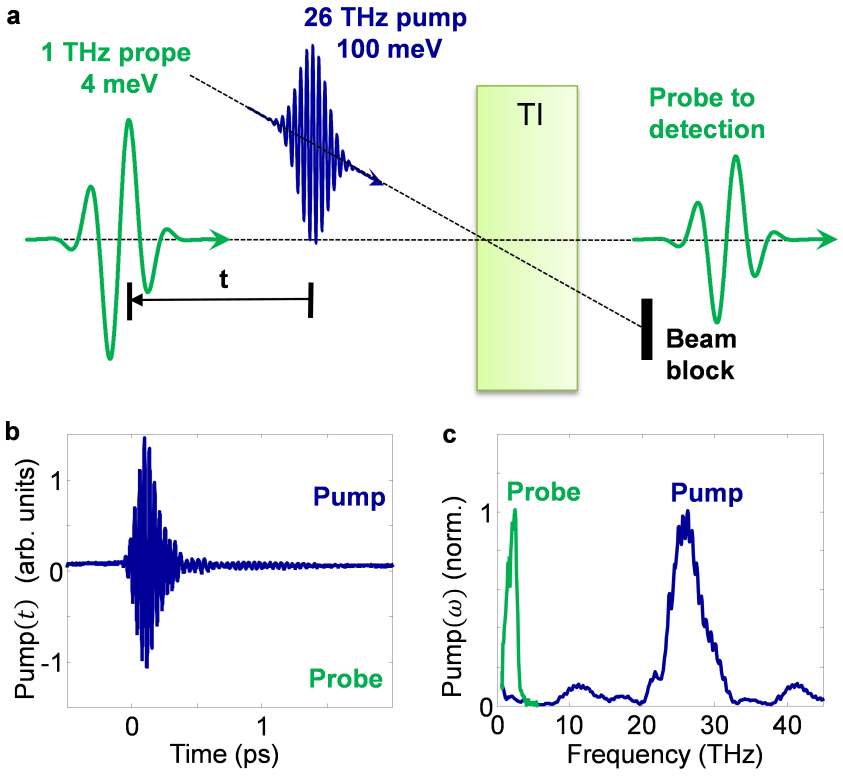

Figure 10.2: THz-pump-THz-probe measurement of charge carrier dynamics in TI compounds $(Bi_xSb_{1-x})_2Te_3$. **a**, An intense 100 meV pump field excites a TI sample. The excited state population is detected via the pump induced transmission change of a time delayed 4 meV probe field. **b**, Electric field transients of our pump and probe pulses. **c**, Fourier spectra of pump and probe pulses.

of $\sim 45°$ to spatially separate the pulses before the detection. Field transients and spectra of our THz pulses are shown in Fig. 10.2b,c.

10.3 Results

10.3.1 Pump-induced broadband THz transmission change at $t = 0$

In Fig. 10.3a we show spectra of our 1 THz probe pulses after transmission through Bi_2Te_3 ($x = 0$) with and without 26 THz pump illumination for maximum pump-probe overlap ($t = 0$). In the excited sample the THz-transmission is $\approx 20\%$ reduced, indicating pump enhanced probe absorption. In strong contrast, when we excite a BST sample with $x = 0.82$ (Fig. 10.3b), the excitation induces an enhanced probe transmission, indicating a bleaching of the sample.

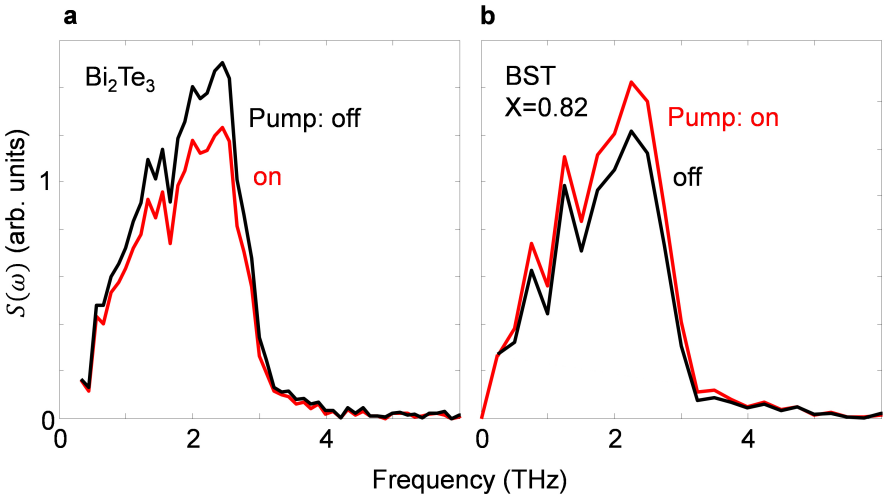

Figure 10.3: Pump induced THz absorption at 1 THz=4 meV. **a**, Excitation of Bi_2Te_3 with 100 meV pump pulses induces enhanced probe absorption indicating increased Drude (intraband) scattering. **b**, Excitation of BST x=0.82 increases probe transmission indicating blocked interband transitions due to an population inversion.

10.3.2 Signal dynamics

To further investigate the temporal dynamics of these remarkably different responses, we conducted measurements for different values of x. We find a very monotoneous behaviour as a function of x. In Fig. 10.4, we show spectrally integrated (0.3-3 THz) changes of the THz transmission upon excitation for various pump-probe delays. The bleaching signal observed for $x = 0.82$ (Fig. 10.3b) appears as positive peak in Fig. 10.4a and has two contributions: one that relaxes within ~ 3 ps, and a second that lives much longer than the longest available time window in our experiment (~ 400 ps, Fig. 10.4c for $x = 0.63$).

When the Fermi level decreases ($x = 0.93$ and $x = 1$), the bleaching feature remains dominant but the amplitude of the long-lived signal decreases in Sb_2Te_3 ($x = 1$). Note the second peak at $t \approx 17$ ps (Fig. 10.4a) is a echo of our pump pulse in the substrate and the time delay depends on the substrate thickness (0.7 mm). Sb_2Te_3 is the only sample grown on a thinner (0.5 mm) Si substrate and, consequently, the peak appears earlier in time ($t \approx 11$ ps,Fig. 10.4b).

When the Fermi level is increased ($x = 0.63$) suddenly the bleaching signal at $t = 0$ and $t > 20$ ps is accompanied by increased absorption ($t = 3$ ps). For $x = 0.3$, 0.43 and Bi_2Te_3 ($x = 0$) this absorption feature dominates the sample response with slowest relaxation time (≈ 7 ps) for BST 0.43.

Finally, we tune our pump pulse from 26 THz (100 meV) to 34 THz (≈ 140 meV). When exciting the $x = 0.63$ sample, the higher pump energy enhances the absorption feature (Fig. 10.4c).

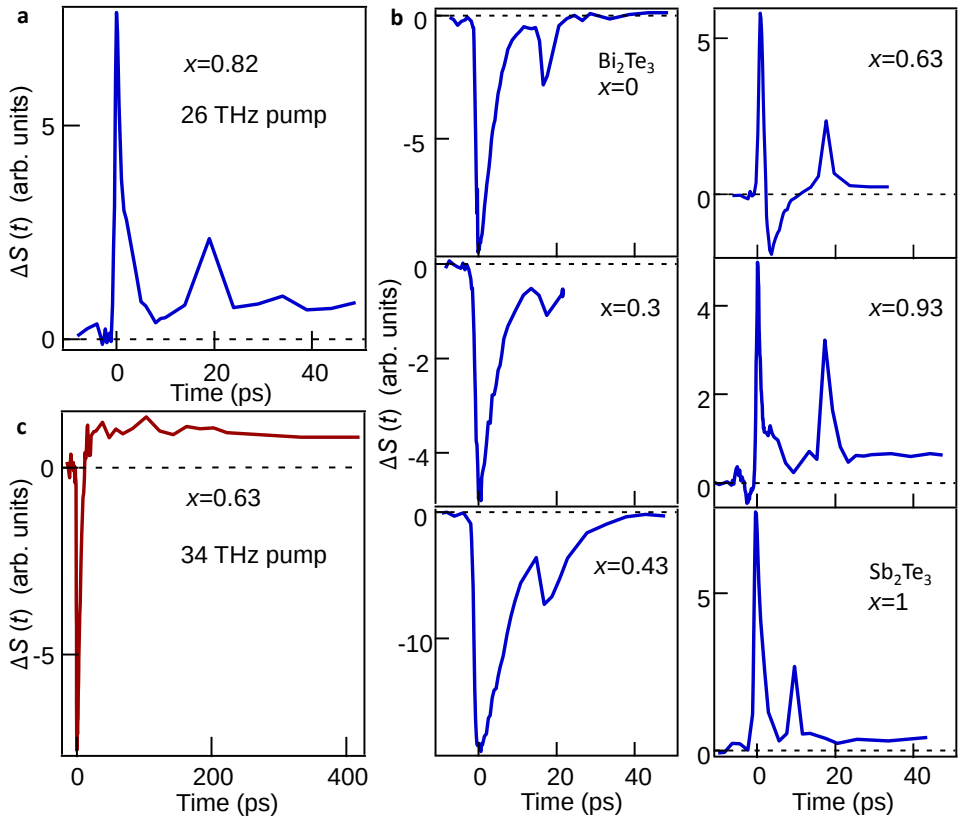

Figure 10.4: Dynamics of the TI transmittance at 1 THz (4 meV) following excitation with sub-band gap photons (26 THz ≈ 100 meV) of BST. **a**, Peak at time zero and step like feature indicate the enhanced probe transmission upon excitation of $(Bi_xSb_x)_2Te_3$ ($x = 0.92$). **b**, Variation of x from 0 to 1 corresponds to a gradual Fermi-level change from n-type to p type across the band gap. For $x < 0.63$ the THz pump induced probe transmission is reduced. In contrast, when $x > 0.63$, the probe transmission is enhanced. **c**, Increasing the pump energy from 26 THz to 34 THz (140 meV) enhances THz absorption in the $x = 0.63$ for $t < 5$ps, while for longer times the transmission is enhanced.

10.4 Discussion

We performed THz-pump-THz-probe measurements on topological insulators (BST) with the Fermi level tuned through the band gap across the Dirac point (Fig. 10.1). For n-type samples ($x \leq 0.3$), we observe a decrease of THz transmission upon excitation. In sharp contrast, for p-type samples ($x \geq 0.82$), the THz transmission increases. In the following, we suggest an explanation of these findings, which also provides a key to identify bulk and surface state dynamics.

10.4.1 Pump-induced bleaching

We first focus on the bleaching signal observed when $x \geq 0.82$. To understand the pump induced transmission enhancement we consider likely optical transitions between initial and final states. The initial state is approximately given by Hall resistance measurements (Fig. 10.1d), which imply the Fermi level localized inside the valence band for $x \geq 0.82$. ARPES data further shows that the Fermi level coincides with the Dirac point (DP) within 100 meV when $x \geq 0.82$) [Wey15, Kel15]. This consensus of the Fermi-level localized around the DP with the appearance of the bleaching signal motivates us to consider possible optical transition at the TI surface. At the DP, two sorts of transitions can absorb THz radiation, depicted in Fig. 10.1. A Bloch electron can either absorb a THz photon by a direct optical transition (DOT), which conserves the electron wave vector $\mathbf{k}$, or by an indirect optical transition (IOT). An indirect transition requires some additional wavevector $\mathbf{k}$ that can be provided by scattering with phonons, lattice defects, or other electrons.

The 100 meV pump pulses excite electrons into the top of the bulk valence band and into the surface states (Fig. 10.1a,c). The observed bleaching signal (Fig. 10.4a) indicates that the newly created electron-hole pairs block some of the originally possible DOTs in a range of $k_{\mathrm{B}}T$ around the Fermi energy E_{F} and, thus, the absorption of probe photons decreases. A similar effect was observed in Graphite [Kam05], where interband transitions significantly contribute to THz probe absorption. Pump-induced electron-hole pairs block this transition, thereby increasing the probe transmission. In the $x \geq 0.82$ TIs, such bleaching may occur at the DP and may block the DOT of the probe as depicted in Fig. 10.1b. Consistently, the bleaching signal (Fig. 10.4a) appears only in TI samples that have the DP close to the Fermi level[Wey15, Kel15]. Only these samples ($x \geq 0.82$) allow transitions across the DP that are found to reduce probe absorption.

One may wonder why such intercone transition across the DP between states with opposite spin are allowed, since spin-flip excitations are forbidden in the dipole approximation. However, this selection rule is softened if spin-orbit coupling reduces the spin polarization below 100%. Indeed, a spin polarization of below 80% has been discussed for the TSS in different 3D TIs[Yaz10] and Kuroda *et al.* reported similar intercone transitions in Sb_2Te_3.

10.4.2 Pump-induced absorption

When $x \leq 0.3$ the n-type doping (Fig. 10.1) causes the Fermi level to lie inside the bulk conduction band. As seen in Fig. 10.1c, such occupation of the initial state allows a large number of final states in the bulk conduction band. Accordingly, we assign the pump-induced absorption enhancement to hot bulk electrons in the conduction band. To support this hypothesis we focus on BST ($x = 0.63$), since this is the only sample that shows pump-induced absorption enhancement ($t = 3$ ps) but also bleaching ($t = 0$ and $t > 10$ ps). If the absorption feature is induced by occupation of the bulk band, the absorption is expected to increase when the pump energy increases from 100 meV to 140 meV, which is in the order of the indirect band gap ($\sim$ 150 meV) and, therefore, transitions across the band gap can contribute to the excited-state population. Indeed, Fig. 10.4c shows a significantly enhanced absorption feature for the higher pump photon energy compared to Fig. 10.4b.

Such THz absorbtion increase in metallic states occurs in many optical-pump/THz-probe experiments due to a broadened Fermi edge that causes increased Drude (intraband) absorption [Kam05]. Similarly, increased probe absorption is found for our $x = 0.43$ sample that has the Fermi level inside the gap. The similar response to the n-doped samples indicates that the Fermi level is less than 100 meV below the bulk conduction band (consitent with ARPES in Ref. [Pla16]). Therefore, surface-to-bulk transitions can populate the bulk conduction band and, thus, enhance Drude-type probe-absorption in the bulk conduction band.

10.4.3 Excited-state dynamics

Having assigned the spectroscopic signature of excited electrons at the DP and in the bulk, we can discuss their very different relaxation dynamics. While the absorption feature ($x \leq 0.3$) decays monoexponentially on a time scale of several picoseconds (Fig. 10.4b), the bleaching signal ($x \geq 0.82$) follows an initially fast (≈ 3 ps) decay but has also a slow component that persists for more than 400 ps (Fig. 10.4c).

Such long-lived signals indicate a strong relaxation bottleneck in samples with $x \geq 0.82$. Bottleneck features of electron relaxation have been observed in ARPES measurements [Sob12, Neu15, Haj14, SB16] and have been assigned to (i) a surface state filling from bulk states [Sob12], (ii) electron transport out of the probe volume inducing a long-lived transient shift of chemical potential [Neu15, Haj14] and (iii) a substantially reduced phase space for electron relaxation at the Dirac point [SB16].

To assign the bottleneck in BST (≥ 0.82), we can exclude (i) and (ii), since our pump pulse (i) has an energy smaller than the band gap, and (ii) excites the sample homogeneously over the entire film thickness. Therefore, our assignment of the bleaching signal to (iii) a blocking of THz optical transitions at the DP is consistent with Ref. [SB16].

Finally, we suggest implications of the observed relaxation dynamics. The pump-induced hot-carrier population quickly relaxes via carrier-carrier and carrier-phonon interactions to an isotropic thermal distribution ($\sim$ 1 ps, [Oni15]), which is then followed by energy transfer to the lattice [Mih16]. Owing to the small excitation energy $\sim$ 100 meV, the

emission of low-energy optical and acoustic phonons is the only efficient cooling pathway to the lattice. The double exponential decay of the bleaching signal indicates that phonons on the TI surface reach thermal equilibrium with the electrons within $\tau_1 \sim 3$ ps (Fig. 10.4). When thermalized, the small Fermi surface around the Dirac point appears as strong bottleneck, since scattering occurs only with a small number of phonons that have a wavevector smaller than $q_{\mathrm{max}} = 2k_{\mathrm{F}}$ where k_{F} is the Fermi wavevector [Kam05]. Pauli blocking than causes the excited surface state to persist for times $\tau_2 > 400$ ps (Fig. 10.4c).

While on the surface, the Γ-phonons are quickly heated to thermal equilibrium with the electrons, which blocks the excited state population, in the bulk the larger set of available phonons can relax the excited state within picoseconds (Fig. 10.4b). When x increases, the relaxation time increases from 5 ps ($x = 0$) to 7 ps ($x = 0.43$). This fact shows the decrease of the excited state Fermi surface, when approaching the conduction band minimum, similar to the reduced cooling at the DP.

10.5 Conclusion/Outlook

We have performed first pump probe measurements on topological insulators with pump and probe photons sharing energies below the band gap. Our results show signatures of bulk and surface electron dynamics with a contribution strength that strongly depends on the Fermi-level position with respect to the Dirac point and the conduction-band minimum. We find that the small Fermi surface around the Dirac point is a strong bottleneck for electron-phonon relaxation. This assignment is consistent with optical pump experiments Ref. [SB16]. However, an extremely long lifetime of the excited state population at the DP for $\tau_2 > 400$ ps is reported here for the first time. Such long excited-state population suggests that at excitation energies smaller than the band gap, the excited surface state in BST ($x \geq 0.82$) is strongly decoupled from the bulk even under ambient conditions.

Detailed studies of the frequency dependence of THz absorption are underway and will reveal further insight into the mobility of the involved charge carriers, which is beyond the scope of this proof of principle study. Further investigation has to show if the extreme lifetime of the excited state population can be exploited for long-lived currents and spin polarizations.

11 Summary

The work presented in this thesis investigates ultrafast charge carrier and lattice dynamics of topological insulators by employing complementary time-resolved techniques. To explore the ultimate speed limits of charge transport, photocurrents are launched with femtosecond (fs) optical pulses that create a highly non-equilibrium electron distribution. While optical pulses induce highly excited electrons ($\hbar\omega >$ band gap $> k_{\mathrm{B}}T$), gentle perturbation of the system is possible with THz electric fields having photon energies well below the thermal energy ($\hbar\omega < k_{\mathrm{B}}T <$ band gap). Thus, physically two complementary regimes of non-equilibrium and near-equilibrium carrier interactions are addressed. Note low energy photons offer the possibility to study the underexplored regime of ultrafast energy relaxation of electrons under conditions met in electronic devices.

In Chapter 7, we explored the capability of Bi_2Se_3 surface currents for THz opto-spintronics. Photocurrents are launched by 20 fs optical laser pulses and measured by detecting the concomitantly emitted terahertz (THz) electromagnetic radiation. The mechanisms underlying the photocurrents are identified based on their temporal structure and their dependence on surface modification. For the first time, we have observed a surface shift photocurrent which arises from a charge displacement at the topological insulator surface. The fast decay time (22 fs) of this current reflects the rapid loss of the optically induced anisotropic surface electron distribution. Such a fast anisotropy decay indicates that electron-electron scattering is the dominant relaxation mechanism [Sun02]. Due to spin-momentum locking, the spin relaxation must proceed on the same time scale. Interestingly, pump-helicity-dependent currents are orders of magnitude smaller than expected from the photocurrent generation scenario based on asymmetric depopulation of the Dirac cone [McI12b]. This remarkable result suggests a strong mutual cancelation of the contributions of the various optical transitions, much reduced matrix elements for surface-to-bulk transitions and/or relatively small pump-induced changes in the electron band velocity. Our results highlight broadband THz emission spectroscopy as a novel and highly sensitive probe of surfaces.

On a more applied note, we were able to demonstrate a sizeable spin-to-charge current conversion at THz frequencies, which shows that topological insulators are of direct relevance for broadband optoelectronic devices.

To study the poorly explored regime of near-equilibrium carrier dynamics and electron-phonon interactions at the surface and in the bulk of Bi_2Te_3 and Sb_2Te_3 (Chapter 9), we reduced the pump photon energy from 1.5 eV (optical) to 4 meV (THz). Since this photon energy is significantly smaller than the characteristic thermal energy (25 meV at room temperature), the excited electrons remain in a Fermi-Dirac distribution. The pump-induced changes of the dielectric function were detected with optical probe pulses. Separation of surface and bulk signals was achieved by modeling of the optical probe process in the samples as a function of film thickness. Remarkably, our results strongly suggest that near-equilibrium electrons in the topological-insulator bulk and at the topological-insulator/substrate interface relax independently of each other. This observation is in

contrast to highly non-equilibrium electron populations, for which a population transfer from bulk to surface states was reported [Sob12].

To further investigate carrier dynamics at the TI surface and in the bulk and to only probe charge carriers near the Fermi energy, the optical probe was replaced by a THz-probe pulse (Chapter 10). To spectrally separate pump and probe pulses, the pump photon energy was increased to 100 meV. This higher photon energy had the additional benefit to more easily drive intercone transitions across the Dirac point. Dynamics of electrons close to the Dirac point were revealed by studying differently doped samples of $(Bi_xSb_{1-x})_2Te_3$ in which the Fermi energy monotonously descents from the conduction band (n-type) to the valence band (p-type). Depending on the Fermi-level position, the pump induced an increase or decrease of the THz conductance. These signals were used to assign electron-phonon dynamics to bulk and surface contributions. Remarkably, the lifetime of the excited-state population depends strongly on the Fermi-level position, which culminates in an extremely long-lived excited state ($>$ 400 ps) in p-type topological insulators. We interpret this observation as a Dirac point bottleneck for electron-phonon relaxation, consistent with optical-pump experiments [SB16]. However, an extremely long lifetime of the excited state population is reported here for the first time.

The results of the THz probe measurements suggest that the often-observed coupling of optically excited bulk and surface state electrons [Wan12, Sob14] is strongly reduced for near-equilibrium carriers in p-type topological insulators. Detailed studies of the frequency dependence of THz absorption are underway and will reveal the mobility of the involved charge carriers. For fundamental and applied reasons, such studies are highly relevant for the discussion of the often-observed bulk dominance in transport measurements at room temperature [Bar14].

Besides these insights into the surface electron dynamics of topological insulators, Chapter 9 is another remarkable result. A THz-pump-induced electronic anisotropy was found to drive a coherent phonon at the topological-insulator/substrate interface by displacement of charges. Note that the force on the phonon is a result of a sum-frequency rather than difference-frequency process as usually observed for optical excitation.

Finally, we emphasize that the surface sensitivity of THz-emission and THz-pump optical/probe spectroscopy demonstrated here, is of fundamental importance for further studies on electron dynamics in bulk-insulating and surface-conducting topological insulators.

Bibliography

[Ahm14] S. Ahmed, J. Savolainen, & P. Hamm. *The effect of the Gouy phase in optical-pump-THz-probe spectroscopy.* Opt. Express **22**, 4, (2014) 4256.

[Ait13] M. Aitani, Y. Sakamoto, T. Hirahara, M. Yamada, H. Miyazaki, M. Matsunami, S. ichi Kimura, & S. Hasegawa. *Fermi-Level Tuning of Topological Insulator Thin Films.* Japanese Journal of Applied Physics **52**, 11R, (2013) 110112.

[Ale16] A. Alekhin, I. Razdolski, N. Ilin, J. P. Meyburg, D. Diesing, V. Roddatis, I. Rungger, M. Stamenova, S. Sanvito, U. Bovensiepen, *et al. Generation of femtosecond spin current pulses via non-thermal spin-dependent Seebeck effect and their interaction with ferromagnets in spin valves.* arXiv preprint arXiv:1606.03614 .

[Apo14] V. Apostolopoulos & M. Barnes. *THz emitters based on the photo-Dember effect.* J. Phys. D: Appl. Phys. **47**, 37, (2014) 374002.

[Arm09] M. R. Armstrong, E. J. Reed, K.-Y. Kim, J. H. Glownia, W. M. Howard, E. L. Piner, & J. C. Roberts. *Observation of terahertz radiation coherently generated by acoustic waves.* Nat Phys **5**, 4, (2009) 285.

[Ash76] N. W. Ashcroft & N. D. Mermin. *Solid state physics.* Saunders College, Philadelphia 120.

[Bac16] D. Backes, R. Mansell, M. Lanius, J. Kampmeier, D. A. Ritchie, G. Mussler, D. Gruetzmacher, & V. Narayan. *Disentangling surface and bulk transport in topological insulator p-n junctions.* ArXiv e-prints .

[Bak98] H. J. Bakker, G. C. Cho, H. Kurz, Q. Wu, & X.-C. Zhang. *Distortion of terahertz pulses in electro-optic sampling.* J. Opt. Soc. Am. B **15**, 6, (1998) 1795.

[Ban12] N. Bansal, Y. S. Kim, M. Brahlek, E. Edrey, & S. Oh. *Thickness-Independent Transport Channels in Topological Insulator* Bi_2Se_3 *Thin Films.* Phys. Rev. Lett. **109**, 11, (2012) 116804.

[Bar14] L. Barreto, L. Kúhnemund, F. Edler, C. Tegenkamp, J. Mi, M. Bremholm, B. B. Iversen, C. Frydendahl, M. Bianchi, & P. Hofmann. *Surface-Dominated Transport on a Bulk Topological Insulator.* Nano Lett. **14**, 7, (2014) 3755.

[Bas15] D. A. Bas, K. Vargas-Velez, S. Babakiray, T. A. Johnson, P. Borisov, T. D. Stanescu, D. Lederman, & A. D. Bristow. *Coherent control of injection currents in high-quality films of* Bi_2Se_3. Appl. Phys. Lett. **106**, 4, (2015) 041109.

[Bea02] M. C. Beard, G. M. Turner, & C. A. Schmuttenmaer. *Measuring Intramolecular*

Charge Transfer via Coherent Generation of THz Radiation. J. Phys. Chem. A **106**, 6, (2002) 878.

[Bel80] V. I. Belinicher & B. I. Sturman. *The photogalvanic effect in media lacking a center of symmetry.* Sov. Phys. Usp. **23**, 3, (1980) 199.

[Ber89] Y. Berozashvili, S. Machavariani, A. Natsvlishvili, & A. Chirakadze. *Dispersion of the linear electro-optic coefficients and the non-linear susceptibility in GaP.* J. Phys. D: Appl. Phys. **22**, 5, (1989) 682.

[Ber06] B. A. Bernevig, T. L. Hughes, & S.-C. Zhang. *Quantum Spin Hall Effect and Topological Phase Transition in HgTe Quantum Wells.* Science **314**, 5806, (2006) 1757.

[Blo29] F. Bloch. *Über die Quantenmechanik der Elektronen in Kristallgittern.* Zeitschrift für Physik **52**, 7, (1929) 555.

[Bos15] F. Boschini, M. Mansurova, G. Mussler, J. Kampmeier, D. Grützmacher, L. Braun, F. Katmis, J. S. Moodera, C. Dallera, E. Carpene, C. Franz, M. Czerner, C. Heiliger, T. Kampfrath, & M. Münzenberg. *Coherent ultrafast spin-dynamics probed in three dimensional topological insulators.* Sci. Rep. **5**, (2015) 15304.

[Bow16] P. R. Bowlan, J. Bowlan, S. Trugman, R. Valdes-Aguilar, J. Qi, X. Liu, J. Furdyna, A. Taylor, D. Yarotski, & R. P. Prasankumar. *Nonlinear phonon dynamics in Bi2Se3 driven by intense THz pulses and probed with optical second harmonic generation.* In *Conference on Lasers and Electro-Optics*. Optical Society of America, 2016 .

[Boy03] R. W. Boyd. *Nonlinear optics.* Academic press, 2003.

[Bra16] L. Braun, G. Mussler, A. Hruban, M. Konczykowski, T. Schumann, M. Wolf, M. Münzenberg, L. Perfetti, & T. Kampfrath. *Ultrafast photocurrents at the surface of the three-dimensional topological insulator* Bi_2Se_3. Nature Communications **7**, (2016) 13259.

[Bru10a] G. Brumfiel. *Topological insulators: Star material.* Nature News **466**, 7304, (2010) 310.

[Bru10b] C. Brune, A. Roth, E. G. Novik, M. Konig, H. Buhmann, E. M. Hankiewicz, W. Hanke, J. Sinova, & L. W. Molenkamp. *Evidence for the ballistic intrinsic spin Hall effect in HgTe nanostructures.* Nat Phys **6**, 6, (2010) 448.

[Bud98] E. Budiarto, N.-W. Pu, S. Jeong, & J. Bokor. *Near-field propagation of terahertz pulses from a large-aperture antenna.* Opt. Lett. **23**, 3, (1998) 213.

[CÔ3] D. Côté, J. E. Sipe, & H. M. van Driel. *Simple method for calculating the propagation of terahertz radiation in experimental geometries.* J. Opt. Soc. Am. B **20**, 6, (2003) 1374.

[Cab11] J. L. Cabellos, B. S. Mendoza, & A. I. Shkrebtii. *Optical coherent current control at surfaces: Theory of injection current.* Phys. Rev. B **84**, 19, (2011) 195326.

[Côt02] D. Côté, N. Laman, & H. Van Driel. *Rectification and shift currents in GaAs.* Appl. Phys. Lett. **80**, 6, (2002) 905.

[Czy04] G. Czycholl. *Theoretische Festkörperphysik.* In *Springer-Lehrbuch.* Springer, 2004 .

[dA11] J. A. del Alamo. *Nanometre-scale electronics with III-V compound semiconductors.* Nature **479**, 7373, (2011) 317.

[Dha94] L. Dhar, J. A. Rogers, & K. A. Nelson. *Time-resolved vibrational spectroscopy in the impulsive limit.* Chemical Reviews **94**, 1, (1994) 157.

[Die12] D. Dietze, K. Unterrainer, & J. Darmo. *Dynamically phase-matched terahertz generation.* Opt. Lett. **37**, 6, (2012) 1047.

[Dru00] P. Drude. *Zur elektronentheorie der metalle.* Annalen der Physik **306**, 3, (1900) 566.

[Dua14] J. Duan, N. Tang, X. He, Y. Yan, S. Zhang, X. Qin, X. Wang, X. Yang, F. Xu, Y. Chen, W. Ge, & B. Shen. *Identification of Helicity-Dependent Photocurrents from Topological Surface States in* Bi_2Se_3 *Gated by Ionic Liquid.* Sci. Rep. **4**.

[Erh15] N. Erhard, S. Zenger, S. Morkötter, D. Rudolph, M. Weiss, H. J. Krenner, H. Karl, G. Abstreiter, J. J. Finley, G. Koblmüller, & A. W. Holleitner. *Ultrafast Photodetection in the Quantum Wells of Single AlGaAs/GaAs-Based Nanowires.* Nano Lett. **15**, 10, (2015) 6869.

[Fau66] W. L. Faust & C. H. Henry. *Mixing of Visible and Near-Resonance Infrared Light in GaP.* Phys. Rev. Lett. **17**, 25, (1966) 1265. PRL.

[Fau04] J. Faure, J. Van Tilborg, R. A. Kaindl, & W. P. Leemans. *Modelling Laser-Based Table-Top THz Sources: Optical Rectification, Propagation and Electro-Optic Sampling.* Optical and Quantum Electronics **36**, 8, (2004) 681.

[Fer02a] B. Ferguson & X.-C. Zhang. *Materials for terahertz science and technology.* Nat. Mater. **1**, 1, (2002) 26.

[Fer02b] M. E. Fermann, A. Galvanauskas, & G. Sucha. *Ultrafast lasers: Technology and applications*, Bd. 80. CRC Press, 2002.

[Fio14] G. Fiori, F. Bonaccorso, G. Iannaccone, T. Palacios, D. Neumaier, A. Seabaugh, S. K. Banerjee, & L. Colombo. *Electronics based on two-dimensional materials.* Nat Nano **9**, 10, (2014) 768.

[For11] M. Forst, C. Manzoni, S. Kaiser, Y. Tomioka, Y. Tokura, R. Merlin, & A. Cavalleri. *Nonlinear phononics as an ultrafast route to lattice control.* Nat Phys **7**, 11, (2011) 854.

[Fu06] L. Fu & C. L. Kane. *Time reversal polarization and a Z_2 adiabatic spin pump.* Phys. Rev. B **74**, (2006) 195312.

[Fu07] L. Fu, C. L. Kane, & E. J. Mele. *Topological Insulators in Three Dimensions.* Phys. Rev. Lett. **98**, 10, (2007) 106803.

[Gal99] G. Gallot & D. Grischkowsky. *Electro-optic detection of terahertz radiation.* J. Opt. Soc. Am. B **16**, 8, (1999) 1204.

[Gan03a] S. D. Ganichev, V. V. Bel'kov, P. Schneider, E. L. Ivchenko, S. A. Tarasenko, W. Wegscheider, D. Weiss, D. Schuh, E. V. Beregulin, & W. Prettl. *Resonant inversion of the circular photogalvanic effect in n-doped quantum wells.* Phys. Rev. B **68**, (2003) 035319.

[Gan03b] S. D. Ganichev & W. Prettl. *Spin photocurrents in quantum wells.* Journal of Physics: Condensed Matter **15**, 20, (2003) R935.

[Gla74] A. M. Glass, D. von der Linde, & T. J. Negran. *High-voltage bulk photovoltaic effect and the photorefractive process in* $LiNbO_3$. Appl. Phys. Lett. **25**, 4, (1974) 233.

[Gla14] M. Glazov & S. Ganichev. *High frequency electric field induced nonlinear effects in graphene.* Phys. Rep. **535**, 3, (2014) 101.

[Gne11] V. Gnezdilov, Y. G. Pashkevich, H. Berger, E. Pomjakushina, K. Conder, & P. Lemmens. *Helical fluctuations in the Raman response of the topological insulator* Bi_2Se_3. Phys. Rev. B **84**, 19, (2011) 195118.

[Gro08] G. I. Groma, J. Hebling, I. Z. Kozma, G. Váró, J. Hauer, J. Kuhl, & E. Riedle. *Terahertz radiation from bacteriorhodopsin reveals correlated primary electron and proton transfer processes.* Proceedings of the National Academy of Sciences **105**, 19, (2008) 6888.

[Haj14] M. Hajlaoui, E. Papalazarou, J. Mauchain, L. Perfetti, A. Taleb-Ibrahimi, F. Navarin, M. Monteverde, P. Auban-Senzier, C. Pasquier, N. Moisan, D. Boschetto, M. Neupane, M. Hasan, T. Durakiewicz, Z. Jiang, Y. Xu, I. Miotkowski, Y. Chen, S. Jia, H. Ji, R. Cava, & M. Marsi. *Tuning a Schottky*

barrier in a photoexcited topological insulator with transient Dirac cone electron-hole asymmetry. Nature Communications **5**, (2014) 3003.

[Han02] P. C. Hansen. *Deconvolution and Regularization with Toeplitz Matrices.* Numerical Algorithms **29**, 4, (2002) 323.

[Has10] M. Z. Hasan & C. L. Kane. *Colloquium : Topological insulators.* Rev. Mod. Phys. **82**, 4, (2010) 3045.

[Has11] M. Z. Hasan & J. E. Moore. *Three-Dimensional Topological Insulators.* Annual Review of Condensed Matter Physics **2**, 1, (2011) 55.

[Heb02] J. Hebling, G. Almási, I. Z. Kozma, & J. Kuhl. *Velocity matching by pulse front tilting for large-area THz-pulse generation.* Opt. Express **10**, 21, (2002) 1161.

[Hel91] T. Held, T. Kuhn, & G. Mahler. *Influence of internal electric fields and surface charges on the transport of an optically generated electron-hole plasma.* Phys. Rev. B **44**, (1991) 12873.

[Hen04] E. Hendry, M. Koeberg, J. M. Schins, L. D. A. Siebbeles, & M. Bonn. *Ultrafast charge generation in a semiconducting polymer studied with* THz *emission spectroscopy.* Phys. Rev. B **70**, (2004) 033202.

[Hen06] E. Hendry, M. Koeberg, B. O'Regan, & M. Bonn. *Local Field Effects on Electron Transport in Nanostructured TiO2 Revealed by Terahertz Spectroscopy.* Nano Lett. **6**, 4, (2006) 755.

[Hér06] J. B. Héroux, Y. Ino, M. Kuwata-Gonokami, Y. Hashimoto, & S. Katsumoto. *Terahertz radiation emission from GaMnAs.* Applied Physics Letters **88**, 22.

[Hir11] H. Hirori, A. Doi, F. Blanchard, & K. Tanaka. *Single-cycle terahertz pulses with amplitudes exceeding 1 MV/cm generated by optical rectification in LiNbO3.* Applied Physics Letters **98**, 9.

[Hoe14] K. Hoefer, C. Becker, D. Rata, J. Swanson, P. Thalmeier, & L. H. Tjeng. *Intrinsic conduction through topological surface states of insulating Bi2Te3 epitaxial thin films.* Proceedings of the National Academy of Sciences **111**, 42, (2014) 14979.

[Hos11] P. Hosur. *Circular photogalvanic effect on topological insulator surfaces: Berry-curvature-dependent response.* Phys. Rev. B **83**, (2011) 035309.

[Hru11] A. Hruban, A. Materna, W. Dalecki, G. Strzelecka, M. Piersa, E. Jurkiewicz-Wegner, R. Diduszko, M. Romaniec, & W. Orłowski. *Influence of chemical composition of liquid phase and growth process on physical properties of* Bi_2Se_3*,* Bi_2Te_3 *and* Bi_2Te_2Se *compounds.* Acta. Phys. Pol. A **120**, 5, (2011) 950.

[Hsi09a] D. Hsieh, Y. Xia, D. Qian, L. Wray, J. H. Dil, F. Meier, J. Osterwalder, L. Patthey, J. G. Checkelsky, N. P. Ong, A. V. Fedorov, H. Lin, A. Bansil, D. Grauer, Y. S. Hor, R. J. Cava, & M. Z. Hasan. *A tunable topological insulator in the spin helical Dirac transport regime.* Nature **460**, 7259, (2009) 1101.

[Hsi09b] D. Hsieh, Y. Xia, D. Qian, L. Wray, F. Meier, J. H. Dil, J. Osterwalder, L. Patthey, A. V. Fedorov, H. Lin, A. Bansil, D. Grauer, Y. S. Hor, R. J. Cava, & M. Z. Hasan. *Observation of Time-Reversal-Protected Single-Dirac-Cone Topological-Insulator States in* Bi_2Te_3 *and* Sb_2Te_3. Phys. Rev. Lett. **103**, (2009) 146401.

[Hub00] R. Huber, A. Brodschelm, F. Tauser, & A. Leitenstorfer. *Generation and field-resolved detection of femtosecond electromagnetic pulses tunable up to 41 THz.* Applied Physics Letters **76**, 22, (2000) 3191.

[Jac06] J. D. Jackson. *Klassische Elektrodynamik.* Walter de Gruyter, 2006.

[Joh02] M. B. Johnston, D. M. Whittaker, A. Corchia, A. G. Davies, & E. H. Linfield. *Simulation of terahertz generation at semiconductor surfaces.* Phys. Rev. B **65**, 16, (2002) 165301.

[Jun13] A. Junck, G. Refael, & F. von Oppen. *Photocurrent response of topological insulator surface states.* Phys. Rev. B **88**, 7, (2013) 075144.

[Kam05] T. Kampfrath, L. Perfetti, F. Schapper, C. Frischkorn, & M. Wolf. *Strongly Coupled Optical Phonons in the Ultrafast Dynamics of the Electronic Energy and Current Relaxation in Graphite.* Phys. Rev. Lett. **95**, (2005) 187403.

[Kam07] T. Kampfrath, J. Nötzold, & M. Wolf. *Sampling of broadband terahertz pulses with thick electro-optic crystals.* Appl. Phys. Lett. **90**, 23, (2007) 231113.

[Kam09] T. Kampfrath, D. M. Beggs, T. F. Krauss, & L. K. Kuipers. *Complete response characterization of ultrafast linear photonic devices.* Optics letters **34**, 21, (2009) 3418.

[Kam13a] T. Kampfrath, M. Battiato, P. Maldonado, G. Eilers, J. Nötzold, S. Mährlein, V. Zbarsky, F. Freimuth, Y. Mokrousov, M. Blügel, Sand Wolf, R. I, P. M. Oppeneer, & M. Münzenberg. *Terahertz spin current pulses controlled by magnetic heterostructures.* Nat. Nanotechnol. **8**, 4, (2013) 256.

[Kam13b] T. Kampfrath, K. Tanaka, & K. A. Nelson. *Resonant and nonresonant control over matter and light by intense terahertz transients.* Nat Photon **7**, 9, (2013) 680.

[Kan11] N. Kanda, T. Higuchi, H. Shimizu, K. Konishi, K. Yoshioka, & M. Kuwata-

Gonokami. *The vectorial control of magnetization by light.* Nature Communications **2**, (2011) 362.

[Kas15] C. Kastl, C. Karnetzky, H. Karl, & A. W. Holleitner. *Ultrafast helicity control of surface currents in topological insulators with near-unity fidelity.* Nat. Commun. **6**.

[Kel15] J. Kellner, M. Eschbach, J. Kampmeier, M. Lanius, E. Młyńczak, G. Mussler, B. Holländer, L. Plucinski, M. Liebmann, D. Grützmacher, C. M. Schneider, & M. Morgenstern. *Tuning the Dirac point to the Fermi level in the ternary topological insulator (Bi1-xSbx)2Te3.* Applied Physics Letters **107**, 25.

[Kit69] C. Kittel, J. M. Gress, & A. Lessard. *Einführung in die Festkörperphysik*, Bd. 14. Oldenbourg München, 1969.

[Kli80] K. v. Klitzing, G. Dorda, & M. Pepper. *New Method for High-Accuracy Determination of the Fine-Structure Constant Based on Quantized Hall Resistance.* Phys. Rev. Lett. **45**, 6, (1980) 494.

[Koi15] N. Koirala, M. Brahlek, M. Salehi, L. Wu, J. Dai, J. Waugh, T. Nummy, M.-G. Han, J. Moon, Y. Zhu, D. Dessau, W. Wu, N. P. Armitage, & S. Oh. *Record Surface State Mobility and Quantum Hall Effect in Topological Insulator Thin Films via Interface Engineering.* Nano Lett. **15**, 12, (2015) 8245.

[Kra79] W. Kraut & R. von Baltz. *Anomalous bulk photovoltaic effect in ferroelectrics: A quadratic response theory.* Phys. Rev. B **19**, (1979) 1548.

[Kru11] J. Krumrain, G. Mussler, S. Borisova, T. Stoica, L. Plucinski, C. Schneider, & D. Grützmacher. *{MBE} growth optimization of topological insulator Bi2Te3 films.* Journal of Crystal Growth **324**, 1, (2011) 115 .

[Kur16] K. Kuroda, J. Reimann, J. Güdde, & U. Höfer. *Generation of Transient Photocurrents in the Topological Surface State of* Sb_2Te_3 *by Direct Optical Excitation with Midinfrared Pulses.* Phys. Rev. Lett. **116**, 7, (2016) 076801.

[Kuž99] P. Kužel, M. A. Khazan, & J. Kroupa. *Spatiotemporal transformations of ultrashort terahertz pulses.* J. Opt. Soc. Am. B **16**, 10, (1999) 1795.

[Lam05] N. Laman, M. Bieler, & H. Van Driel. *Ultrafast shift and injection currents observed in wurtzite semiconductors via emitted terahertz radiation.* J. Appl. Phys. **98**, 10, (2005) 103507.

[Lei99a] A. Leitenstorfer, S. Hunsche, J. Shah, M. C. Nuss, & W. H. Knox. *Femtosecond Charge Transport in Polar Semiconductors.* Phys. Rev. Lett. **82**, (1999) 5140.

[Lei99b] A. Leitenstorfer, S. Hunsche, J. Shah, M. Nuss, & W. Knox. *Detectors and*

sources for ultrabroadband electro-optic sampling: Experiment and theory. Appl. Phys. Lett. **74**, 11, (1999) 1516.

[Lei00] A. Leitenstorfer, S. Hunsche, J. Shah, M. C. Nuss, & W. H. Knox. *Femtosecond high-field transport in compound semiconductors.* Phys. Rev. B **61**, (2000) 16642.

[Lew14] R. A. Lewis. *A review of terahertz sources.* J. Phys. D: Appl. Phys. **47**, 37, (2014) 374001.

[Li13] J. J. Li, J. Chen, D. A. Reis, S. Fahy, & R. Merlin. *Optical Probing of Ultrafast Electronic Decay in Bi and Sb with Slow Phonons.* Phys. Rev. Lett. **110**, (2013) 047401.

[Li14] C. Li, O. van 't Erve, J. Robinson, Y. Liu, L. Li, & B. Jonker. *Electrical detection of charge-current-induced spin polarization due to spin-momentum locking in Bi2Se3.* Nature nanotechnology **9**, 3, (2014) 218.

[Lia10] L. Liao, Y.-C. Lin, M. Bao, R. Cheng, J. Bai, Y. Liu, Y. Qu, K. L. Wang, Y. Huang, & X. Duan. *High-speed graphene transistors with a self-aligned nanowire gate.* Nature **467**, 7313, (2010) 305.

[Liu10] C.-X. Liu, X.-L. Qi, H. Zhang, X. Dai, Z. Fang, & S.-C. Zhang. *Model Hamiltonian for topological insulators.* Phys. Rev. B **82**, 4, (2010) 045122.

[Liu15] Q. Liu, X. Zhang, L. Abdalla, A. Fazzio, & A. Zunger. *Switching a Normal Insulator into a Topological Insulator via Electric Field with Application to Phosphorene.* Nano Lett. **15**, 2, (2015) 1222.

[Luo13] C. W. Luo, H.-J. Chen, C. M. Tu, C. C. Lee, S. A. Ku, W. Y. Tzeng, T. T. Yeh, M. C. Chiang, H. J. Wang, W. C. Chu, J.-Y. Lin, K. H. Wu, J. Y. Juang, T. Kobayashi, C.-M. Cheng, C.-H. Chen, K.-D. Tsuei, H. Berger, R. Sankar, F. C. Chou, & H. D. Yang. *THz Generation and Detection on Dirac Fermions in Topological Insulators.* Adv. Opt. Mater. **1**, 11, (2013) 804.

[Mad72] O. Madelung. *Festkörpertheorie*, Bd. 109. Springer-Verlag, 1972.

[Mad98a] O. Madelung, U. Rössler, & M. Schulz. *Antimony telluride (*Sb_2Te_3*) optical properties.* In *Non-Tetrahedrally Bonded Elements and Binary Compounds I.* Landolt-Börnstein - Group III Condensed Matter vol. 41C, Springer Berlin Heidelberg, 1998 1–10.

[Mad98b] O. Madelung, U. Rössler, & M. Schulz. *Bismuth selenide (*Bi_2Se_3*) phonon dispersion, phonon frequencies.* In *Non-Tetrahedrally Bonded Elements and Binary Compounds I.* Landolt-Börnstein - Group III Condensed Matter vol. 41C, Springer Berlin Heidelberg, 1998 1–3.

[Mad98c] O. Madelung, U. Rössler, & M. Schulz. *Bismuth telluride (Bi_2Te_3) optical properties, dielectric constant.* In *Non-Tetrahedrally Bonded Elements and Binary Compounds I.* Landolt-Börnstein - Group III Condensed Matter vol. 41C, Springer Berlin Heidelberg, 1998 .

[Mal08] V. L. Malevich, R. Adomavičius, & A. Krotkus. *THz emission from semiconductor surfaces.* C. R. Phys. **9**, 2, (2008) 130.

[MCB02] G. M. T. Matthew C. Beard & C. A. Schmuttenmaer. *Measuring Intramolecular Charge Transfer via Coherent Generation of THz Radiation.* The Journal of Physical Chemistry A **106**, 6, (2002) 878.

[McI12a] J. W. McIver, D. Hsieh, S. G. Drapcho, D. H. Torchinsky, D. R. Gardner, Y. S. Lee, & N. Gedik. *Theoretical and experimental study of second harmonic generation from the surface of the topological insulator Bi_2Se_3.* Phys. Rev. B **86**, (2012) 035327.

[McI12b] J. W. McIver, D. Hsieh, H. Steinberg, P. Jarillo-Herrero, & N. Gedik. *Control over topological insulator photocurrents with light polarization.* Nat. Nanotechnol. **7**, 2, (2012) 96.

[Mel14] A. R. Mellnik, J. S. Lee, A. Richardella, J. L. Grab, P. J. Mintun, M. H. Fischer, A. Vaezi, A. Manchon, E.-A. Kim, N. Samarth, & D. C. Ralph. *Spin-transfer torque generated by a topological insulator.* Nature **511**, 7510, (2014) 449.

[Mic15] Z. Mics, K.-J. Tielrooij, K. Parvez, S. A. Jensen, I. Ivanov, X. Feng, K. Müllen, M. Bonn, & D. Turchinovich. *Thermodynamic picture of ultrafast charge transport in graphene.* Nature Communications **6**, (2015) 7655.

[Mih16] M. T. Mihnev, F. Kadi, C. J. Divin, T. Winzer, S. Lee, C.-H. Liu, Z. Zhong, C. Berger, W. A. de Heer, E. Malic, A. Knorr, & T. B. Norris. *Microscopic origins of the terahertz carrier relaxation and cooling dynamics in graphene.* Nature Communications **7**, (2016) 11617.

[Mil12] D. L. Mills. *Nonlinear optics: basic concepts.* Springer Science & Business Media, 2012.

[Mis97] S. K. Mishra, S. Satpathy, & O. Jepsen. *Electronic structure and thermoelectric properties of bismuth telluride and bismuth selenide.* J. Phys.: Condens. Matter **9**, 2, (1997) 461.

[Mis15] O. V. Misochko, J. Flock, & T. Dekorsy. *Polarization dependence of coherent phonon generation and detection in the three-dimensional topological insulator* Bi_2Te_3. Phys. Rev. B **91**, (2015) 174303.

[Moo10] J. E. Moore. *The birth of topological insulators.* Nature **464**, 7286, (2010) 194.

[Moo11] J. E. Moore. *Topological insulators.* IEEE Spectrum **48**, 7, (2011) 38.

[Mus01] C. Musio. *Vision: The Approach of Biophysics and Neurosciences: Proceedings of the International School of Biophysics, Casamicciola, Napoli, Italy, 11-16 October 1999*, Bd. 11. World Scientific, 2001.

[Nas06] F. Nastos & J. E. Sipe. *Optical rectification and shift currents in GaAs and GaP response: Below and above the band gap.* Phys. Rev. B **74**, 3, (2006) 035201.

[Nas10] F. Nastos & J. E. Sipe. *Optical rectification and current injection in unbiased semiconductors.* Phys. Rev. B **82**, 23, (2010) 235204.

[Nay07] D. A. Naylor & M. K. Tahic. *Apodizing functions for Fourier transform spectroscopy.* J. Opt. Soc. Am. A **24**, 11, (2007) 3644.

[Neu15] M. Neupane, S.-Y. Xu, Y. Ishida, S. Jia, B. M. Fregoso, C. Liu, I. Belopolski, G. Bian, N. Alidoust, T. Durakiewicz, V. Galitski, S. Shin, R. J. Cava, & M. Z. Hasan. *Gigantic Surface Lifetime of an Intrinsic Topological Insulator.* Phys. Rev. Lett. **115**, (2015) 116801.

[Nis12] J. Nishitani, T. Nagashima, & M. Hangyo. *Coherent control of terahertz radiation from antiferromagnetic magnons in NiO excited by optical laser pulses.* Phys. Rev. B **85**, (2012) 174439.

[Nol13] G. S. Nolas, J. Sharp, & J. Goldsmid. *Thermoelectrics: basic principles and new materials developments*, Bd. 45. Springer Science & Business Media, 2013.

[Nus94] M. C. Nuss, P. C. M. Planken, I. Brener, H. G. Roskos, M. S. C. Luo, & S. L. Chuang. *Terahertz electromagnetic radiation from quantum wells.* Applied Physics B **58**, 3, (1994) 249.

[Olb14] P. Olbrich, L. E. Golub, T. Herrmann, S. N. Danilov, H. Plank, V. V. Bel'kov, G. Mussler, C. Weyrich, C. M. Schneider, J. Kampmeier, D. Grützmacher, L. Plucinski, M. Eschbach, & S. D. Ganichev. *Room-Temperature High-Frequency Transport of Dirac Fermions in Epitaxially Grown* Sb_2Te_3*- and* Bi_2Te_3*-Based Topological Insulators.* Phys. Rev. Lett. **113**, (2014) 096601.

[Oni15] Y. Onishi, Z. Ren, K. Segawa, W. Kaszub, M. Lorenc, Y. Ando, & K. Tanaka. *Ultrafast carrier relaxation through Auger recombination in the topological insulator* $Bi_{1.5}Sb_{0.5}Te_{1.7}Se_{1.3}$. Phys. Rev. B **91**, (2015) 085306.

[Par13] K. Park, C. D. Beule, & B. Partoens. *The ageing effect in topological insulators: evolution of the surface electronic structure of* Bi_2Se_3 *upon K adsorption.* New J. Phys. **15**, 11, (2013) 113031.

[Pla16] H. Plank, L. E. Golub, S. Bauer, V. V. Bel'kov, T. Herrmann, P. Olbrich, M. Es-

chbach, L. Plucinski, C. M. Schneider, J. Kampmeier, M. Lanius, G. Mussler, D. Grützmacher, & S. D. Ganichev. *Photon drag effect in* $(Bi_{1-x}Sb_x)_2Te_3$ *three-dimensional topological insulators.* Phys. Rev. B **93**, (2016) 125434.

[Pri12] S. Priyadarshi, K. Pierz, & M. Bieler. *All-Optically Induced Ultrafast Photocurrents: Beyond the Instantaneous Coherent Response.* Phys. Rev. Lett. **109**, (2012) 216601.

[Qi11] X.-L. Qi & S.-C. Zhang. *Topological insulators and superconductors.* Rev. Mod. Phys. **83**, 4, (2011) 1057.

[Ram14] G. K. P. Ramanandan, G. Ramakrishnan, N. Kumar, A. J. L. Adam, & P. C. M. Planken. *Emission of terahertz pulses from nanostructured metal surfaces.* Journal of Physics D: Applied Physics **47**, 37, (2014) 374003.

[Rio12] J. Rioux & J. Sipe. *Optical injection processes in semiconductors.* Physica E **45**, (2012) 1 .

[Rou09] P. Roushan, J. Seo, C. V. Parker, Y. S. Hor, D. Hsieh, D. Qian, A. Richardella, M. Z. Hasan, R. J. Cava, & A. Yazdani. *Topological surface states protected from backscattering by chiral spin texture.* Nature **460**, 7259, (2009) 1106.

[Roy14] S. Roy, H. L. Meyerheim, K. Mohseni, A. Ernst, M. M. Otrokov, M. G. Vergniory, G. Mussler, J. Kampmeier, D. Grützmacher, C. Tusche, J. Schneider, E. V. Chulkov, & J. Kirschner. *Atomic relaxations at the (0001) surface of* Bi_2Se_3 *single crystals and ultrathin films.* Phys. Rev. B **90**, (2014) 155456.

[RS16] J.-C. Rojas-Sánchez, S. Oyarzún, Y. Fu, A. Marty, C. Vergnaud, S. Gambarelli, L. Vila, M. Jamet, Y. Ohtsubo, A. Taleb-Ibrahimi, P. Le Fèvre, F. Bertran, N. Reyren, J.-M. George, & A. Fert. *Spin to Charge Conversion at Room Temperature by Spin Pumping into a New Type of Topological Insulator:* α*-Sn Films.* Phys. Rev. Lett. **116**, (2016) 096602.

[SB14] J. Sánchez-Barriga, A. Varykhalov, J. Braun, S.-Y. Xu, N. Alidoust, O. Kornilov, J. Minár, K. Hummer, G. Springholz, G. Bauer, R. Schumann, L. Yashina, H. Ebert, M. Hasan, & O. Rader. *Photoemission of* Bi_2Se_3 *with Circularly Polarized Light: Probe of Spin Polarization or Means for Spin Manipulation?* Phys. Rev. X **4**, 1, (2014) 011046.

[SB16] J. Sánchez-Barriga, E. Golias, A. Varykhalov, J. Braun, L. V. Yashina, R. Schumann, J. Minár, H. Ebert, O. Kornilov, & O. Rader. *Ultrafast spin-polarization control of Dirac fermions in topological insulators.* Phys. Rev. B **93**, (2016) 155426.

[Sch15] C. B. Schmidt, S. Priyadarshi, S. A. Tarasenko, & M. Bieler. *Ultrafast magneto-*

photocurrents in GaAs: Separation of surface and bulk contributions. Appl. Phys. Lett. **106**, 14, (2015) .

[Sei16] T. Seifert, S. Jaiswal, U. Martens, J. Hannegan, L. Braun, P. Maldonado, F. Freimuth, A. Kronenberg, J. Henrizi, I. Radu, *et al. Efficient metallic spintronic emitters of ultrabroadband terahertz radiation.* Nature Photonics .

[Sel08] A. Sell, A. Leitenstorfer, & R. Huber. *Phase-locked generation and field-resolved detection of widely tunable terahertz pulses with amplitudes exceeding 100 MV/cm.* Opt. Lett. **33**, 23, (2008) 2767.

[Sha04] J. Shan & T. F. Heinz. *Terahertz Radiation from Semiconductors.* Springer Berlin Heidelberg, Berlin, Heidelberg, 2004 1–56.

[Sha12] K. M. F. Shahil, M. Z. Hossain, V. Goyal, & A. A. Balandin. *Micro-Raman spectroscopy of mechanically exfoliated few-quintuple layers of Bi2Te3, Bi2Se3, and Sb2Te3 materials.* Journal of Applied Physics **111**, 5.

[She84] Y.-R. Shen. *Principles of nonlinear optics.* Wiley-Interscience, New York, NY, USA, 1984.

[She14] C. Shekhar, C. E. ViolBarbosa, B. Yan, S. Ouardi, W. Schnelle, G. H. Fecher, & C. Felser. *Evidence of surface transport and weak antilocalization in a single crystal of the* Bi_2Te_2Se *topological insulator.* Phys. Rev. B **90**, (2014) 165140.

[Sim14] S. Sim, M. Brahlek, N. Koirala, S. Cha, S. Oh, & H. Choi. *Ultrafast terahertz dynamics of hot Dirac-electron surface scattering in the topological insulator* Bi_2Se_3. Phys. Rev. B **89**, (2014) 165137.

[Sip00] J. E. Sipe & A. I. Shkrebtii. *Second-order optical response in semiconductors.* Phys. Rev. B **61**, (2000) 5337.

[Sob12] J. A. Sobota, S. Yang, J. G. Analytis, Y. L. Chen, I. R. Fisher, P. S. Kirchmann, & Z.-X. Shen. *Ultrafast Optical Excitation of a Persistent Surface-State Population in the Topological Insulator* Bi_2Se_3. Phys. Rev. Lett. **108**, (2012) 117403.

[Sob14] J. Sobota, S.-L. Yang, D. Leuenberger, A. Kemper, J. Analytis, I. Fisher, P. Kirchmann, T. Devereaux, & Z.-X. Shen. *Ultrafast electron dynamics in the topological insulator Bi2Se3 studied by time-resolved photoemission spectroscopy.* J. Electron. Spectrosc. Relat. Phenom. **195**, (2014) 249 .

[Son14] J. C. W. Song & L. S. Levitov. *Shockley-Ramo theorem and long-range photocurrent response in gapless materials.* Phys. Rev. B **90**, 7, (2014) 075415.

[Sta14] R. L. Stamps, S. Breitkreutz, J. Åkerman, A. V. Chumak, Y. Otani, G. E. W. Bauer, J.-U. Thiele, M. Bowen, S. A. Majetich, M. Kläui, I. L. Prejbeanu, B. Di-

eny, N. M. Dempsey, & B. Hillebrands. *The 2014 Magnetism Roadmap.* J. Phys. D: Appl. Phys. **47**, 33, (2014) 333001.

[Sun02] S. K. Sundaram & E. Mazur. *Inducing and probing non-thermal transitions in semiconductors using femtosecond laser pulses.* Nat. Mater. **1**, 4, (2002) 217.

[Tom13] A. Tomasino, A. Parisi, S. Stivala, P. Livreri, A. C. Cino, A. C. Busacca, M. Peccianti, & R. Morandotti. *Wideband THz Time Domain Spectroscopy based on Optical Rectification and Electro-Optic Sampling.* Scientific Reports **3**, (2013) 3116.

[Tu15] C.-M. Tu, T.-T. Yeh, W.-Y. Tzeng, Y.-R. Chen, H.-J. Chen, S.-A. Ku, C.-W. Luo, J.-Y. Lin, K.-H. Wu, J.-Y. Juang, T. Kobayashi, C.-M. Cheng, K.-D. Tsuei, H. Berger, R. Sankar, & F.-C. Chou. *Manifestation of a Second Dirac Surface State and Bulk Bands in THz Radiation from Topological Insulators.* Sci. Rep. **5**, (2015) 14128.

[VA12] R. Valdés Aguilar, A. V. Stier, W. Liu, L. S. Bilbro, D. K. George, N. Bansal, L. Wu, J. Cerne, A. G. Markelz, S. Oh, & N. P. Armitage. *Terahertz Response and Colossal Kerr Rotation from the Surface States of the Topological Insulator* Bi_2Se_3. Phys. Rev. Lett. **108**, (2012) 087403.

[VA15] R. Valdés Aguilar, J. Qi, M. Brahlek, N. Bansal, A. Azad, J. Bowlan, S. Oh, A. J. Taylor, R. P. Prasankumar, & D. A. Yarotski. *Time-resolved terahertz dynamics in thin films of the topological insulator Bi2Se3.* Applied Physics Letters **106**, 1.

[vB81] R. von Baltz & W. Kraut. *Theory of the bulk photovoltaic effect in pure crystals.* Phys. Rev. B **23**, (1981) 5590.

[vdV04] N. C. J. van der Valk, T. Wenckebach, & P. C. M. Planken. *Full mathematical description of electro-optic detection in optically isotropic crystals.* J. Opt. Soc. Am. B **21**, 3, (2004) 622.

[Vug12] I. D. Vugmeyster, J. F. Whitaker, & R. Merlin. *GaP based terahertz time-domain spectrometer optimized for the 5-8 THz range.* Applied Physics Letters **101**, 18.

[Wan11] Y. H. Wang, D. Hsieh, D. Pilon, L. Fu, D. R. Gardner, Y. S. Lee, & N. Gedik. *Observation of a Warped Helical Spin Texture in* Bi_2Se_3 *from Circular Dichroism Angle-Resolved Photoemission Spectroscopy.* Phys. Rev. Lett. **107**, (2011) 207602.

[Wan12] Y. H. Wang, D. Hsieh, E. J. Sie, H. Steinberg, D. R. Gardner, Y. S. Lee, P. Jarillo-Herrero, & N. Gedik. *Measurement of Intrinsic Dirac Fermion Cooling on the Surface of the Topological Insulator* Bi_2Se_3 *Using Time-Resolved and Angle-Resolved Photoemission Spectroscopy.* Phys. Rev. Lett. **109**, (2012) 127401.

[Wan13] Y. Wang, L. Guo, X. Xu, J. Pierce, & R. Venkatasubramanian. *Origin of coherent*

phonons in Bi_2Te_3 excited by ultrafast laser pulses. Phys. Rev. B **88**, (2013) 064307.

[Wan16] M. Wang, S. Qiao, Z. Jiang, S. Luo, & J. Qi. *Unraveling Photoinduced Spin Dynamics in the Topological Insulator* Bi_2Se_3. Phys. Rev. Lett. **116**, 3, (2016) 036601.

[Web08] W. Weber, L. E. Golub, S. N. Danilov, J. Karch, C. Reitmaier, B. Wittmann, V. V. Bel'kov, E. L. Ivchenko, Z. D. Kvon, N. Q. Vinh, A. F. G. van der Meer, B. Murdin, & S. D. Ganichev. *Quantum ratchet effects induced by terahertz radiation in GaN-based two-dimensional structures.* Phys. Rev. B **77**, (2008) 245304.

[Wey15] C. Weyrich, M. Drögeler, J. Kampmeier, M. Eschbach, G. Mussler, T. Merzenich, T. Stoica, I. E. Batov, J. Schubert, L. Plucinski, B. Beschoten, C. M. Schneider, C. Stampfer, D. Grützmacher, & T. Schäpers. *Growth, characterization, and transport properties of ternary* $(Bi_{1-x}(Sb_x)_2Te_3$ *topological insulator layers.* ArXiv e-prints .

[Wu14] X. Wu, S. Carbajo, K. Ravi, F. Ahr, G. Cirmi, Y. Zhou, O. D. Mücke, & F. X. Kärtner. *Terahertz generation in lithium niobate driven by Ti:sapphire laser pulses and its limitations.* Opt. Lett. **39**, 18, (2014) 5403.

[Wyn05] K. Wynne & J. J. Carey. *An integrated description of terahertz generation through optical rectification, charge transfer, and current surge.* Optics Communications **256**, (2005) 400.

[Xia09] Y. Xia, D. Qian, D. Hsieh, L. Wray, A. Pal, H. Lin, A. Bansil, D. Grauer, Y. S. Hor, R. J. Cava, & M. Z. Hasan. *Observation of a large-gap topological-insulator class with a single Dirac cone on the surface.* Nat. Phys. **5**, 6, (2009) 398.

[Xue97] D. Xue & S. Zhang. *Dependence of Linear Electro-optic Coefficient on Difference in the Atomic Sizes in Zinc Blende Crystals.* Journal of Solid State Chemistry **130**, 1, (1997) 54 .

[Yan85] Y.-X. Yan, E. B. Gamble, & K. A. Nelson. *Impulsive stimulated scattering: General importance in femtosecond laser pulse interactions with matter, and spectroscopic applications.* The Journal of Chemical Physics **83**, 11, (1985) 5391.

[Yar89] A. Yariv. *Quantum electronics, 3rd.* Edn.(John WieLy & Sons, New York, 1988) p **389**.

[Yaz10] O. V. Yazyev, J. E. Moore, & S. G. Louie. *Spin Polarization and Transport of Surface States in the Topological Insulators* Bi_2Se_3 *and* Bi_2Te_3 *from First Principles.* Phys. Rev. Lett. **105**, (2010) 266806.

[Zei92] H. J. Zeiger, J. Vidal, T. K. Cheng, E. P. Ippen, G. Dresselhaus, & M. S. Dresselhaus. *Theory for displacive excitation of coherent phonons.* Phys. Rev. B **45**, (1992) 768.

[Zha09] H. Zhang, C.-X. Liu, X.-L. Qi, X. Dai, Z. Fang, & S.-C. Zhang. *Topological insulators in* Bi_2Se_3*,* Bi_2Te_3 *and* Sb_2Te_3 *with a single Dirac cone on the surface.* Nat. Phys. **5**, 6, (2009) 438.

[Zha10] W. Zhang, R. Yu, H.-J. Zhang, X. Dai, & Z. Fang. *First-principles studies of the three-dimensional strong topological insulators* Bi_2Te_3*,* Bi_2Se_3 *and* Sb_2Te_3. New J. Phys. **12**, 6, (2010) 065013.

[Zha11] J. Zhang, C.-Z. Chang, Z. Zhang, J. Wen, X. Feng, K. Li, M. Liu, K. He, L. Wang, X. Chen, Q.-K. Xue, X. Ma, & Y. Wang. *Band structure engineering in* $(Bi_{1-x}(Sb_x)_2Te_3$ *ternary topological insulators.* Nature Communications **2**, (2011) 574.

[Zha13] P. Zhang & M. W. Wu. *Hot-carrier transport and spin relaxation on the surface of topological insulator.* Phys. Rev. B **87**, 8, (2013) 085319.

[Zhu15] L.-G. Zhu, B. Kubera, K. Fai Mak, & J. Shan. *Effect of Surface States on Terahertz Emission from the* Bi_2Se_3 *Surface.* Sci. Rep. **5**, (2015) 10308.

List of Publications

Publications within this thesis

L. Braun, G. Mussler, A. Hruban, M. Konczykowski, T. Schumann, M. Wolf, M. Münzenberg, L. Perfetti and T. Kampfrath. *Ultrafast photocurrents at the surface of the three-dimensional topological insulator Bi_2Se_3*, Nature Communications **7**, (2016) 13259

T. Seifert, S. Jaiswal, U. Martens, J. Hannegan, L. Braun, P. Maldonado, F. Freimuth, A. Kronenberg, J. Henrizi, I. Radu, E. Beaurepaire, Y. Mokrousov, P. M. Oppeneer, M. Jourdan, G. Jakob, D. Turchinovich, L. M. Hayden, M. Wolf, M. Münzenberg, M. Kläui and T. Kampfrath. *Efficient metallic spintronic emitters of ultrabroadband terahertz radiation*, Nature Photonics **10**, (2016), 483–488

F. Boschini, M. Mansurova, G. Mussler, J. Kampmeier, D. Grützmacher, L. Braun, F. Katmis, J. S. Moodera, C. Dallera, E. Carpene, C. Franz, M. Czerner, C. Heiliger, T. Kampfrath, and M. Münzenberg. *Coherent ultrafast spin-dynamics probed in three dimensional topological insulators*, Scientific Reports **5**, (2015), 15304

Publications concerning other topics

A. Rubano, L. Braun, M. Wolf, and T. Kampfrath. *Mid-infrared time-domain ellipsometry: Application to Nb-doped $SrTiO_3$*, Applied Physics Letters **101**, (2012), 081103

Academic curriculum vitae

Der Lebenslauf ist in der Online-Version aus Gründen des Datenschutzes nicht enthalten.

Danksagungen

Die vorliegende Arbeit entstand am Fritz-Haber-Institut in Berlin und wäre ohne die Unterstützung zahlreicher Kolleginnen und Kollegen in dieser Form nicht zustande gekommen. An dieser Stelle möchte ich mich daher bei allen herzlich bedanken, insbesondere bei

Herrn Prof. Dr. M. Wolf für ein ideales Arbeitsumfeld und wissenschafliche Entfaltungsmöglichkeiten. Seine stete Bereitschaft zu kritischen Diskussionen war mir eine besondere Hilfe.

Mein ganz besonderer Dank gilt Herrn Dr. Tobias Kampfrath der immer als direkter Ansprechpartner zur Verfügung stand und wesentlich zur vielseitigen Themenstellung beigetragen hat. Unseren zahlreichen Diskussionen konnte ich viele wertvolle Anregungen entnehmen, die, zusammen mit seiner großzügigen Hilfe und Unterstützung bei vielfältigen Problemen, den Fortgang dieser Arbeit sehr gefördert haben.

Herrn Prof. Dr. M. Weinelt von der FU Berlin danke ich für die Übernahme des Koreferates.

Herrn Prof. M. Münzenberg (Ernst-Moritz-Arndt-Universität Greifswald), Prof. Dr. L. Perfetti (Université Paris-Saclay), Dr. G Mussler (Forschungszentrum Jülich) und ihren Mitarbeitern danke ich für die vielen hochwertigen Proben, deren Charakterisierung und wissenschaftlichen Diskussionen, die wesentlich zum Gelingen dieser Arbeit beigetragen haben.

Für die Hilfe bei der Nutzung und das Teilen ihres Wissens als auch ihrer wertvollen Messzeit an den intensiven THz-Strahlungsquellen möchte ich mich bei Herrn S. Mährlein und M. Sajadi bedanken.

Ferner gilt mein Dank Herrn G. Heyne, dem Leiter des Elektroniklabors am Fritz-Haber-Institut und stellvertretend für seine Mitarbeiter, Herrn V. Platschkowski und Herrn T. Zehentbauer, die mich bei allen Fragen zur Elektronik und technischen Weiterentwicklung tatkräftig unterstützt haben.

Herrn M. Krenz, Herrn S. Kubala und Herrn R. Franke danke ich, dass sie mir bei technischen Problemen jeder Art engagiert geholfen haben.

Darüber hinaus möchte ich mich bei meinen Kolleginnen und Kollegen der Terahertz Physik Gruppe und der Abteilung Physikalische Chemie für die vielen anregenden Gespräche bedanken.

Nicht zuletzt möchte ich mich bei meinen Eltern bedanken, die mich in vielerlei Weise unterstützt und ermutigt haben. Insbesondere aber bei meiner Frau, die es mir durch ihr Engagement ermöglicht hat Familie und Promotion zu vereinbaren.

Selbstständigkeitserklärung gemäss der Promotionsordnung

Sämtliche verwendeten Hilfsmittel, Hilfen und Quellen sind an der entsprechenden Stelle angegeben. Ich versichere, dass ich auf dieser Grundlage diese Arbeit selbstständig verfasst habe. Diese Arbeit wurde bisher weder in gleicher noch ähnlicher Form einer anderen Prüfungskomission vorgelegt oder veröffentlicht.

Berlin, den

Lukas Braun